POR Calabria 2014-2020 Fesr-Fse il futuro è un lavoro quotidiano

UNIONE EUROPEA FONDI STRUTTURALI E DI INVESTIMENTO EUROPEI · REPUBBLICA ITALIANA · REGIONE CALABRIA · UNIVERSITÀ DELLA CALABRIA

UNIVERSITA' DELLA CALABRIA

Dipartimento di Informatica, Modellistica, Elettronica e Sistemistica (DIMES)

Dottorato di Ricerca in

INFORMATION AND COMMUNICATION TECHNOLOGIES

Con il contributo di (Ente finanziatore)

POR CALABRIA 2014-2020

CICLO

XXXV

INVERSE SOURCE AND SCATTERING SOLUTIONS FOR MICROWAVE IMAGING APPLICATIONS

Settore Scientifico Disciplinare ING-INF/02 – CAMPI ELETTROMAGNETICI

Coordinatore: Ch.mo Prof. Giancarlo Fortino

Firma ____[redacted]

Firma oscurata in base alle linee guida del Garante della privacy

Supervisore/Tutor: Ch.ma Prof.ssa Sandra Costanzo

Firma____[redacted]

Firma oscurata in base alle linee guida del Garante della privacy

Dottorando: Dott. Giuseppe Lopez

[redacted]

Firma oscurata in base alle linee guida del Garante della privacy

"La borsa di dottorato è stata cofinanziata con risorse del Programma Operativo Regionale Calabria FSE/FESR 2014 – 2020 (CCI 2014IT16M2OP006)"

Inverse Source and Scattering Solutions for Microwave Imaging Applications

Giuseppe Lopez

A thesis submitted in partial fulfillment of the requirements for the degree of

Doctor of Philosophy

November 2022

To Maria Rosa and to my Family

Acknowledgements

First and foremost, I would like to express my gratitude to my Supervisor, Prof. Sandra Costanzo, for the consistent support and fruitful suggestions received throughout this path, for having encouraged and inspired me for the last three years.

My gratitude also goes to Prof. Natalia K. Nikolova, for having followed me during my visiting period at McMaster University, for the precious advice she gave me during the activities in her research group.

Truly thank you to my colleagues and friends - Adil, Antonio, Vincenzo and Alexandra Macarena, for the time spent in and out of the Lab.

I am also grateful to all the Electromagnetic Vision Lab members at McMaster University, for all their dedication and interest in supporting my research.

Thank you to Dan for the warm welcome and kindness during my days in Canada: your generosity and helpfulness will never be forgotten.

To my Family, the main guidance in all my decisions.
To Maria Rosa, for her never-ending support, love and patience.

Rende,
November 2022

Giuseppe Lopez

Abstract

Electromagnetic inverse scattering strategies are used in the field of Microwave Imaging (MWI) to reconstruct the complex permittivity profile of a certain domain of interest (DOI), where an object under test is assumed to be located therein. Generally speaking, when a certain antenna interrogates such a target, the back-scattered field is collected on the receivers, dislocated on a measurement domain outside the DOI. Inverse scattering is then performed considering both the incident and the back-scattered field, the latter usually indicated as the total field. The imaging solutions based on the inverse scattering methods pertain to the non-invasive diagnostic tools, and they can be used in a variety of applications, embracing, among others, through-the-wall imaging, Nondestructive testing (NDT), Ground-penetrating Radar (GPR) and biomedical imaging solutions. The inverse scattering algorithms generally require the use of both magnitude and phase of the total field, as well as of the incident field, the latter referring to the field evaluated without the presence of the target, assumed as the reference scenario. The performed research activities aim to find out reliable microwave imaging strategies, able to solve inverse scattering problems by using intensity-only electric field data. Although the full-data inverse scattering methods show promising reconstruction results, the demand in terms of complex data can be challenging, especially in the case of diagnostic methods performed at higher frequencies beyond the microwave frequency range. Furthermore, relaxing the coherence requirements of the acquisition stage, could open to the use of affordable and cheaper measurement equipment, such as power meters, as an alternative to more bulky and expensive measurement setups.

The microwave imaging solution has been treated from different perspectives. Initially, an iterative solution of the inverse scattering has been formulated, based on the contrast source formulation and denoted as Phaseless Contrast Source Inversion method (P-CSI). In this method, phaseless total field data have been used, together with numerical and/or simulated incident field data, meaning that the incident field is assumed to be preliminary known as imaging system characterization.

Secondly, dealing with phaseless data, an inverse source problem has been also addressed. Indeed, when considering near-field antenna measurement and diagnostic, phaseless approach can be less prone to probe positioning errors as compared to the complex-data case. Therefore, the incident field modeling process has been analyzed and proposed in a phaseless version, so that a complete phase-free inverse scattering framework has been formulated. More specifically, a strategy based on a spatial domain indirect holography technique (SDIHT) has been extended to the inverse source solution and combined with incident field characterization methods, the latter expressed in the form of Modal Expansion (ME) or, alternatively, in terms of equivalent current densities, which solution goes under the name of Source Reconstruction Method (SRM).

The inverse strategy has been first tested on 2D simplified targets, with canonical geometries and low permittivity contrast, considering both simulated and experimental data. Secondly, the predictability of the method has been tested when considering more inhomogeneous targets. In this context, a deep focus on breast imaging solutions has been addressed. For this case, system requirements in terms of data sparsity, background medium selection and incident field characterization have been analyzed. The phaseless framework has been ultimately validated in-silico, when considering 3D scattering models, with field data pertaining to the near field zone.

Sommario

Le attività di ricerca svolte hanno riguardato l'esplorazione di tecniche di imaging a microonde, basate sull'utilizzo di misure di sola intensità di campo elettrico. Sebbene l'impiego di misure di campo complesse diano buoni riscontri in termini di accuratezza nella ricostruzione della permettività complessa dei target sotto osservazione, lo studio di tecniche di solo modulo è stato dettato da differenti fattori. In primo luogo, l'utilizzo della sola intensità dei campi coinvolti può aprire ad una consistente semplificazione del setup di acquisizione, consentendo l'utilizzo di dispositivi più economici rispetto a quelli impiegati nei setup di imaging tradizionali, solitamente coerenti ed ingombranti. Inoltre, sebbene il contributo di fase dei campi retrodiffusi porti con sé gran parte del contenuto informativo del target sotto osservazione, una sua misura accurata non può essere sempre garantita, specie nel caso di setup di imaging a scansione meccanica e con frequenze di lavoro più elevate, al limite del regime delle microonde o oltre. Inizialmente, l'approccio proposto ha visto l'utilizzo di misure di solo modulo per i valori di campo elettrico totale, assumendo, per i campi incidenti, valori di campo noti a priori e/o provenienti da simulazioni. Tale metodo di inversione è stato inizialmente testato su dataset di campi simulati e sperimentali, operanti sia in campo lontano che in campo vicino, relativamente a target di natura metallica e dielettrica, considerando in prima istanza scatteratori deboli. Successivamente, il metodo è stato validato considerando campi retro-diffusi e operanti nella banda delle microonde, nel caso di target fortemente eterogenei e ad elevato contrasto. Particolare attenzione è stata posta all'utilizzo di tale metodologia nell'ambito dell'imaging del seno. In tale contesto, è stato validato un modello a linee di trasmissione, al fine di determinare le condizioni ottimali in termini di frequenza di lavoro e caratteristiche di permettività del mezzo di background, in modo da scegliere opportunamente il compromesso tra accoppiamento elettromagnetico e profondità di penetrazione.

Tale modello è stato successivamente validato considerando il caso di modelli di seno tridimensionali ed impiegando sorgenti di campo non-analitiche. Una seconda parte della ricerca ha riguardato lo studio di metodi di inverse source e di diagnostica delle antenne, da includere all'interno delle procedure di scattering inverso, atte ad estendere l'utilizzo di misure di sola intensità anche per la caratterizzazione del campo incidente. Quest'ultimo, nelle soluzioni proposte in letteratura, è infatti solitamente assunto come noto nella sua formulazione in termini di modulo e fase. Sono stati proposti una serie di approcci, ottenuti combinando tecniche olografiche spaziali e metodi di diagnostica, quest'ultimi basati sull'espressione dei campi incidenti in termini di espansione modale o di densità di correnti equivalenti. Tali tecniche consentono di ricavare le distribuzioni di campo incidente delle sorgenti coinvolte nella fase di imaging, a partire da misure di sola intensità, consentendo dunque lo sviluppo di una procedura di imaging interamente phase-free. La combinazione dei metodi di inverse source e inverse scattering a partire da valori di campo in solo modulo, è stata successivamente validata in-silico, considerando sia un dominio di immagine bidimensionale, sia target tridimensionali, con analisi effettuate in campo vicino. I risultati ottenuti dimostrano le peculiarità del metodo proposto e la sua validità in diversi scenari applicativi, tra i quali si evidenzia il potenziale impiego nell'ambito della diagnostica biomedicale.

Contents

List of Tables

List of Figures

Abbreviations

ACR American College Radiology.

ANN Artificial Neural Networks.

AUT Antenna Under Test.

AVA Antipodal Vivaldi Antenna.

AWGN Additive White Gaussian Noise.

BA Born Approximation.

BI-RADS Breast Imaging Reporting & Data System.

BIM Born Iterative Method.

BP Backpropagation.

CC-CSI Cross-correlated Contrast Source Inversion.

CG Conjugate Gradient.

CG-FFT Conjugate Gradient Fast Fourier Transform.

CGLS Conjugate Gradient for Least Square.

CS Contrast Source.

CSI Contrast Source Inversion.

DBA Distorted Born Approximation.

DBIM Distorted Born Iterative Method.

DL-AVA Double-Layer Antipodal Vivaldi Antenna.

DOI Domain of interest.

EFIE Electric-Field Integral Equations.

FF Far-Field.

FFT Fast Fourier Transform.

GPR Ground-penetrating Radar.

LSM Linear Sampling Method.

ME Modal Expansion.

MoM Method of Moments.

MR-CSI Multiplicative Regularized Contrast Source Inversion.

MRI Magnetic Resonance Imaging.

MWI Microwave Imaging.

NDT Nondestructive testing.

NF Near-Field.

OSM Orthogonality Sampling Method.

OUT Object Under Test.

PBP Phaseless backpropagation.

P-CSI Phaseless Contrast Source Inversion.

PML Perfectly Matched Layer.

PR Phase Retrieval.

PSF Point Spread Function.

RMSE Root Mean Square Error.

SDIHT Spatial Domain Indirect Holography Technique.

SL-AVA Single-Layer Antipodal Vivaldi Antenna.

SLL Sidelobe level.

SOM Subspace-based optimization method.

SRM Source Reconstruction Method.

TL Transmission Line.

TM Transverse Magnetic.

TSVD Truncated Singular Value Decomposition.

TV Total Variation.

US Ultrasound.

UWB Ultra-wide Band.

Chapter 1

Introduction

1.1 Introduction

Microwave imaging methods have been an open research field for decades. The applications explored among the scientific community are different, putting a lot of attention and effort into the development of solution strategies to be applied to a non-exhaustive list of applications, including remote sensing, Nondestructive testing (NDT), Ground-penetrating Radar (GPR), concealed weapon detection and, above all, biomedical imaging. In the latter case, although most of the imaging methods made strides during the years, the cases in which microwave biomedical imaging apparatus have reached the clinical trial stages are limited. Aside from the complexity of the measurement setup, the main challenges in this context lie on the limited predictability of the scattering phenomena in the case of very heterogeneous structures, typically involved in human tissues. Indeed, despite the existent dielectric diversity among the tissues, quantitative reconstruction of these properties is definitely the ultimate long-term goal of microwave imaging for biomedical scenarios, with a view to its use as an affordable and supportive diagnostic tool. From an analytical perspective, microwave inverse scattering problems are well-known to be ill-posed and ill-conditioned and they face non-linearity issues by nature. Consequently, some strategy needs to be adopted, in order to have reliable and stable solutions.

Among the different open and fascinating research questions within the microwave imaging community, one of those considers the possibility to detect, from a qualitative and potentially quantitative perspective, the electromagnetic properties of a generic Object Under Test (OUT), by exploiting intensity-only measurements of the involved fields.

The motivations behind this assumption are different and can be read from multiple perspectives. Indeed, despite the advance in measurement equipment, *full-data* field acquisitions would require good accuracy in the measurements of both amplitude and phase of the involved fields. Despite this task can be quite successful in the case of measurements performed within the microwave frequency range, it cannot always be accomplished or guaranteed especially at higher frequencies. Furthermore, in the case of mechanical scanning configurations, phase data result to be more prone to positioning errors, whereas the use of complex signals generally needs coherent detection and thus a phase synchronization between transmitters and receivers. Phaseless acquisitions can strongly simplify the hardware complexity, while the phase stability and synchronization requirements can be also relaxed. At the same time, phase data usually carry most of the information content about the nature of the scatterer. These facts consequently put phaseless microwave imaging as a challenging task to be performed. Despite the limited demand on the measurement equipment, the use of intensity-only field data heavily loads the inverse scattering strategy complexity and it requires *additional* information to cope with the enforced data sparsity.

Among the imaging phaseless approaches proposed in the research community, most of them rely on a strong assumption regarding the incident field data distribution, i.e., the field evaluated without the presence of the target under inspection and known as a *reference* scenario. Indeed, in these approaches, the incident field is assumed to be analytically known or available from simulations. In this thesis, some approaches have been investigated to cope with this assumption in the phaseless domain, so that the incident field data, required for the solution of the inverse scattering problem, could be potentially retrieved from amplitude-only data samples, resulting in a complete phaseless framework. More specifically, along with a phaseless imaging reconstruction method, a combined inverse source strategy for the estimation of the incident field distribution, starting from amplitude-only data samples, has been analyzed and secondly applied to multi-static imaging scenarios. The developed methods have been preliminarily tested considering canonical targets, then most of the attention has been dedicated to the use of these tools in the field of biomedical imaging, with a strong emphasis on the case of breast imaging solutions. In this context, investigations have been performed for the description of the most suitable imaging setup configuration under the restriction imposed by the phaseless approach.

Furthermore, in addition to the breast imaging task, supplementary imaging system conditions have been investigated; among these, the predictability of a proposed simplified transmission line model for the coupling medium selection and the operating frequency, specifically tailored for breast imaging case, has been tested and secondly validated by 3D electromagnetic simulations, where more realistic and complex breast models have been involved.

1.2 Main contribution of Present Work

The major contributions proposed in this thesis can be summarized as follows:

1) **Inverse Scattering:** the implementation of a phaseless microwave imaging solution, namely the Phaseless Contrast Source Inversion (P-CSI) method, based on the classical Contrast Source (CS) formulation of the inverse scattering problem, where both incident and total field data in terms of amplitude-only data are used for the inversion strategy. The method has been inspected mostly in the following aspects:

   (a) The introduction of a proper initial guess selection for the (iterative) reconstruction method, that makes use of a phaseless backpropagation solution in a microwave imaging context, where the amplitude-only data is fully exploited as prior information content;

   (b) The validation of the method on experimental far-field data, in the presence of metallic or low-permittivity dielectric targets, and extension to the case of scattered field coming from high contrast targets, evaluated in the near-field zone;

   (c) The validation of the proposed solution in the context of microwave breast imaging, by considering realistic breast models with different levels of fibroglandular density. Furthermore, a context study regarding the main aspects of a microwave breast imaging system design has been also addressed.

2) **Inverse Source:** the definition of a combined strategy for the incident field characterization in microwave imaging methods, pertaining to the inverse source problem solutions, allowing to obtain the field distribution within the imaging domain starting from phaseless measurements, by combining holography-based solutions with antenna characterization methods.

Chapter 2

Problem Statement and State of the Art

2.1 Electromagnetic Scattering Problems

Generally speaking, scattering phenomena arise when an electromagnetic field interacts with a certain object, conventionally indicated as *target*. As a consequence of the impinging field, the target acts as a field source; consequently, besides the presence of the incident field, a superimposed field component is observed, conventionally named as the *scattered* field. This field can be physically interpreted as the field coming from the *induced* currents, generated due to field-target interaction. The scattering events occur as a consequence of the difference in the electromagnetic properties between the target and the background. Therefore, a *total* field distribution is defined as the superimposition of the scattered field and the incident portion, the latter evaluated without the presence of the target and indicated as *reference* scenario. Electromagnetic scattering can be treated from two different points of view, similar to the cause-effect relation: in fact, the determination of the field scattered by a certain object, by knowing its dielectric properties goes under the name of forward scattering problem (cause $\rightarrow$ effect). This kind of problem results to be well-posed in the Hadamard's sense [1].

For clarity, here the definition of a well-posed problem is recalled:

Definition. *A problem is defined as well-posed in the sense of Hadamard if:*

- *it has a solution;*
- *the solution is unique;*
- *the solution depends continuously on the data.*

A problem is instead defined to be ill-posed if at least one of those conditions is not guaranteed. In the forward solution, all the conditions of well-posedness are valid; this is not true in the case of the inverse scattering counterpart, which consists in finding out the electromagnetic properties of a certain target, supposed to be unknown, starting from measured field data (cause $\leftarrow$ effect). In this case, the existence of a unique solution can be guaranteed only if there are no constraints on the data availability (i.e. full-data case) [2], whereas this is not always the case when considering more data sparsity, such as the phaseless data case discussed in this work. Indeed, in the case of phaseless far-field measurement, uniqueness is not guaranteed due to the translation invariance of the amplitude-only far-field pattern. Furthermore, minimum perturbation (viz., noise) of the input data, i.e. the field coming from measurements, can determine strong variation in the output results, consequently leading to poor reliability and robustness of the reconstruction. Despite the fact that the ill-posedness of the problem can be alleviated by considering a multi-view case, the problem is still ill-posed due to the finite number of (independent) measurements. Consequently, a limited number of illumination points can be effectively exploited, whereas additional constraints such as prior information and/or proper initial guess in the case of iterative inverse scattering solutions, need to be properly addressed.

Having reliable reconstructions in imaging methods is of remarkable importance, especially when associated with medical applications. Indeed, significant is the number of screened false-positives cases experienced with the X-ray-based imaging solutions, which often require additional supportive tools, such as Magnetic Resonance Imaging (MRI). To this extent, the use of Microwave Imaging (MWI) techniques as diagnosis and screening tools is still promising and intense research is currently underway among different research groups worldwide. More specifically, MWI applied to breast cancer detection still results to be one of the most investigated and emerging technology [3]; this can be associated to the fact that most of the currently available screening solutions requires the use of ionizing radiation and acquisition methods not comfortable for the patient - e.g., breast compression in mammography - which remains the gold standard imaging modality for breast cancer screening [4]. Furthermore, the potential use of cheap and portable devices represents one of the additional advantages of MWI solutions as compared to the other existing medical imaging modalities.

2.2 Mathematical Framework and Involved Operators

A generic microwave imaging setting is provided in Fig. 2.1. This setup illustrates a multi-static/multi-view imaging system, consisting of a certain number of transceivers N, located along a closed curve S. Those are alternately assumed as transmitters, while the remaining ones act as receivers. By doing so, a multi-illumination system is considered, whereas the scattering response is detected from multiple receiving angles. The imaging domain, denoted as D, represents the investigated area and assuming to enclose the target's support, hereby denoted as B. By indicating with ϵ_{r_b} the complex relative permittivity of the homogeneous and non-magnetic background medium that surrounds the Object Under Test (OUT), while assuming the latter to have a certain complex relative permittivity $\epsilon_r(\mathbf{r})$, a dielectric contrast function can be defined as follows:

$$\chi(\mathbf{r}) = \frac{\epsilon_r(\mathbf{r}) - \epsilon_{r_b}}{\epsilon_{r_b}} \tag{2.1}$$

The contrast function defined in Eq. (2.1) is the unknown that the MWI inverse scattering solutions aim to find. Inverse scattering generally relies on the formulation of the electromagnetic scattering problem in terms of Electric-Field Integral Equations (EFIE), here briefly recalled.
A 3D EM model is usually extremely complex to formulate, especially in the case of heterogeneous scattering objects; indeed the inverse scattering solution is translated into a prohibitive computational task, especially when forward models are considered for the generation of synthetic field data to

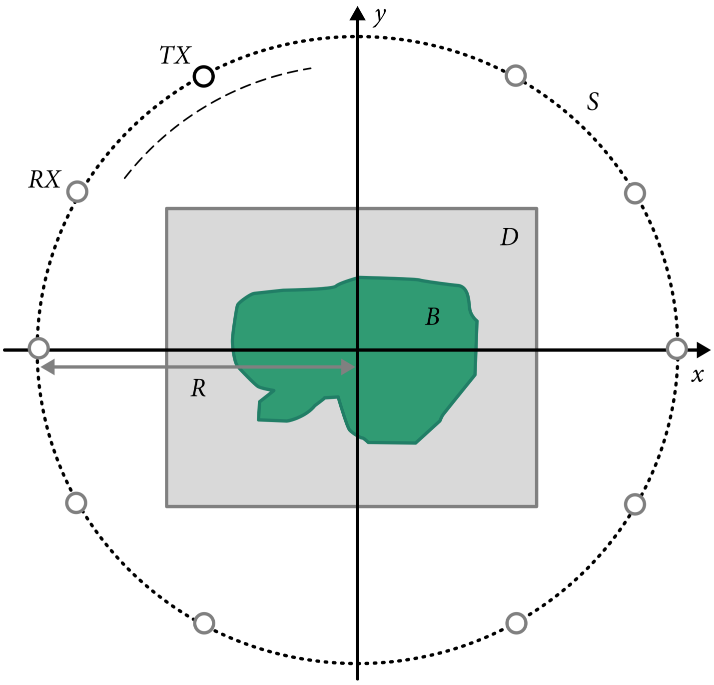

Figure 2.1: Generic imaging scenario.

test the inversion methods. As a consequence, here the reduction to a 2D scheme has been adopted, starting from the 3D Helmholtz equation for the electric field, within a non-magnetic uniform background, i.e., $\mu_b(\mathbf{r}) = \mu_0$:

$$\nabla \times \nabla \times \mathbf{E}(\mathbf{r}) - \omega^2 \mu_b \epsilon(\mathbf{r})\mathbf{E}(\mathbf{r}) = 0 \tag{2.2}$$

Assuming a field symmetry for the E-field in the scattering volume, meaning that the incident field, as well as the scattered field coming from the target, can be considered *invariant* along the z-direction:

$$\frac{\partial \mathbf{E}(\mathbf{r})}{\partial z} = 0 \tag{2.3}$$

When Eq. (2.3) holds true, the scattering problem can be assumed to be fully described by the E_z component only, whereas the magnetic field components are assumed to be transverse to the z-axis. The considered approach is known as TM_z approximation and the Eq. (2.2) can be expressed as:

$$\nabla_\perp^2 E_z(\mathbf{r}) + \omega^2 \mu_b \epsilon(\mathbf{r}) E_z(\mathbf{r}) = 0 \tag{2.4}$$

where $\nabla_\perp^2$ indicates the 2D Laplace operator in the transverse plane.

The solution of Eq. (2.4) enables the data acquisition and the reconstruction stage to be performed on planes, i.e., considering a tomography approach. The 2D Helmholtz equation can be evaluated for two different domains - the *data domain* $\mathbb{S}$ (or simply S), including the *measurement space*, and the *state domain* $\mathbb{D}$ (or simply D), denoting the *imaging domain*. According to these definitions, two equations pertaining to the above-mentioned domains can be formulated as follows:

$$\begin{aligned} E^s(\mathbf{r}) = E^t(\mathbf{r}) - E^i(\mathbf{r}) = {k_b}^2 \int_{\mathbb{D}} g(\mathbf{r}, \mathbf{r}')\chi(\mathbf{r}')E^t(\mathbf{r}')\ \mathbf{dr}', \mathbf{r} \in \mathbb{S} \\ E^t(\mathbf{r}) = E^i(\mathbf{r}) + {k_b}^2 \int_{\mathbb{D}} g(\mathbf{r}, \mathbf{r}')\chi(\mathbf{r}')E^t(\mathbf{r}')\ \mathbf{dr}', \mathbf{r} \in \mathbb{D} \end{aligned} \tag{2.5}$$

where E^t, E^i and E^s indicate the total, incident, and scattered field portions, respectively, whereas g denotes the Green's scalar radiating operator:

$$g(\mathbf{r}, \mathbf{r}') = \frac{i}{4} H_0^{(1)}(k_b|\mathbf{r} - \mathbf{r}'|) \tag{2.6}$$

While $k_b = \omega\sqrt{\epsilon_0\epsilon_{r_b}\mu_0}$ indicates the background wave number, whereas $H_0^{(1)}$ denotes the Hankel function of zeroth-order and first kind. The EFIE in Eq. (2.5) show the non-linear relation between fields and contrast. Throughout the text, the definition of an equivalent Contrast Source (CS), denoted as $w(\mathbf{r})$, will be used. This refers to the equivalent current that is generated as a consequence of the existing dielectric contrast between the background and the scatterer:

$$w(\mathbf{r}) := \chi(\mathbf{r})E^t(\mathbf{r}) \tag{2.7}$$

The term in Eq. (2.7) can be exploited to re-write Eq. (2.5) in a more compact form, which can be useful when the CS is used as an auxiliary unknown for the solution of the inverse scattering problem, as in the case of the Contrast Source Inversion (CSI) based method described in Chapter 4. Consequently, the EFIE can be expressed in the CS formulation as:

$$\begin{aligned} E^s(\mathbf{r}) = {k_b}^2 \int_{\mathbb{D}} g(\mathbf{r}, \mathbf{r}')w(\mathbf{r}')\ \mathbf{dr}', \mathbf{r} \in \mathbb{S} \\ E^t(\mathbf{r}) = E^i(\mathbf{r}) + {k_b}^2 \int_{\mathbb{D}} g(\mathbf{r}, \mathbf{r}')w(\mathbf{r}')\ \mathbf{dr}', \mathbf{r} \in \mathbb{D} \end{aligned} \tag{2.8}$$

In order to handle those equations numerically, a discretization form needs to be derived. This can be done by considering a Method of Moments (MoM) solution and by using elementary pulse basis functions. More specifically, the imaging domain can be discretized into $M = N_x \times N_y$ sub-wavelength cells, located at $\mathbf{r}_m$, with $m \in (1, 2, \dots, M)$. Each cell is approximated to an equivalent disk with radius $a = \sqrt{\frac{\Delta_x \Delta_y}{\pi}}$, where $\Delta_{x,y}$ is the one-dimension cell size, so that a closed form of the Green's operator can be obtained [5]. Therefore, the EFIE in Eq. (2.5) can be re-written as:

$$\begin{aligned} \mathbf{E^s} &= \mathbf{G_S} diag\left(\boldsymbol{\chi}\right) \mathbf{E^t} \\ \mathbf{E^t} &= \mathbf{E^i} + \mathbf{G_D} diag\left(\boldsymbol{\chi}\right) \mathbf{E^t} \end{aligned} \tag{2.9}$$

where $\boldsymbol{\chi}$ is expressed as a $M \times 1$ vector, whereas $\mathbf{G_{S,D}}$ are the integral operators, with size $N_{RX} \times M$ and $M \times M$ respectively, whose formulations are expressed as:

$$\begin{aligned} \mathbf{G_S}(s,m) &= \frac{ik_b\pi a}{2} J_1(k_b a) H_0^{(1)}(k_b|\mathbf{r}_s - \mathbf{r}_m|) \\ \mathbf{G_D}(m,m') &= \begin{cases} \frac{ik_b\pi a}{2} J_1(k_b a) H_0^{(1)}(k_b|\mathbf{r}_s - \mathbf{r}_m|) & m \neq m' \\ \frac{ik_b\pi a}{2} H_1^{(1)}(k_b a) - 1 & m = m' \end{cases} \end{aligned} \tag{2.10}$$

where $\mathbf{r}_s$ indicates each receiver position, with $s \in (1, 2, \dots, N_{RX})$.

2.3 Linear and Non-linear Inverse Scattering Strategies

The electromagnetic inverse scattering strategies are generally distinguished from different perspectives. One such criterion is based on how the non-linearity highlighted in Eq. (2.5) is treated. Some approaches consider the linearized version of the scattering problem, discarding the mutual interaction inside the imaging domain and mutual coupling effects. This assumption is equivalent to assume the total field inside the imaging domain to be equal to the incident field only. This strategy leads to the common Born Approximation (BA), which brings some limitations in the reconstruction capabilities of the inverse solutions.

Indeed, in this case, the operation of the inverse method is limited to *weak* scatterers; thus, it cannot be extended to the case of high-contrast objects. Besides the reconstruction limitations from a quantitative perspective, the linearization of the scattering solution enables the possibility of having real-time imaging methods [6]. In this context, recent solution strategies that combine the use of the BA and of the Rytov approximation - the latter putting constraints on the dielectric contrast only and not on the target's size - result in promising reconstructions, specifically for tissue imaging [7], [8]. Alternative linearized methods consider a reference scenario that differs from the case of a homogeneous background, such as the Distorted Born Approximation (DBA), where the scatterer is assumed as a form of perturbation within the background. Other potential extensions to the BA-based methods are the non-linear and iterative well-known strategies such as the Born Iterative Method (BIM) and the Distorted Born Iterative Method (DBIM), where in the latter the internal field and the Green's function are updated during each iteration, by iterative forward solver recalls. Linearized methods have been used, combined with Truncated Singular Value Decomposition (TSVD) solutions, with promising qualitative reconstruction results in different fields of application such as microwave ablation [9] and through-the-wall imaging solutions [10], [11]. When the target under investigation does not fall within the condition of weak scatter, the full-non linearity of the scattering problem can be tackled by considering different methods. In most of these solutions, the inverse scattering problem is treated as the minimization of a certain cost function, that quantifies the discrepancy between the measured field data and the one obtained from the designed scattering model. Among these strategies, global optimization methods, also known as stochastic reconstruction methods, such as particle swarm algorithms [12], [13] have been adopted in the past, but their usage is limited due to the high computational load and intrinsically more suitable for parallel computing solutions.

Currently, the majority of the non-linear methods are instead based on local deterministic solutions. In that case, the local optimization strategies that are generally used include, among others, Gaussian-Newton methods, Levenberg-Marquardt solutions, steepest descent methods, and conjugate gradient-based solutions [14]–[16]. Unfortunately, the convergence to a physical solution is strongly related to the selection of a proper-defined initial guess, so that the optimization problem does not get stuck into local minima, leading to the occurrence of potential false solutions. Consequently, regularization strategies and a suitable initialization of the inverse procedure are crucial for the success of the imaging task.

2.4 Phaseless Inverse Scattering - Motivation and Current Trends

The use of intensity-only data in inverse scattering is a challenging problem that has gained a remarkable interest in the research community. The solutions trying to face this task are different, such as the ones based on an inexact-Newton scheme operating on Lebesgue spaces [17], [18], the CSI-based methods [19] or the Subspace-based optimization method (SOM) proposed in [20]. Further approaches consider the use of Gauss-Newton inversion schemes [21], and more recently, solutions based on the contraction of the integral scattering equation have been investigated [22], where multiple scattering contributions can be handled by splitting them into global and local wave components. By properly weighting those two contributions, the non-linearity of the phaseless method can be effectively alleviated. Another category of solutions considers an extended Rytov approximation model for non-weak scatterers, where the high-order phase term that is conventionally neglected in the standard Rytov formulation, can be estimated by using the inhomogeneous plane wave theory [23], [24]. Lately, the use of Artificial Neural Networks (ANN)-based methods has been recently proposed and successfully applied to numerical simulations for the reconstruction of homogeneous cylindrical targets [25], [26].

The motivations behind the use of amplitude-only inverse scattering strategies are different. Firstly, the accuracy in phase measurements cannot be always guaranteed and it can be severely compromised, especially in the case of imaging systems with higher frequencies approaching the millimeter-wave range and beyond. Secondly, complex measured data are more prone to positioning errors, especially in the case of multi-static imaging scenarios and/or mechanical positioners [27]. Furthermore, the potential use of intensity-only data could open to a more compact and cheap measurement setup, by using affordable power meters without the need for bulky equipment.

As a counterpart, the lack of phase information requires more effort in the inverse scattering process, to compensate for the limited data information coming from amplitude-only data. This limitation can be effectively compensated by increasing the data diversity, such as the number of *illumination* points. Unfortunately, an upper limit exists in the number of independent data that can be extracted in this case. More specifically, in the case of the phaseless scenario, to properly characterize both incident and total field intensities, the required number of samples on a closed curve can be obtained according to the criteria provided in [28]–[30]:

$$max\{(4k_bR_S)^2, [2k_b(R_S + R_D)]^2\} \tag{2.11}$$

where R_S and R_D denote the radius of the measurement curve and the smallest circle that surrounds the target, respectively. Indeed, due to reciprocity, only half of these samples constitute independent data. As compared to the phase-available counterpart, in a phaseless imaging domain, the scattered field portion cannot be extracted from the total field by means of a simple subtraction of the incident field. This strong limitation further complicates the solution of the inverse scattering problem.

Indeed, a challenging problem that arises is the inclusion of prior information about the target to be imaged, by solely considering the limited available data. Standard Backpropagation (BP) solutions cannot be used in the case under inspection, since expressed in terms of the scattered portion of the field, which is not available in the case of phaseless measurements. Some strategies need to be necessarily investigated to cope with this non-trivial task. In the case of iterative methods, one option consists of compensating for the lack of phase information, by exploiting the intensity measured data within the formulation of a proper initial guess. According to this theory, a feasible strategy that makes use of a modified back-propagation approach in a phaseless context, indicated as Phaseless backpropagation (PBP) is investigated, and it is discussed in detail in Section 4.2.

Broadly speaking, the solution to the inverse scattering problems from phaseless data can be faced by considering two different strategies. The first family of methods includes a two-step based solution, consisting of the preliminary estimation of the field phase starting from the total field amplitude only data, by applying a Phase Retrieval (PR) step.

The latter can be accomplished in different ways; in the case of FF measurements, the complex-valued field can be reconstructed by following the approach initially provided by Fienup in [31]–[33], and then extended to different engineering fields, such as optics and x-ray crystallography. This approach consists of a Fourier-based reconstruction method, where the field phase is retrieved starting from the knowledge of the absolute value of its spatial Fourier transform. When the FF condition does not necessarily hold true, different solutions coming from interferometry and phase-shift related methods can be exploited, so that the phase information content can be extracted from basic electromagnetic theory, combined with multiple intensity field data. The data variety that is required by this kind of approach can be achieved in different ways, e.g., by considering measurements performed along two parallel planes [34]–[36] or by considering a two co-planar probe scanning system [37]. Once completed, this step is generally followed by the solution of a classical inverse scattering problem based on complex field data performed in the second step. The two-step approach allows better control of the non-linearity but, at the same time, it has its main drawback in the potential propagation error that affects the retrieved phase. The computed errors in the phase reconstruction, in fact, could propagate to the imaging step, causing a non-linear amplification of such error [29]. Alternatively, a second family of single-step approaches aims to solve the inverse scattering problem by directly exploiting the measured total field intensity data, without involving a phase retrieval stage for this field [38]. In this type of method, the discrepancy between the intensity data and the modeled one is evaluated and thus minimized according to a certain optimization scheme.

Aside from the total and scattered field analysis, in the context of microwave imaging, an insight into incident field modeling, especially in the case of amplitude-only data methods, is appropriate. As a matter of fact, most of the contributions in the field of microwave imaging based on amplitude-only data, consider a strong assumption about the availability of the incident field distribution inside the imaging area. This task could be accomplished by sampling the entire imaging domain, resulting in a cumbersome measurement stage due to the inherent sampling limitations. Alternatively, the incident field can be numerically modeled in terms of Green's function or, it can be retrieved from a certain number of acquisition samples evaluated on the measurement space.

Most of the adopted phaseless microwave imaging strategies, consider the use of complex incident field and of the phaseless total field as input data to the inversion method. The assumption on the incident field is conventionally used in the microwave imaging community, indicating this step as system (i.e., antennas) characterization, that can be performed prior to the imaging task, and thus partially going against the definition of a pure phaseless reconstruction.

Rather than apply the PR stage to the total field, the phase recovery can be exploited for the incident field data. By doing so, combining a single-step phaseless microwave imaging strategy with a PR stage applied to the incident field data only, could lead to a completely phaseless microwave imaging approach. Furthermore, the phase reconstruction error that affects the incident field data reconstruction has a limited impact on the imaging results, as compared to the case where the PR is applied to the total field. According to these considerations, an incident field modeling strategy - i.e, an inverse source method - starting from the amplitude-only acquisition of the incident field is investigated, and further details are provided in Chapter 3. The incident field data retrieved following the proposed phaseless technique, is then included within the Phaseless Contrast Source Inversion (P-CSI) method discussed in Chapter 4.

Chapter 3

Incident Field Analysis in Microwave Imaging Systems

3.1 Inverse Source Problem Applied to a Microwave Imaging Context

In combination with the inverse scattering problems for imaging purposes, the solution of the inverse source problems can be seen as a side problem to be solved. Indeed, inverse source problems embrace the imaging context, since the incident field distribution within the imaging domain is one of the required data to perform inverse scattering, unless the resolvent kernel of the EFIE is obtained as measured Point Spread Function (PSF), incorporating the incident field dot product under the BA condition for the total internal field, as deeply discussed in [39], [40]. Therefore, retrieving the incident field can be seen as an intermediate step toward the solution of the main inverse scattering problem. In order to get the incident field distribution starting from measured data, different established techniques can be used, and most of them take inspiration from antenna characterization. These include Near Field - Far Field (NF-FF) or NF-NF transformations.

In the context of phaseless data, two are the available options for the incident field evaluation:

- Characterize the incident field source directly from amplitude-only data [41];

- Perform a PR step starting from the phaseless data.

Pertaining to the second of the categories listed above, a combined method for the recovery of the incident field distribution within the imaging domain is developed.
This task is accomplished by extending a holography-based method, named as Spatial Domain Indirect Holography Technique (SDIHT), into an imaging context. Indeed, this first step can be seen as a PR stage, limited to the points lying on the measurement domain only. In order to characterize the incident field distribution starting from a limited number of incident field samples, here two families of techniques are discussed, denoted as the Modal Expansion (ME) technique and the Source Reconstruction Method (SRM), whose are described in Section 3.3 and Section 3.4, respectively. Both methods rely on the Huygens' principle, meaning that the field distribution outside a certain contour can be expressed as the combination of a limited number of primary sources (incident fields) or of secondary sources, i.e., equivalent currents. The ME method is based on the assumption that any electromagnetic field solution can be represented by the sum of an orthogonal series of components in the coordinate system of interest [42]–[46]. Consequently, this general statement can be extended to different scenarios: in the planar case, the orthogonal series is composed of plane waves with different amplitudes and propagation directions. In the case of a spherical or cylindrical coordinate system, the fields can be represented as the superimposition of spherical or cylindrical waves, respectively. Although extensively used, the main limitation of the ME based methods is that they cannot be extended to non-canonical geometries. Regarding the SRM, it consists of the determination of the equivalent current densities, evaluated over a closed surface surrounding the Antenna Under Test (AUT). Therefore the SRM can be seen as a more flexible solution, feasible to any geometry domain [47], [48]. Such reconstruction methods generally start from the knowledge of the incident field values in complex terms, evaluated on a certain measurement region; consequently, the prior step based

on the Spatial Domain Indirect Holography Technique (SDIHT) enables the use of those methods even in a phaseless scenario, compensating for the lack of phase content.

3.2 Spatial Domain Indirect Holography Technique (SDIHT) as Phase Retrieval (PR) Stage

Microwave indirect holography techniques have been extensively applied for the determination of the antenna radiation pattern or, for evaluating the NF distribution and fields at the antenna aperture [49]. As opposed to the standard direct holography, in the indirect holography, the field distribution can be obtained by considering scalar field measurements. In view of a phaseless microwave imaging method, an indirect holography solution can be potentially adopted as a PR strategy. More specifically, here the PR stage has been considered as a modified version of the Spatial Domain Indirect Holography Technique (SDIHT) proposed in [50]. The SDIHT directly operates in the spatial domain, avoiding any spectral component analysis of the samples [51]. Starting from intensity measurements only, the SDIHT was originally conceived to retrieve NF distribution on planar surfaces of a generic AUT. Due to the ability to recover the field distribution on arbitrary geometries, in the case of a cylindrical imaging setup, rather than considering a planar surface, the SDIHT can be applied to the measurement points only. Based on this fact, the SDIHT is used as an intermediate step for the incident field characterization, so that the PR capabilities of such a method are used to determine the incident complex data along the bounded measurement domain S, starting from intensity-only measurements. Once the incident field data are obtained through the SDIHT stage, they can be given as input to either the ME and the SRM, previously mentioned in Section 3.1, in order to recover the incident field distribution within the DOI. By doing so, no complex data are involved, resulting in a full phaseless procedure.
Hereafter the details of the SDIHT implementation are discussed. Inspired by [52], this technique assumes three field intensity acquisitions for each fixed RX location.

The three sets of field intensities can be obtained by combining the measured fields with three different reference signals, differing only for the phase shift ϕ imposed along a feedback line; the acquisition scheme is depicted in Fig. 3.1, illustrating the case of a single RX-TX couple.

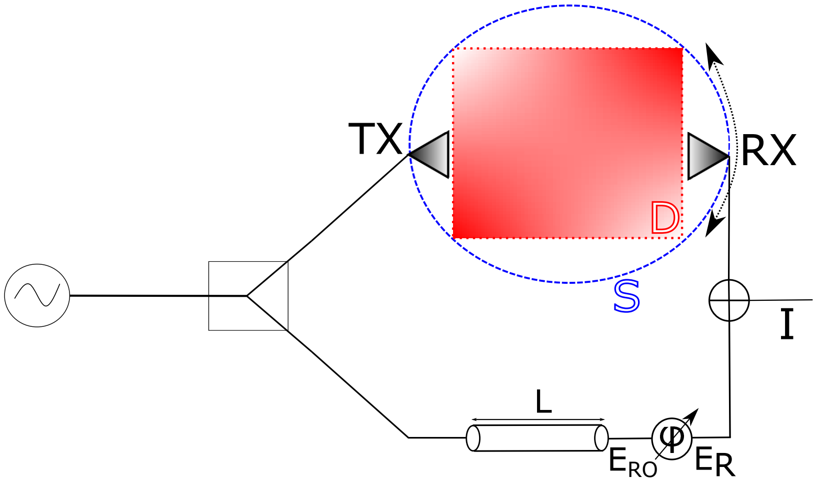

Figure 3.1: Spatial Domain Indirect Holography Technique (SDIHT) scheme, applied to a microwave imaging context, for the phase recovery of the incident field in the measurement domain S.

In this case, the following field intensity measurements can be performed:

$$I_\phi = |E_S^i + E_R^\phi|^2 = |E_S^i + E_{RO}e^{j\phi}|^2, \quad \phi \in (-\pi/2, 0, \pi/2) \tag{3.1}$$

where E_S^i follows the imaging terminology, indicating the (incident) field evaluated along the observation domain S, while E_R^ϕ indicates the *reference* field, after applying the phase contribution ϕ. By formulating Eq. (3.1) with the different values of ϕ, we have:

$$\begin{aligned} I_0 &= |E_S^i| + |E_{RO}| + (E_S^i)^* E_{RO} + E_S^i (E_{RO})^* \\ I_{-\pi/2} &= |E_S^i| + |E_{RO}| - j(E_S^i)^* E_{RO} + jE_S^i (E_{RO})^* \\ I_{\pi/2} &= |E_S^i| + |E_{RO}| + j(E_S^i)^* E_{RO} - jE_S^i (E_{RO})^* \end{aligned} \tag{3.2}$$

where $[\cdot]^*$ indicates the complex conjugate operator.
The corresponding squared amplitude signals in Eq. (3.2) are processed in order to get the incident field phase E_S^i.

According to the details provided in [50], defining the quantities:

$$
\begin{aligned}
A &= I_0 - I_{-\pi/2} \\
&= (E_S^i)^* E_{RO}(1+j) + E_S^i (E_{RO})^* (1-j) \\
B &= I_0 - I_{\pi/2} \\
&= (E_S^i)^* E_{RO}(1-j) + E_S^i (E_{RO})^* (1+j)
\end{aligned}
\tag{3.3}
$$

By combining the expressions in Eq. (3.3):

$$
\begin{aligned}
\frac{A-B}{A+B} &= \frac{2j\left[(E_S^i)^* E_{RO} - E_S^i (E_{RO})^*\right]}{2\left[(E_S^i)^* E_{RO} + E_S^i (E_{RO})^*\right]} \\
&= j\frac{(-2j) Im\{E_S^i (E_{RO})^*\}}{2Re\{E_S^i (E_{RO})^*\}} \\
&= \frac{Im\{E_S^i (E_{RO})^*\}}{Re\{E_S^i (E_{RO})^*\}}
\end{aligned}
\tag{3.4}
$$

We can finally obtain:

$$
\begin{aligned}
\tan^{-1}\left[\frac{A-B}{A+B}\right] &= \tan^{-1}\left[\frac{(I_0 - I_{-\pi/2}) - (I_0 - I_{\pi/2})}{(I_0 - I_{-\pi/2}) + (I_0 - I_{\pi/2})}\right] \\
&= \phi_{E_S^i} - \phi_{E_{RO}}
\end{aligned}
\tag{3.5}
$$

where $\phi_{E_S^i}$ denotes the retrieved phase of the incident field, while $\phi_{E_{RO}}$ indicates a constant phase-shift, which can be compensated assuming the cable length L to be known. For the validation of the reconstruction method, a simple line source, numerically formulated in the form of a Hankel function of the second kind, has been assumed as field source. In Fig. 3.2, the actual phase sampled in a circular fashion is compared to the retrieved phase obtained through Eq. (3.5). This technique can be potentially replaced by other PR methods but, despite the need for three measurement campaigns, it does not need different reference planes to provide the necessary data diversity to perform the PR stage correctly.

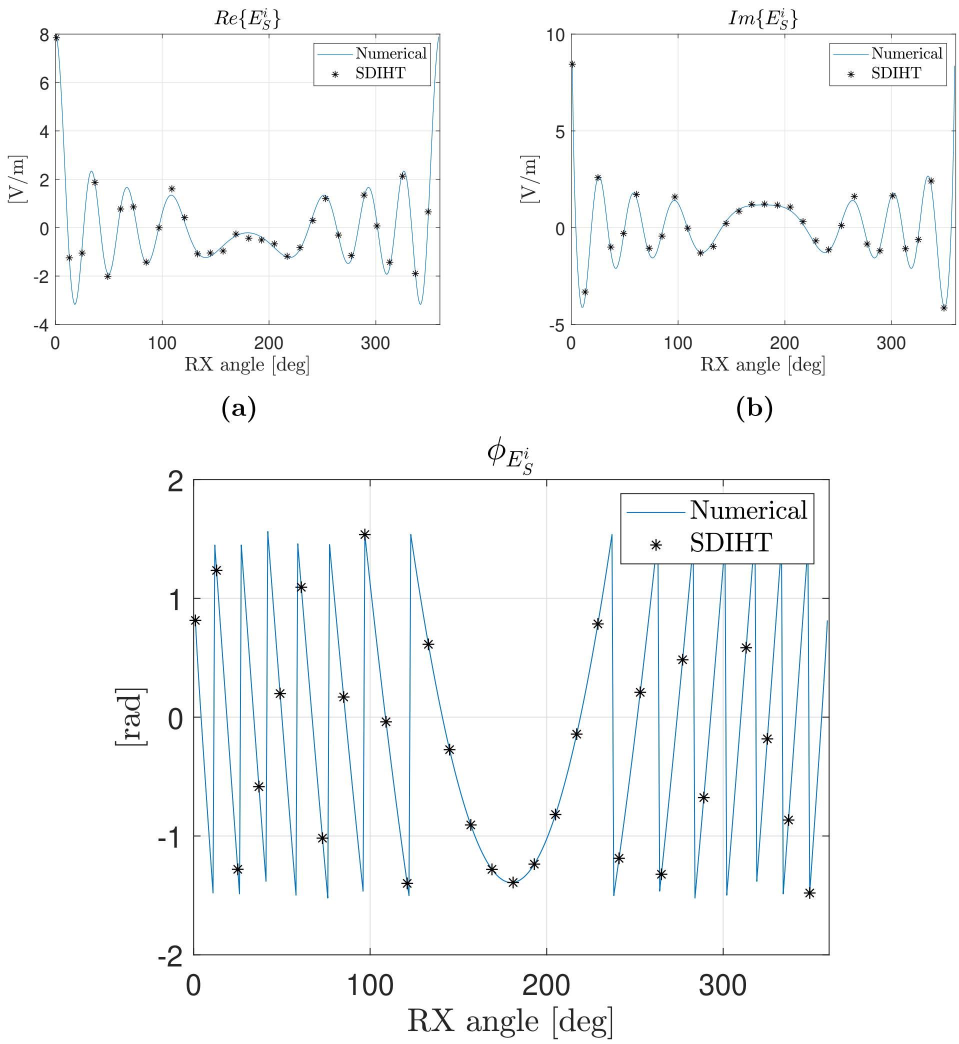

(c)

Figure 3.2: Incident field recovered on sampling points along the measurement domain S, with the Spatial Domain Indirect Holography Technique (SDIHT) - (a) real part, (b) imaginary part, (c) phase.

3.3 Modal Expansion (ME)

According to the ME theory, NF measurements can be decomposed in known propagating wave modes, so that field data can be evaluated on the desired locations. In the case of a cylindrical setup, the field coming from the transmitting antenna can be modelled as a superposition of cylindrical waves. Thus, it can be formulated as a polynomial expansion in terms of Hankel functions of order ν:

$$E^i_{ME}\left(r,\theta\right)=\sum_{\nu=-N_c}^{N_c} c_\nu H^{(2)}_\nu\left(k_b r\right)e^{j\nu\theta} \tag{3.6}$$

where N_c denotes the number of cylindrical waves, (r,θ) are the coordinates of the observation point with respect to the transmitter location, k_b is the wave number in the background, while c_ν are the unknown coefficients. The lower-bound for the truncation number can be selected - as function of the normalized radius $k_b r$ - by analyzing the Hankel function variation with respect to the order ν, so that the most considerable contribution coming from the Hankel basis functions can be included properly [43], [53]. An example of the Hankel function trend (real part) is depicted in Fig. 3.3. The c_ν coefficients are evaluated by minimizing the square distance between the field data, i.e., E^i_S, and the corresponding fields calculated with the expansion in Eq. (3.6). This problem can be re-written in a matrix form and solved in a least square sense:

$$E^i_S=\mathbf{H}c \tag{3.7}$$

where $\mathbf{H}$ is the matrix including the different order Hankel functions. Once the expansion coefficients are known, the incident field in D - E^i_D - can be computed by re-applying Eq. (3.6), considering the discretization grid nodes in D as observations points.
In order to test the predictability of the ME method, the incident field data coming from the SDIHT stage is corrupted by considering an additive noise, according to the following [54]:

$$E^{i_{noisy}}_S=E^i_S+\max\left(E^i_S\right)\frac{\eta}{\sqrt{2}}\left(\theta_1+j\theta_2\right) \tag{3.8}$$

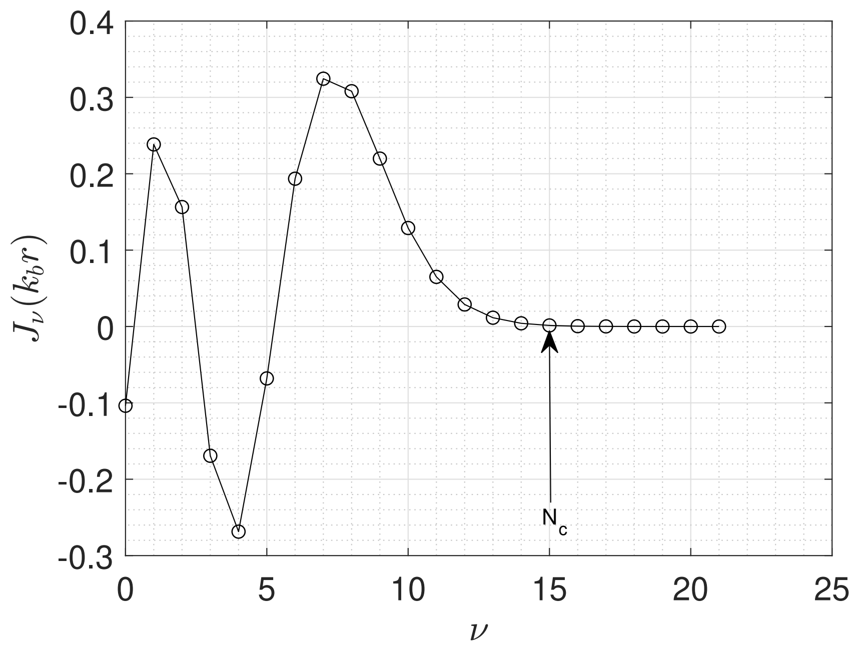

Figure 3.3: Bessel function - $Re\{H_\nu^{(2)}(k_b r)\}$ versus the order ν. The truncation number N_c is highlighted.

where θ_1 and θ_2 are two real random vectors, whose elements range in [-1,1], while η indicates the noise percentage with respect to the maximum field amplitude and here set as $\eta = 10\%$.

The ME technique is validated by considering a line-current source as reference propagating field, defined as:

$$E^i(\mathbf{r}) = \frac{1}{4i} H_0^{(2)}\left(k_b|\mathbf{r} - \mathbf{r}'|\right), \quad \mathbf{r}' \in D \tag{3.9}$$

Considering the transceivers located along a closed curve S with radius $R_{TX} = 3\lambda$, after the PR stage completed with the SDIHT shown in Section 3.2, the retrieved incident field distribution starting from the field data on S is shown in Fig. 3.4, and compared to the numerical model provided in Eq. (3.9). The ME approach has also been tested in the case of non-numerical field source, such as in the case of the field radiated by a Double-Layer Antipodal Vivaldi Antenna (DL-AVA), while operating with the presence of a coupling medium and described in Chapter 5 - Section 5.2.2. The reconstructed field distribution compared to the one imported from CST Studio Suite® is illustrated in Fig. 3.5.

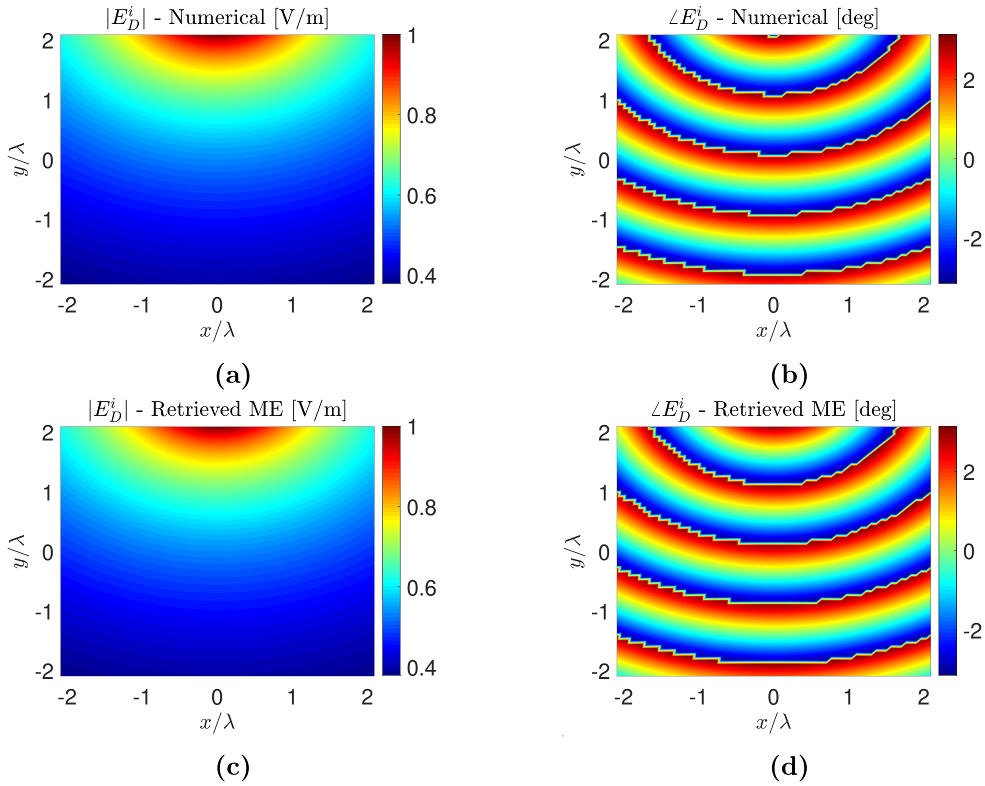

Figure 3.4: Incident field distribution for a line current source - Exact (a) amplitude and (b) phase. Retrieved (c) amplitude and (d) phase with the ME technique.

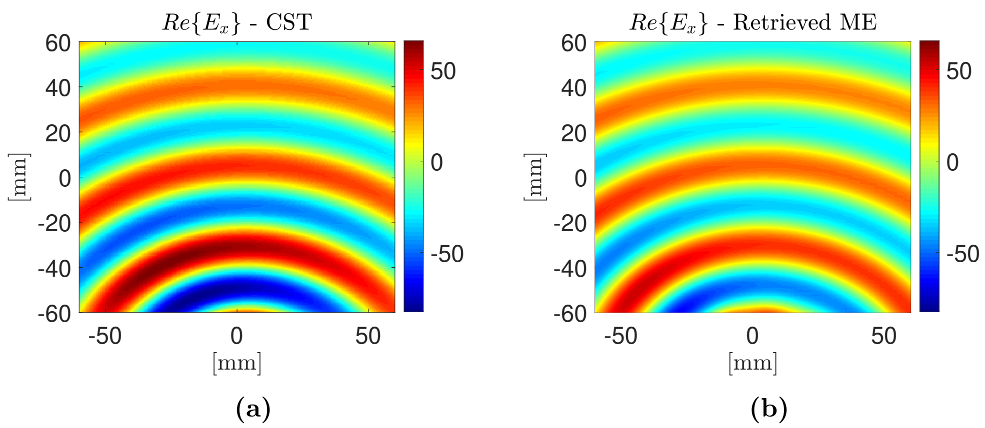

Figure 3.5: Field reconstruction (real part) for the simulated Double-Layer Antipodal Vivaldi Antenna (DL-AVA) discussed in Chapter 5, by applying the combined SDIHT+ME method - (a) CST data, (b) retrieved field.

3.4 Source Reconstruction Method (SRM)

Beside the ME technique described in Section 3.3, the incident field distribution can be obtained by exploiting the Source Reconstruction Method (SRM). Based on the equivalence principle, the SRM, is an integral equation based technique, mainly used in antenna diagnostics, NF-FF transformations and solution of inverse source problems [55], [56]. More specifically, exploiting the equivalence principle, the SRM aims to find out the equivalent current distributions that radiate the same fields as the actual AUT outside the equivalent currents' domain, here consisting of a bounded region surrounding the field source and denoted as S'. The schematic of the SRM scenario is shown in Fig. 3.6.

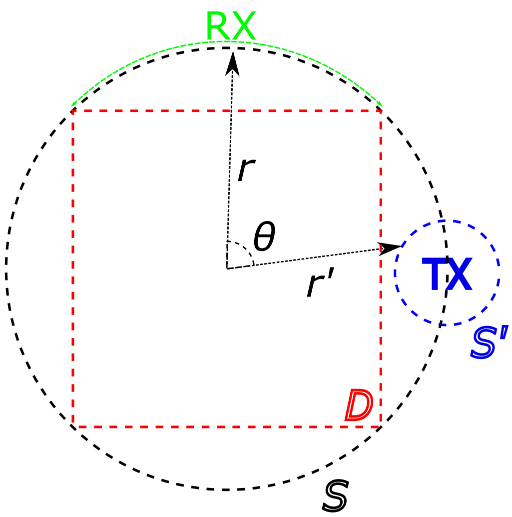

Figure 3.6: Source Reconstruction Method (SRM) - schematic

The method is able to provide an electromagnetic model based on a series of equivalent current distributions, that can be exploited to evaluate the generated field at any points outside S'. The SRM can potentially solve problems that go beyond the classical sampling criteria, but also it is able to solve equivalent currents that are smaller than half a wavelength in size, providing increased resolution features.

The unknown equivalent sources can be defined in a MoM model, while the involved integral operators, correlating the sampled data and the equivalent currents, are based on analytic Green's functions, which provides a stable solution for the inversion of the involved matrix operators.

The flexibility of the method in the sampling space opens to include the SRM in microwave imaging applications [21], [57], by setting the acquisition domain as the incident field measurement space. Once the equivalent currents are obtained, the radiated fields can be determined by using a numerical forward solver. The field radiated by the equivalent currents and evaluated in the measurement domain S can be obtained as:

$$E(\mathbf{r}) = E^{\mathbf{J_S}}(\mathbf{r}) + E^{\mathbf{M_S}}(\mathbf{r}) \tag{3.10}$$

where $E^{\mathbf{J_S}}$ is the field contribution due to the electric current $\mathbf{J_S}$, while $E^{\mathbf{M_S}}$ is the contribution coming from the magnetic current $\mathbf{M_S}$. The two terms included in Eq. (3.10) can be written as:

$$E^{\mathbf{J_S}}(\mathbf{r}) = -\frac{j\eta_b}{4\pi k_b}\int_{S'}\left(k_b^2+\nabla^2\right)\left(\mathbf{J_S}(\mathbf{r}')\frac{e^{-jk_b|\mathbf{r}-\mathbf{r}'|}}{|\mathbf{r}-\mathbf{r}'|}\right)\mathbf{dS}' \tag{3.11}$$

$$E^{\mathbf{M_S}}(\mathbf{r}) = -\frac{1}{4\pi}\nabla\times\int_{S'}\left(\mathbf{M_S}(\mathbf{r}')\frac{e^{-jk_b|\mathbf{r}-\mathbf{r}'|}}{|\mathbf{r}-\mathbf{r}'|}\right)\mathbf{dS}' \tag{3.12}$$

The Transverse Magnetic (TM) condition allows us to assume the existence of the z-component of the electric current - J_S^z, and of the two orthogonal magnetic currents, i.e., M_S^x and M_S^y. Therefore, recalling the fundamental solution of the Helmholtz equation for the generic cylindrical case as:

$$G(\boldsymbol{\rho}) = \frac{1}{4i}H_0^{(2)}(k_b\boldsymbol{\rho}) \tag{3.13}$$

And neglecting the E-field components lying on the x-y plane, the expression of the electric field due to the current J_S^z can be obtained by manipulating Eq. (3.11), resulting in [57]:

$$E_z^{J_S^z}(\mathbf{r}) = -\frac{\omega\mu_0}{4}\int_{S'}J_S^z(\mathbf{r}')\,H_0^{(2)}(k_b|\mathbf{r}-\mathbf{r}'|)\,\mathbf{dS}' \tag{3.14}$$

While the contributions due to M_S^x and M_S^y are taken from Eq. (3.12), and written as:

$$E_z^{M_S^x}(\mathbf{r}) = -\frac{1}{4j}\int_{S'}M_S^x(\mathbf{r}')\,k_bH_1^{(2)}(k_b|\mathbf{r}-\mathbf{r}'|)\,\frac{(y-y')}{|\mathbf{r}-\mathbf{r}'|}\mathbf{dS}' \tag{3.15}$$

$$E_z^{M_S^y}(\mathbf{r}) = \frac{1}{4j}\int_{S'} M_S^y(\mathbf{r}')\, k_b H_1^{(2)}(k_b|\mathbf{r}-\mathbf{r}'|)\, \frac{(x-x')}{|\mathbf{r}-\mathbf{r}'|}\mathbf{dS}' \tag{3.16}$$

Consequently, the z-component of the electric field can be obtained as the sum of the three contributions in Eqs. (3.14) to (3.16) coming from the equivalent currents, for an arbitrary point outside S'.

As for the discretization of the integral operators, by considering a pulse-wave basis function, the continuous operators among Eqs. (3.14) to (3.16) are discretized as:

$$\begin{bmatrix} A_{J_S^z} & A_{M_S^x} & A_{M_S^y} \end{bmatrix} \begin{bmatrix} J_S^z \\ M_S^x \\ M_S^y \end{bmatrix} = E_z \tag{3.17}$$

where $A_{J_S^z}$, $A_{M_S^x}$, $A_{M_S^y}$ denote the operators acting on the unknown currents, while the field sampled at the receiver locations can be seen as the superimposition of the three contributions, resulting in:

$$E_z = E_z^{J_S^z} + E_z^{M_S^x} + E_z^{M_S^y} \tag{3.18}$$

Each element in Eq. (3.18) has the following size:

$$\begin{aligned} &A_i \rightarrow [N_{RX} \times M \times N_{TX}], \quad i = J_S^z, M_S^x, M_S^y \\ &J_S^z, M_S^x, M_S^y \rightarrow [M \times N_{TX}] \\ &E_z \rightarrow [N_{RX} \times \; N_{TX}] \end{aligned} \tag{3.19}$$

where M is the number of discretization points pertaining to the S' domain, on which the equivalent currents are evaluated. The problem shown in Eq. (3.17) can be solved by considering different methods. In the case under test, due to the over-determination of the system, a Conjugate Gradient for Least Square (CGLS) method[1] has been implemented to solve Eq. (3.17). The iterative CGLS algorithm aims to solve the following:

$$\arg\min_{\mathbf{x}} \; \|\mathbf{Ax} - \mathbf{b}\|_2 \tag{3.20}$$

where **A**, **x** and **b** are the elements provided in Eq. (3.17) in a compact form, with the current distributions to be intended as unknown.

[1]The strategy has been selected among the regularization tools provided in the *regtools* MATLAB package [58].

By solving Eq. (3.20), the current distributions surrounding the transmitter location that produce the smallest squared error at the receiving locations are found. The iteration of the CGLS is stopped manually, i.e., by considering the L-curve method [59]. The L-curve method is a visually inspecting technique for the regularization of ill-posed problems. In a typical L-curve plot, the norm of the solution, i.e., $\|\mathbf{x}\|_2$, is plotted versus the residual norm of the problem, i.e., $\|\mathbf{Ax} - \mathbf{b}\|_2$. The resulting curve assumes an L-curve shape, indicating the trade-off in minimizing the residual and reducing the size of the solution at the increase of the number of iterations, since as the iteration progresses, the norm of the solution can become large. Therefore, the solution localized at the corner of the L-curve is conventionally selected as the optimal solution, as shown in the example depicted in Fig. 3.7.

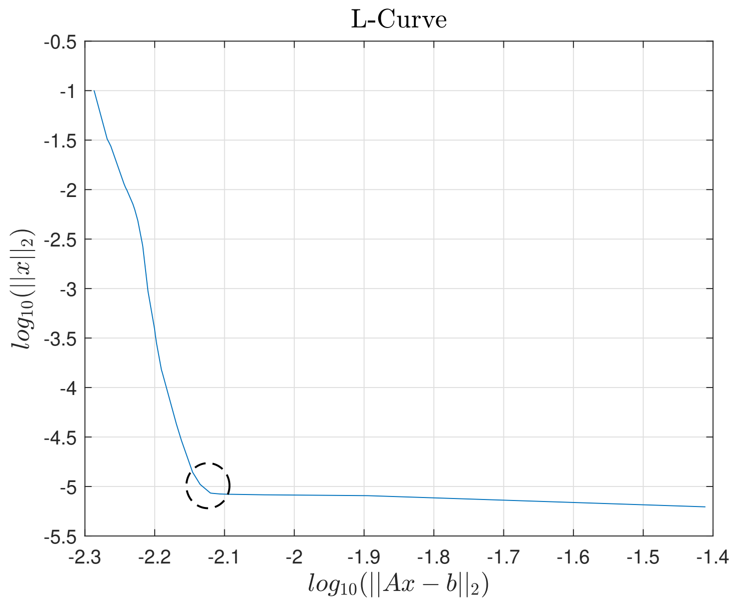

Figure 3.7: Example of L-curve trend and highlighted *knee*, for the solution of the problem described in Eqs. (3.17) and (3.20).

In the case of a cylindrical measurement setup, the setup symmetry suggests inspecting the L-curve for a single transmitter position only, thus assuming to be valid for the other transmitter locations. Once the set of equivalents current is found, the radiating field evaluated according to the relations in Eqs. (3.14) to (3.16), is firstly compared to the one coming from the SDIHT stage, or from a numerical model, considering the sampling points lying on S. An example of a reconstructed field from the equivalent currents, in the case of a TM line source, is shown in Fig. 3.8.

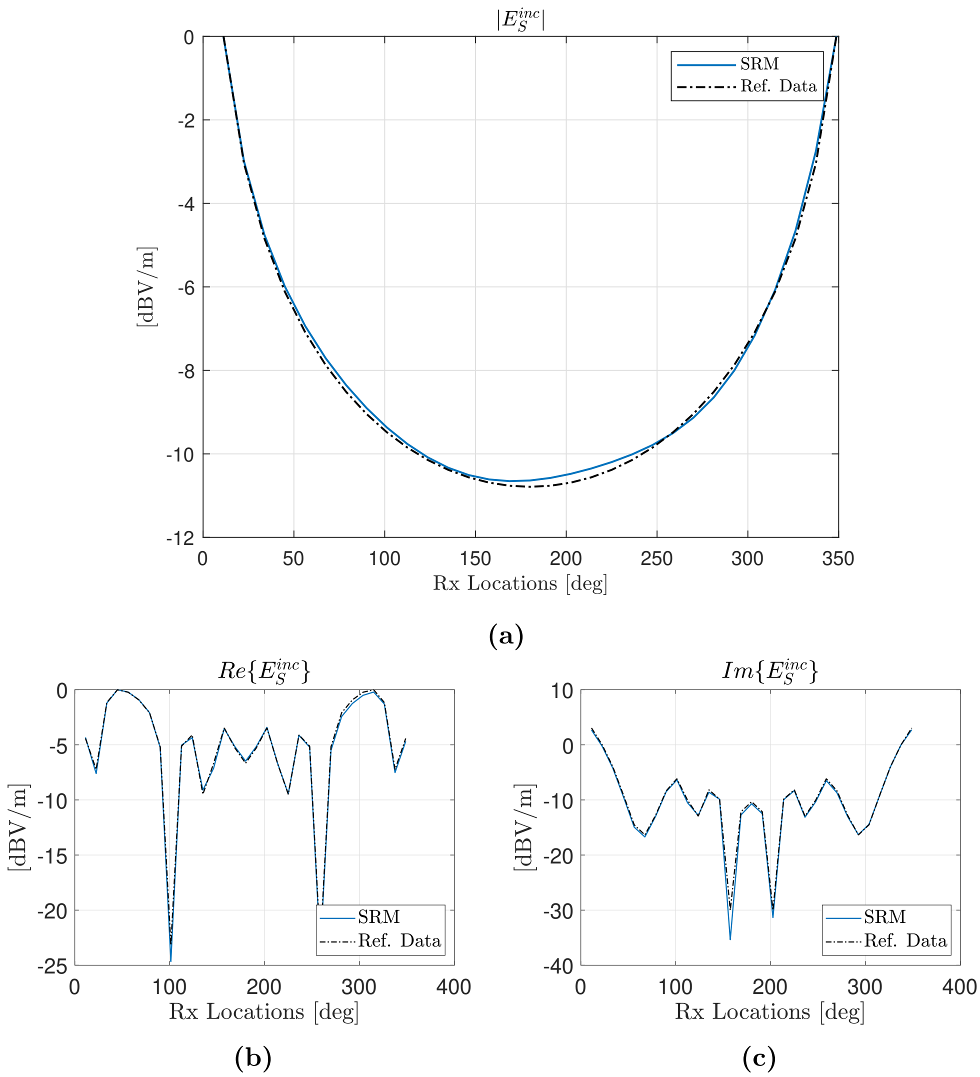

Figure 3.8: Example of the field generated by the SRM equivalent currents, compared to the reference field, in the case of a TMz line source. (a) Amplitude, (b) real and (c) imaginary parts. All the quantities are expressed in dBV/m and evaluated on the measurement domain S.

For the validation of the SRM technique, different numerical radiating sources are considered. Aside from the source type, the incident field reconstruction inside the DOI is obtained within a whole phaseless scheme, since the field distribution is retrieved starting from complex data terms in S, obtained via the SDIHT applied to phaseless measured data, as discussed in Section 3.2. The retrieved incident field along the measured curve given by the SDIHT method is then given as input to the SRM method. A generalized expression of a directive source is used as a test case, for a certain focus level m as reported in [60], [61]:

$$E^{inc}(\mathbf{r}) = \frac{1}{4i} H_0^{(2)}\left(k_b\left|\mathbf{r}-\mathbf{r}'\right|\right)\left[\cos(\theta)\right]^m \tag{3.21}$$

where θ is the angle between the observation point and the antenna boresight direction; in the case of $m = 0$, Eq. (3.21) is reduced to the omnidirective source case.

The incident field inside the DOI is reconstructed for different focus levels m, evaluated on the $x - y$ plane, orthogonal with respect to the line source direction, i.e., z. Those fields are compared to the numerical model, considering the following normalized error as metric:

$$\delta = \frac{\|E^{inc}_{retrieved} - E^{inc}_{numerical}\|_D}{\|E^{inc}_{numerical}\|_D} \tag{3.22}$$

The retrieved amplitude in the case of non-directive source ($m = 0$) is shown and compared to the numerical reference in Fig. 3.9, whereas reconstruction examples for more directive sources are reported, in the case of $m = 2$ (Fig. 3.10), $m = 4$ (Fig. 3.11) and $m = 6$ (Fig. 3.12). For the latter, the comparison with the numerical case of Eq. (3.21) along four different cuts is shown in Fig. 3.13.

The metric indicated in Eq. (3.22), evaluated for the different focusing levels m, is summarized in Table 3.1. The use of either the SRM and the ME, combined with the SDIHT method proposed in Section 3.2, is exploited as incident field characterization and included in the P-CSI method, described in Chapter 4 and later applied to the breast imaging case, as discussed in Chapter 5.

Table 3.1: Reconstruction error for different focus levels m.

Focus level - m	δ [%]
0	2.5
2	4.31
4	8.68
6	13.20

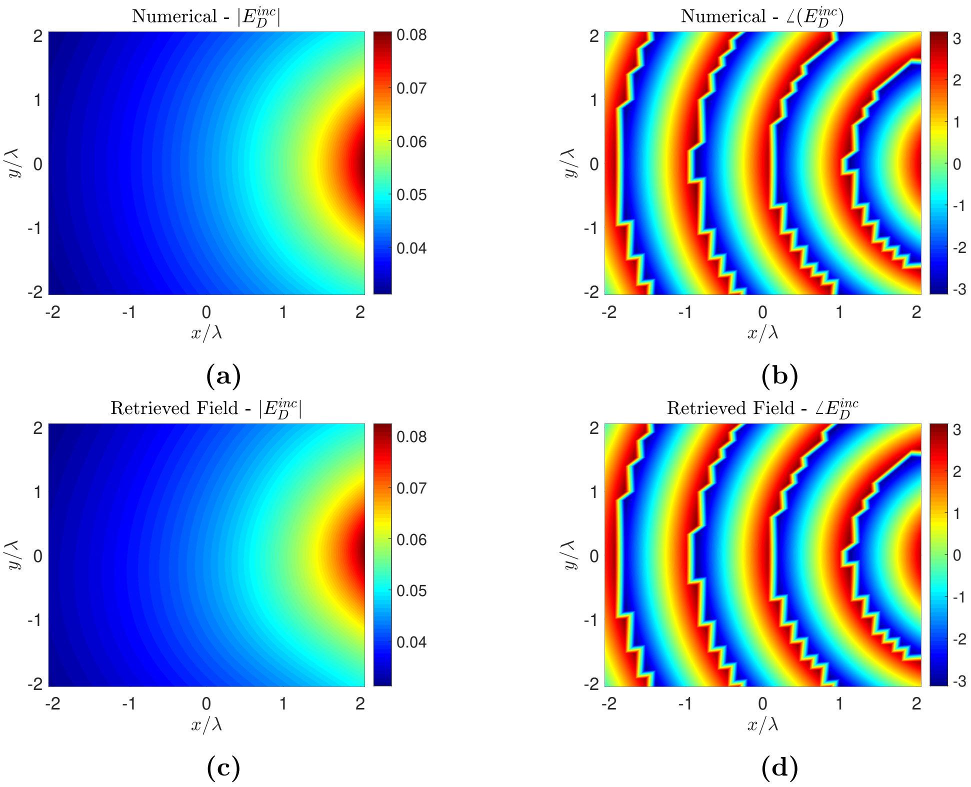

Figure 3.9: Source Reconstruction Method (SRM) - Incident field distribution for $m = 0$ (line source). Numerical (a) amplitude and (b) phase. Retrieved (c) amplitude and (d) phase.

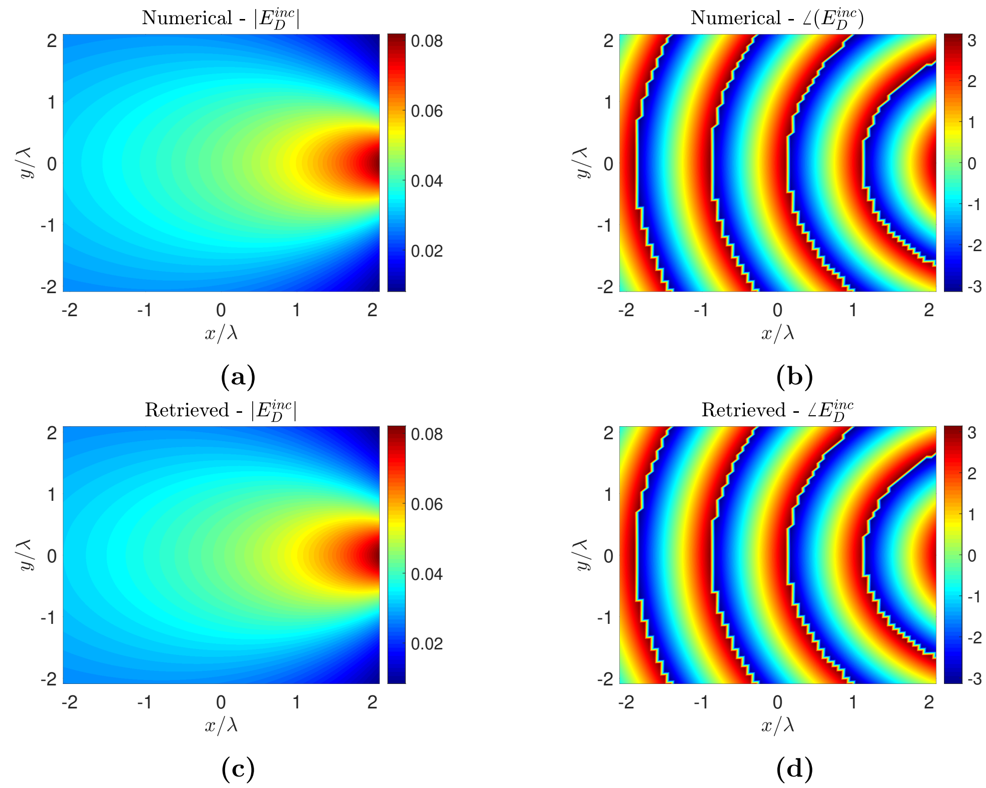

Figure 3.10: Source Reconstruction Method (SRM) - Incident field distribution for $m = 2$. Numerical (a) amplitude and (b) phase. Retrieved (c) amplitude and (d) phase.

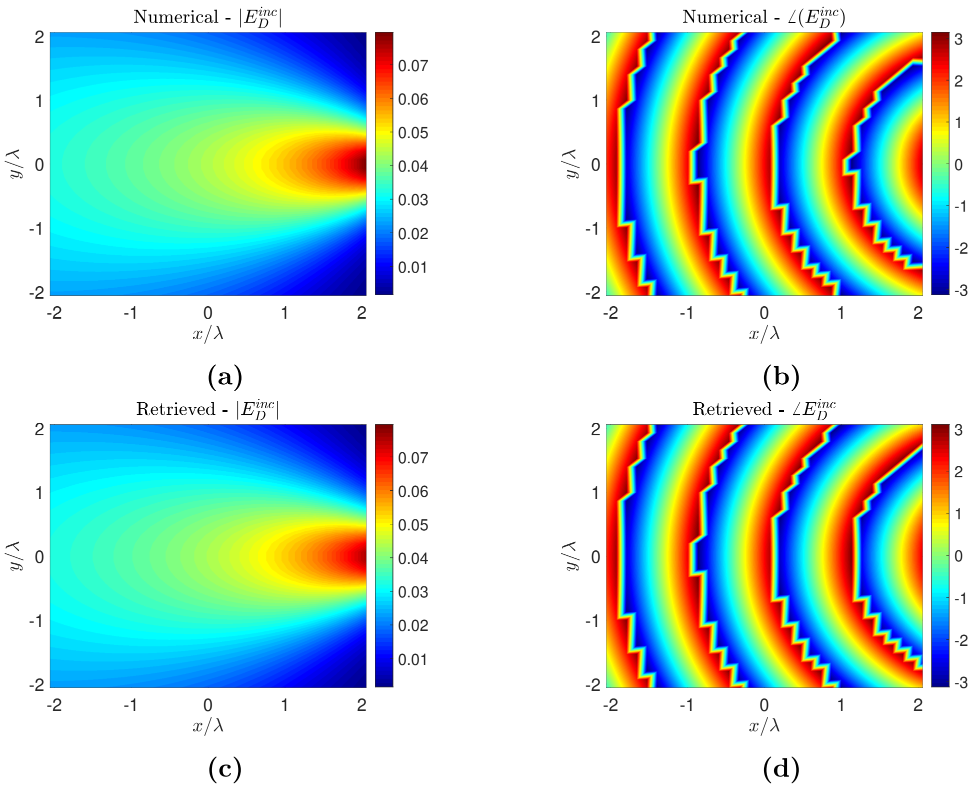

Figure 3.11: Source Reconstruction Method (SRM) - Incident field distribution for $m = 4$. Numerical (a) amplitude and (b) phase. Retrieved (c) amplitude and (d) phase.

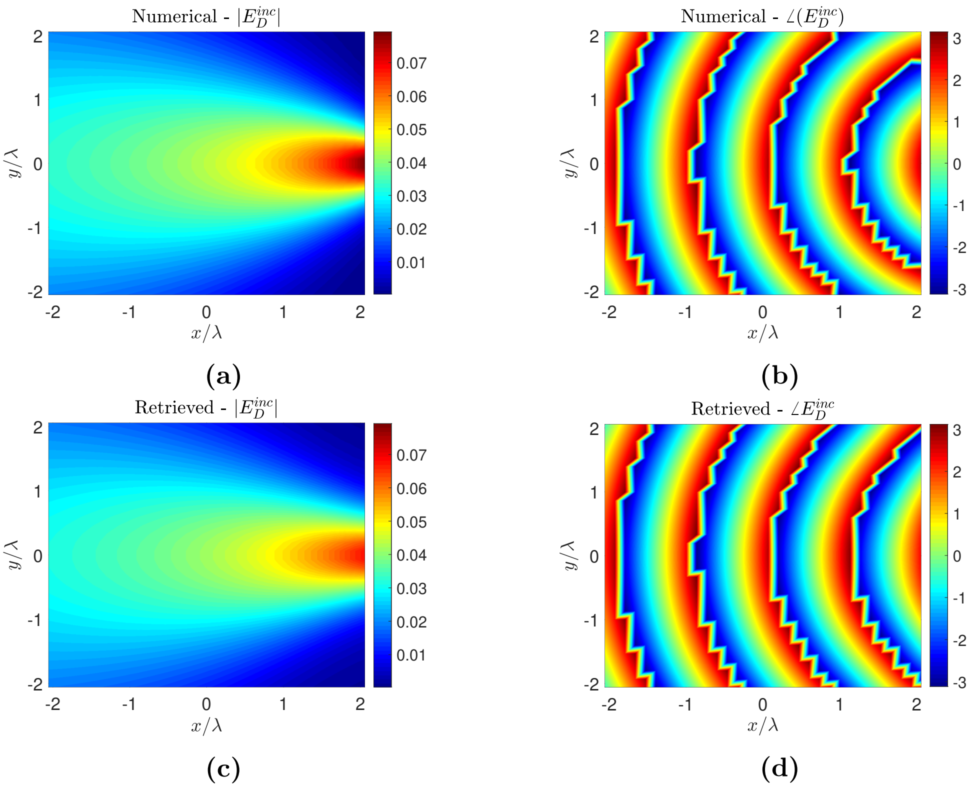

Figure 3.12: Source Reconstruction Method (SRM) - Incident field distribution for $m = 6$. Numerical (a) amplitude and (b) phase. Retrieved (c) amplitude and (d) phase.

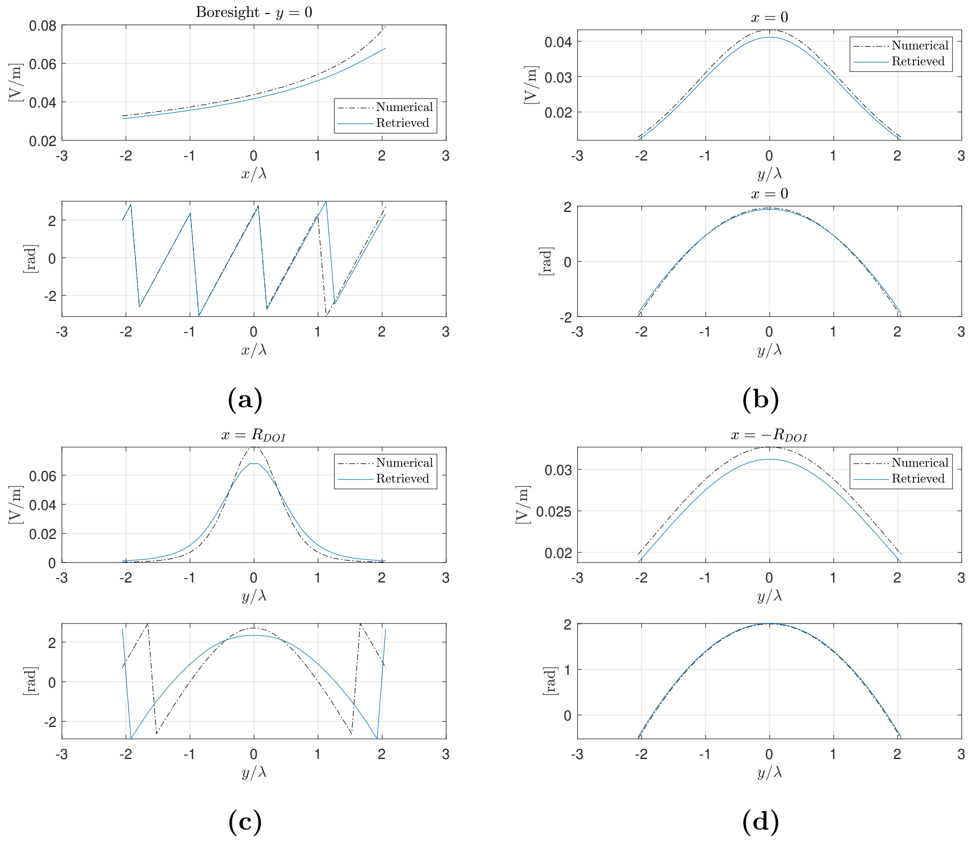

Figure 3.13: Incident field distribution for $m = 6$ on different cutting planes - (a) $y = 0$, (b) $x = 0$, (c) $x = R_{DOI}$ and (d) $x = -R_{DOI}$, where $R_{DOI} = 3\lambda$.

Chapter 4

Inverse Scattering Solution with Phaseless Data

4.1 Phaseless Contrast Source Inversion (P-CSI) Method

Once the incident field characterization from phaseless data is completed by following the combined approach discussed in Chapter 3, the inverse scattering problem needs to be effectively solved. In this chapter, a phaseless iterative inverse scattering strategy is discussed. Pertaining to the locally based solutions, the inverse scattering problem is solved in an iterative fashion. A proper cost function is defined and, according to the CSI formulation, this can be expressed at the n^{th} step as:

$$\begin{aligned} F(\chi^{(n)}, w_v^{(n)}) &= F_S(w_v^{(n)}) + F_D(w_v^{(n)}, \chi^{(n)}) \\ &= \alpha_S \sum_{v=1}^{N_{TX}} \left|\left| r_{S,v}^{(n)} \right|\right|_S^2 + \alpha_D \sum_{v=1}^{N_{TX}} \left|\left| \rho_{D,v}^{(n)} \right|\right|_D^2 \end{aligned} \tag{4.1}$$

where α_{S-D} is a normalization factor. The cost function in Eq. (4.1) consists of a linear combination of two different terms: the first one - $F_S(w_v^{(n)})$ - named as *data function*, considers the discrepancy between the total field, evaluated on the measurement domain S and the corresponding modeled field. For the case at hand, only total field intensity values are evaluated and, for a fixed transmitting position v, it results to be (*data residual*):

$$r_{S,v}^{(n)} = |E_{S,v}^{tot}|^2 - |E_{S,v}^{mod(n)}|^2 \tag{4.2}$$

where the modeled field $E_{S,v}^{mod(n)}$ can be easily obtained from the first of the EFIE in the CS formulation stated in Eq. (2.8):

$$E_{S,v}^{mod(n)} = E_{S,v}^{inc} + G_S w_v^{(n)} \tag{4.3}$$

The incident field term can be derived by considering the SDIHT method described in Section 3.2. The second term in Eq. (4.1) - $F_D(w_v^{(n)}, \chi^{(n)})$ - denotes the error which affects the second of Eq. (2.8) in the imaging domain D and it is indicated as *state function*. This term follows the traditional formulation, also valid in the case of complex data availability, so that for a fixed transmitter it can be defined as (*state residual*):

$$\rho_{D,v}^{(n)} = \chi^{(n)}[E_{D,v}^{inc} + G_D w_v^{(n)}] - w_v^{(n)} \tag{4.4}$$

The solution of the inverse scattering problem follows the CSI formulation [62], [63]. The inverse scattering problem aims to alternately find the contrast source $w = E_D^{tot}\chi$ and the dielectric contrast χ. The pseudocode of the inverse strategy is reported in Fig. 4.1. This process first involves an iterative implementation of the Conjugate Gradient (CG) scheme, in order to evaluate the contrast source w for a fixed value of the contrast χ at the n^{th} step.

The contrast source at the n^{th} step is obtained by following the CG update:

$$w_v{}^{(n)} = w_v{}^{(n-1)} + \alpha_v{}^{(n)} d_v{}^{(n)} \tag{4.5}$$

where α is the step length, and d is the conjugate gradient direction, updated as:

$$d_v{}^{(n)} = g_v{}^{(n)} + \gamma^{(n)} d_v{}^{(n-1)} \tag{4.6}$$

with g denoting the gradient of the cost functional F, while γ is the Polak-Ribière parameter for the direction update [64], whereas v indicates the different incident directions, i.e., $v \in \{1, 2, \ldots, N_{TX}\}$.

1: **procedure** INITIALIZATION
2: $w_v^{(0)}$, $\chi^{(0)}$, ${E^{tot}}_v^{(0)}$ ▷ Initial guess and starting values
3: **procedure** CS UPDATE
4: *Calculate*:
$\nabla F = g_v^{(n)}$ ▷ Cost Function Gradient
5: $\gamma^{(n)}\ (g_v^{(n)},\ g_v^{(n-1)})$ ▷ Polak-Ribiére
6: $d_v^{(n)} = g_v^{(n)} + \gamma^{(n)} d_v^{(n-1)}$ ▷ Direction Update
7: $\alpha^{(n)}$ ▷ Learning Rate
8: $w_v^{(n)} = w_v^{(n-1)} + \alpha^{(n)} d_v^{(n)}$ ▷ **CS Update scheme**
9: **procedure** CONTRAST UPDATE
10: ${E^{tot}}_v^{(n)} = E_v^i + G_D w_v^{(n)}$ ▷ Total Field Update
11: $\chi^{(n)}({E^{tot}}_v^{(n)}, w_v^{(n)}) = \underset{\chi^{(n)}}{\text{argmin}}\ F_{D_n}$ ▷ **Contrast Update**
12: **procedure** COST FUN. UPDATE
13: *Calculate*:
$r_v^{(n)}, \rho_v^{(n)}$ ▷ Data/State Residuals
14: $F_n = F_{S_n}(r_v^{(n)}) + F_{D_n}(\rho_v^{(n)})$
15: **procedure** CONV. CRITERIA
16: $n = n + 1$
17: **if** $F_n < tol \vee n > n_{max}$ **then**
18: *STOP*
19: **else**
20: **go to** 3

Figure 4.1: Phaseless Contrast Source Inversion (P-CSI) - pseudocode.

Due to the structure of the cost functional F, the relative gradient with respect to the contrast source w can be split into two parts, namely g_S and g_D, for the data cost functional F_S and the state cost functional F_D, respectively. For convenience in notation, the dependency on the transmitter location v is omitted. Both gradients are evaluated by considering the Fréchet derivative of the function under investigation. The derivative is here calculated for the data cost functional only, since the calculation in the case of the g_D is analogous. For a fixed transmitting location, and evaluating the involved fields on the $m \in \{1, 2, \ldots, N_{RX}\}$ positions, the Fréchet derivative for the not normalized version of the F_S functional can be written as [65]:

$$\begin{aligned} \lim_{\epsilon \to 0} \frac{1}{\epsilon} \Bigg[\sum_{m=1}^{N_{RX}} \left| |E_S^{tot}|^2 - |E_S^{inc} + G_S(w^{(n)} + \epsilon g_S^{(n)})|^2 \right|^2 \\ - \sum_{m=1}^{N_{RX}} \left| |E_S^{tot}|^2 - |E_S^{inc} + G_S w^{(n)}|^2 \right|^2 \Bigg] \end{aligned} \tag{4.7}$$

By using the expressions provided in Eqs. (4.2) and (4.3), we have:

$$\begin{aligned} \lim_{\epsilon \to 0} \frac{1}{\epsilon} \sum_{m=1}^{N_{RX}} |r_S^{(n)} - 2\epsilon Re\{(\overline{E_S^{inc} + G_S w^{(n)}}) G_S g_S^{(n)}\} + O(\epsilon^2)|^2 - |r_S^{(n)}|^2 \\ = -4Re \sum_{m=1}^{N_{RX}} r_S^{(n)} (\overline{E_S^{inc} + G_S w^{(n)}}) G_S g_S^{(n)} \\ = -4Re \sum_{m=1}^{N_{RX}} (\overline{g_S^{(n)}}) G_S^{\star} (E_S^{mod(n)} r_S^{(n)}) \end{aligned} \tag{4.8}$$

In Eq. (4.8) the property of the norm operator is used, i.e., $\|a+b\|^2 = \|a\|^2 + \|b\|^2 + 2Re\{\overline{a}b\}$, with $\overline{[\cdot]}$ denoting the complex conjugate operator, while $[\cdot]^{\star}$ indicates the adjoint operator.

The last term of Eq. (4.8) has its maximum variation when:

$$g_S^{(n)} = G_S^{\star} \left(E_S^{mod(n)} r_S^{(n)} \right) \tag{4.9}$$

The expression of the gradient for the not normalized functional F_D is calculated in a similar fashion:

$$\begin{aligned} &\lim_{\epsilon \to 0} \frac{F_D\left(w^{(n)} + \epsilon g_D^{(n)}\right) - F_D\left(w^{(n)}\right)}{\epsilon} = \\ &-2Re\left\{\sum_{m=1}^{N_{RX}} \overline{g_D^{(n)}}\left[\rho_D^{(n)} - G_D^{\star}(\overline{\chi^{(n)}}\rho_D^{(n)})\right]\right\} \end{aligned} \tag{4.10}$$

The Fréchet derivative in Eq. (4.10) has its maximum for:

$$g_D^{(n)} = \rho_D^{(n)} - G_D^{\star}(\overline{\chi^{(n)}}\rho_D^{(n)}) \tag{4.11}$$

where we consider $\rho_D^{(n)}$ as in Eq. (4.4).

Once the contrast source at the n^{th} stage is obtained considering the expression in Eq. (4.5) and the total field in D is updated accordingly (line 10 - pseudocode), the dielectric contrast χ can be updated as the minimizer of the state function only - F_D (line 11 - pseudocode). Therefore:

$$\begin{aligned} \chi^{(n)}(E_{v,n}^{tot}, w_v^{(n)}) &= \underset{\chi^{(n)}}{\operatorname{argmin}}\, F_{D_n} \\ &= \frac{\sum_{v=1}^{N_{TX}} w_{v,n}\overline{E_{v,n}^{tot}}}{\sum_{v=1}^{N_{TX}} \left|E_{v,n}^{tot}\right|^2} \end{aligned} \tag{4.12}$$

The required incident field E_D^{inc} included in the total field update stage is obtained by using the incident field recovery strategy described in Chapter 3.
Once the contrast is determined through Eq. (4.12), an additive regularization layer is included in the contrast update stage, implementing a Total Variation (TV) function, corresponding to the discretized version of the following [65]:

$$F_R^{(n)}(\chi) = \frac{1}{A}\int_D \frac{|\nabla\chi(r)|^2 + \delta^{(n)}}{|\nabla\chi^{(n)}(r)|^2 + \delta^{(n)}} dA \tag{4.13}$$

where A indicates the area of the imaging domain, while $\delta^{(n)} = \frac{F(\chi^{(n)})}{\Delta x \Delta y}$ represents the steering parameter that controls the weight of the regularization as a function of the number of iterations, with $\Delta x \Delta y$ denoting the discretized mesh size.

Indeed, the regularization factor in Eq. (4.13) approaches 1 for large values of $\delta^{(n)}$, while the regularization effect increases with the number of iterations. Therefore, by directly relating the steering parameter to the cost function F, allows to increase the regularization effects as the cost function decreases - i.e., as the iteration number increases. Conversely, it has almost no effect in the early stage of the inversion, namely for large values of the cost function and hence of $\delta^{(n)}$. This approach prevents the need for a regularization parameter to be selected manually.

An extra feature of the inverse method is here highlighted. The term $E_S^{mod(n)}$ that appears within the expression of the gradient portion g_S in Eq. (4.9), used in the CS update scheme, represents the *modeled* total field obtained in the iterative stage, as function of the contrast source at the n^{th} iteration [65]. Therefore, the lack of phase information content results to be partially compensated within the iterative update procedure of the contrast source, by exploiting the modeled (and not measured) total field in its complex form.
Here the scattered total field data due to the presence of one of the breast models illustrated in Chapter 5[1] is considered as validating example. The data coming from the forward solver - whose phase is not used in the P-CSI routine, is compared to the total field $E_S^{mod(n)}$ obtained at the end of the iterative stage and coming from the scattering model, in both amplitude (Fig. 4.2) and phase (Fig. 4.3), for the different N_{TX} locations. A more compact indication of the discrepancy between the forward solver data and the retrieved total field is shown in Fig. 4.4. Similar results can be obtained when considering different targets. Consequently, if the convergence is achieved, the P-CSI, aside from the permittivity profile of the object, is also able to implicitly retrieve, at the end of the CS update stage, the total field in complex form among the measurement points.

[1]Breast ID: 010204 - from the University of Wisconsin Cross-Disciplinary Electromagnetics (UWCEM) Laboratory - Numerical Breast Phantom Repository [66].

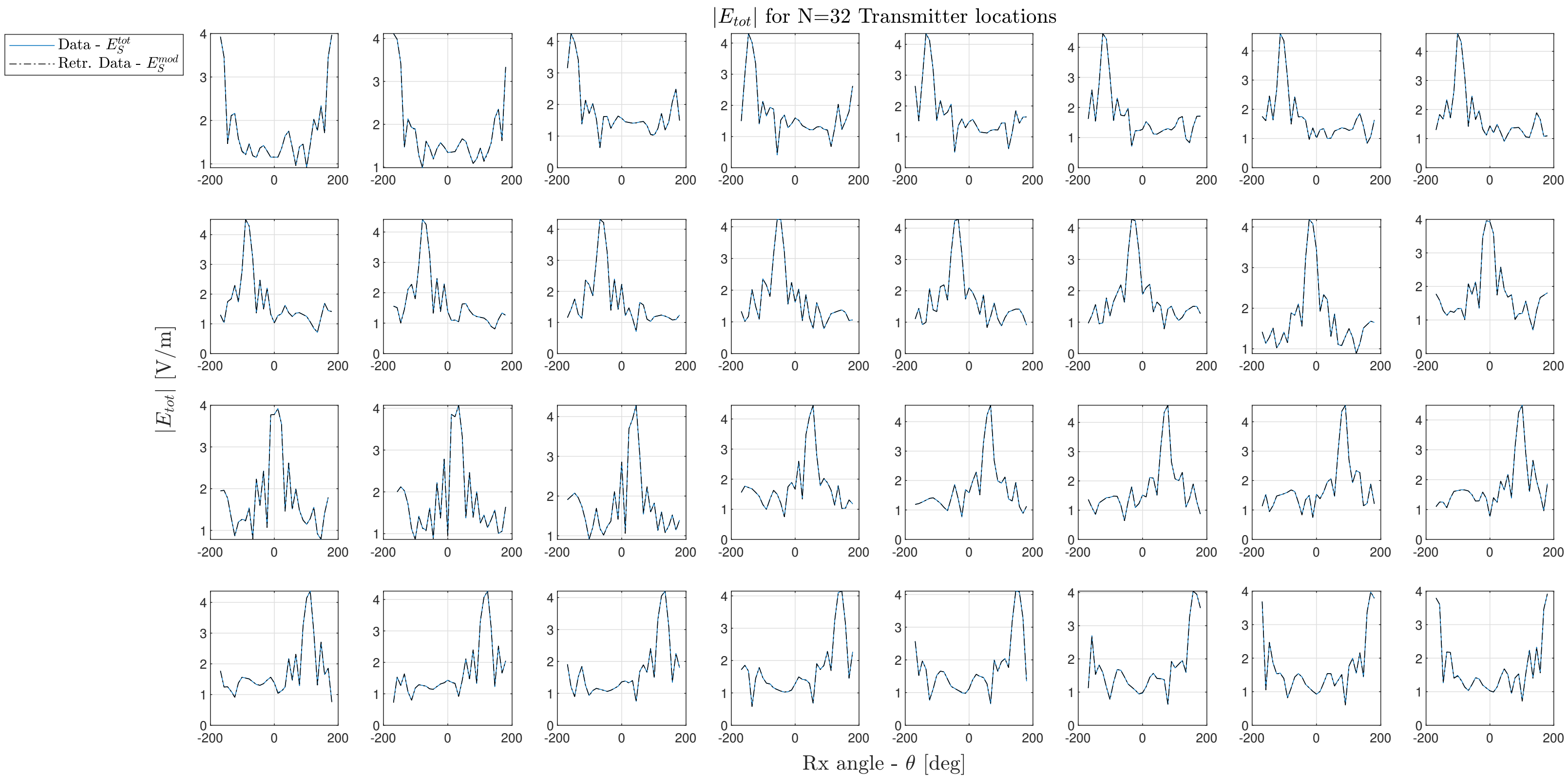

Figure 4.2: Example of total field retrieved amplitude - $|E_S^{mod(n)}|$ - and total field amplitude coming from the forward solver - $|E_S^{tot}|$.

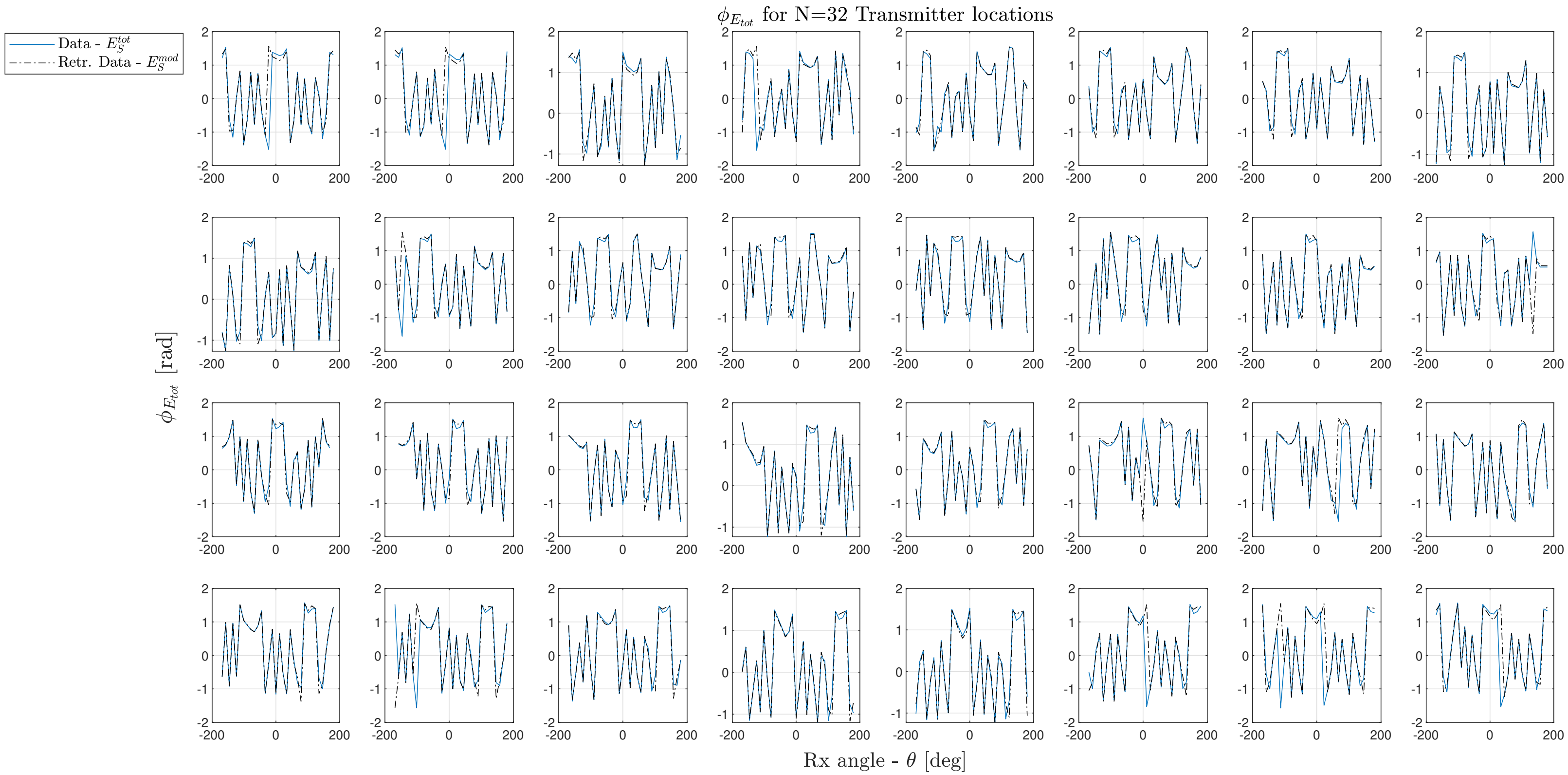

Figure 4.3: Example of total field retrieved phase - $\phi_{E_S^{mod(n)}}$ - and total field phase coming from the forward solver - $\phi_{E_S^{tot}}$.

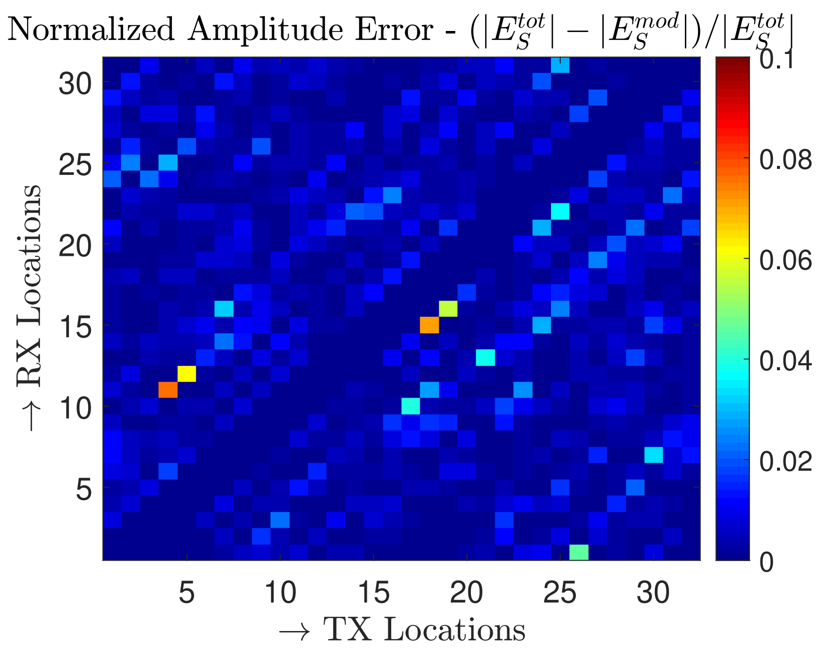

(a)

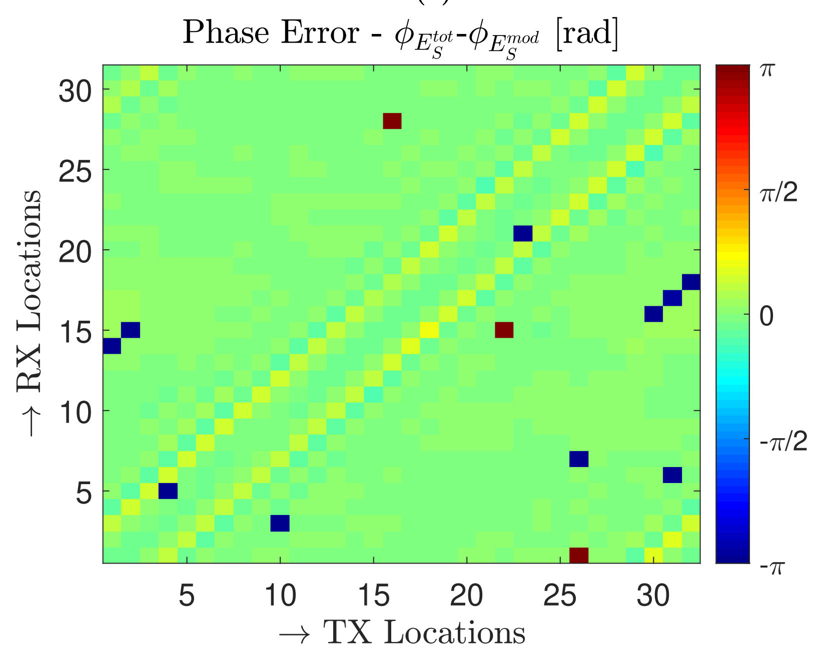

(b)

Figure 4.4: Reconstruction error of the total field (a) amplitude and (b) phase, for the different transceiver locations - compact form of the results shown in Figs. 4.2 and 4.3.

4.2 On the Initial Guess and Prior Information: Amplitude Only Data Case

Several techniques have been proposed among researchers to include some prior information about the OUT. Those approaches consider the use of Ultra-wide Band (UWB) radar techniques [67] or alternatively, the inclusion of prior information coming from other imaging modalities, such as Ultrasound (US) tomography [68], or Magnetic Resonance Imaging (MRI), that can provide details about the inner structure of the target. Those are included as spatial information, so that the dielectric properties to be reconstructed are assumed to be confined within a defined limited region. Those kinds of approaches are generally implemented in the form of a regularization layer [69]. Despite the promising results obtainable by implementing those strategies, the need for a multimodal imaging system for the inverse process remains the main drawback. Alternatively, prior information can be inferred as an inhomogeneous background medium [70]; consequently, for this case, when considering iterative solutions, the contrast, as well as the Green's operator, needs to be refined within each step [71], [72].

Among the different microwave-based strategies, the Orthogonality Sampling Method (OSM) [73]–[76] and the Linear Sampling Method (LSM) [77] can be adopted to find out preliminary qualitative information about the target shape and support. Those qualitative procedures generally consider an indicator function, defined on the domain of interest (DOI), able to discern if a spatial point lies inside or outside the target's support. In the case of OSM, an intensity pattern can be obtained by starting from the definition of a *reduced* scattered field, as a result of the scalar product between the measurements of the far-field pattern and a test function - usually selected as the Green's function - in order to check their orthogonality. Consequently, higher values are expected in the case of points included in the target's support. Originally thought for far-field measurements, the OSM has also been recently investigated in the NF region as deeply discussed in [78]. Other methods put some explicit constraints on the contrast function or alternatively, induce numerical bounds to the unknown contrast values. Nonetheless, the CSI methods are known to depend on the initial guess selected for the contrast source w, as a consequence of the local optimization solution. Different approaches are conventionally used to come up with this aspect; one consists of the definition of prior *estimation* of the average expected permittivity profile and of the internal field, assumed to be equal to the incident field [29]:

$$w^{(0)} = \chi_{av} E_D^{inc} \tag{4.14}$$

Alternatively, BP solutions can be adopted starting from the scattered field data [79]. If the first approach brings some strong assumptions, i.e. the prior knowledge of expected object permittivity and of the incident field distribution, the second one is not applicable in the case of amplitude-only measurements, unless arbitrary values of the total field phase are considered [19], so that the scattered field portion can be extracted. Consequently, a suitable strategy needs to be investigated so that the available limited phaseless data can be used as prior information about the target's support. A Phaseless backpropagation (PBP) method has been considered in the P-CSI framework, inspired by the work presented in the case of MRI-based inverse scattering problems and proposed in [80]. The definition of the BP has been tailored for the case of phaseless data, by minimizing the data cost function F_S only, following a steepest-descent method and limiting it to the first step. Once the gradient of the data cost function is found as in Eq. (4.9), the initial guess of the CS auxiliary unknown w can be obtained as:

$$w^{(0)} = -\beta_0 g_S^{(-1)} \tag{4.15}$$

where $g_S^{(-1)}$ is the gradient evaluated when $w = w^{(-1)} = 0$. With this assumption, by setting Eq. (4.15) in Eq. (4.3) and combine it within Eq. (4.9), the gradient at this step is simply equal to:

$$g_S^{(-1)} = G_S^{\star}[E_S^{inc}(|E_S^{tot}|^2 - |E_S^{inc}|^2)] \tag{4.16}$$

where β_0 denotes an optimal step length, obtained as minimization of the data function F_S, when the contrast source is imposed to be equal to the one in Eq. (4.15):

$$\arg\min_{w} F_S(w^{(0)}) = \arg\min_{w} F_S(-\beta_0 g_S^{(-1)}) \tag{4.17}$$

Using the Euler chain rule [65], the following cubic expression is solved for the step β_0 as the solution for the minimization of Eq. (4.17):

$$2\beta_0^3 \,\|A\|_S^2 - \beta_0^2 (A|B)_S + \beta_0 (\|B\|_S^2 - 2(A|C)_S) + (B|C)_S = 0 \qquad (4.18)$$

where $([\cdot]|[\cdot])$ is the inner product for the measurement domain S, while the other terms are defined as:

$$A = |G_S g_S^{(-1)}|^2 \qquad (4.19)$$

$$B = 2Re\left\{ E_S^{inc} \overline{G_S g_S^{(-1)}} \right\} \qquad (4.20)$$

$$C = |E_S^{tot}|^2 - |E_S^{inc}|^2 \qquad (4.21)$$

The real-root solution of the cubic expression in Eq. (4.18) is selected as the step-length term for the initial guess of the CS. This approach can be repeated for all the transmitters, obtaining a set of N_{TX} initial guesses for the CS pertaining to each transmitting position.
Recalling that the CS - for a selected transmitter - is defined in terms of dielectric contrast - χ - as:

$$w = \chi E_D^{tot} \qquad (4.22)$$

where E_D^{tot}, in the case of the initial guess, this becomes:

$$E_{D_0}^{tot} = E_D^{inc} + G_D w^{(0)} \qquad (4.23)$$

while the initial dielectric contrast, according to its expression given in Eq. (4.12), becomes:

$$\chi_0 = \frac{\sum_v w_v^{(0)} \overline{E_{v_{D_0}}^{tot}}}{\sum_v E_{v_{D_0}}^{tot}} \qquad (4.24)$$

The complex incident field data that appear in Eq. (4.16) and Eq. (4.23) can be assumed numerically known, or, alternatively obtained according to the amplitude-only scheme discussed in Chapter 3. The potential of the CS initial guess in Eq. (4.15), coming from the PBP solution, has been verified on different types of targets.

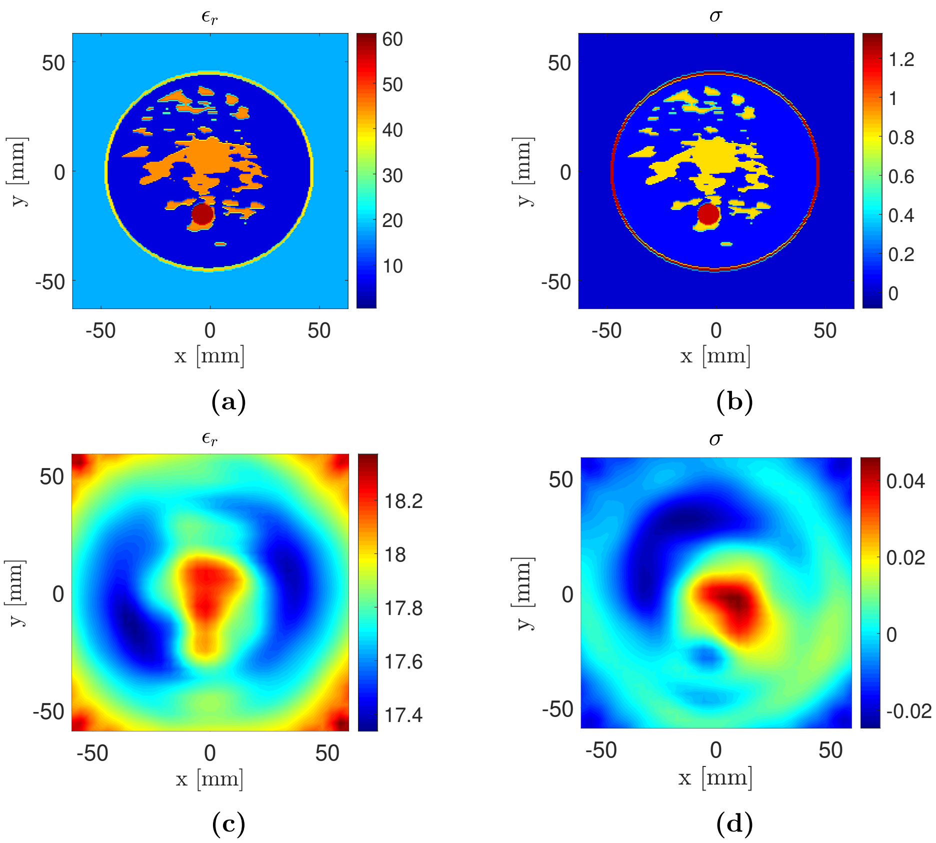

Figure 4.5: Example of initial guess for a Class 2 breast model: (a)-(b) breast model ground truth and (c)-(d) corresponding Phaseless backpropagation (PBP) initial guess.

In the field of breast imaging, the PBP solution has been tested for different breast models. An example of the corresponding permittivity profile coming from the initial guess χ_0, when considering the breast model depicted in Figs. 4.5a and 4.5b, is shown in Figs. 4.5c and 4.5d. Consequently, the PBP initial guess solution results to be an informative initial solution, making use of the total field intensity, with no prior assumption on the nature of the scatterer or on its expected dielectric properties and support, even when considering heterogeneous targets.

4.3 Error Metrics

The quantitative aspects of the retrieved permittivity versus the ground truth profile are generally evaluated with a series of standard error criteria. Here the Root Mean Square Error (RMSE) [81] and the correlation coefficient ρ [72] with respect to the ground truth are evaluated and defined as follows:

$$\begin{aligned} RMSE :&= \sqrt{\frac{\sum_{i=1}^{N_{grid}} x_{est} - x_{true}}{N_{grid}}} \\ \rho_x &= \frac{x_{true} \cdot x_{est}}{\|x_{true}\| \cdot \|x_{est}\|} \end{aligned} \tag{4.25}$$

where x_{est} and x_{true} denote the retrieved and the actual quantity under investigation, respectively, while N_{grid} is the number of the discretization points within the DOI.

4.4 Point Spread Function (PSF) and Sensitivity Analysis

Prior to any imaging reconstructions, the inverse scattering problem solution is tested by considering a point-like scatterer. This task is accomplished by analyzing the Point Spread Function (PSF) of the system. The PSF has been evaluated by considering the scattering of a circular probe, localized at the center of the imaging system. The geometry of the scatterer, with a radius below $\lambda/8$ [39] - where λ is the wavelength in the background medium - guarantees a uniform incident field on the scatterer cross-section. As for the contrast, a $\Delta\chi = 1$ is assumed. The 3 dB lobe of the resulting impulse response is evaluated, indicating how a point-like target is imaged and how much it is potentially spread by the system. Then, the Sidelobe level (SLL) is assumed as second indicator. To assess the stability of the method, those indicators are evaluated for different SNR values, simulated by considering an Additive White Gaussian Noise (AWGN) to the involved electric fields. The ideal PSF in the case of noiseless data and in the case of an SNR of 20 dB are shown in Fig. 4.6a and Fig. 4.6b, respectively. The resulting metrics values as function of SNR are shown in Table 4.1.

According to the results shown in Fig. 4.7, the spatial resolution feature of the method results to be stable even in the case of noisy measurements.

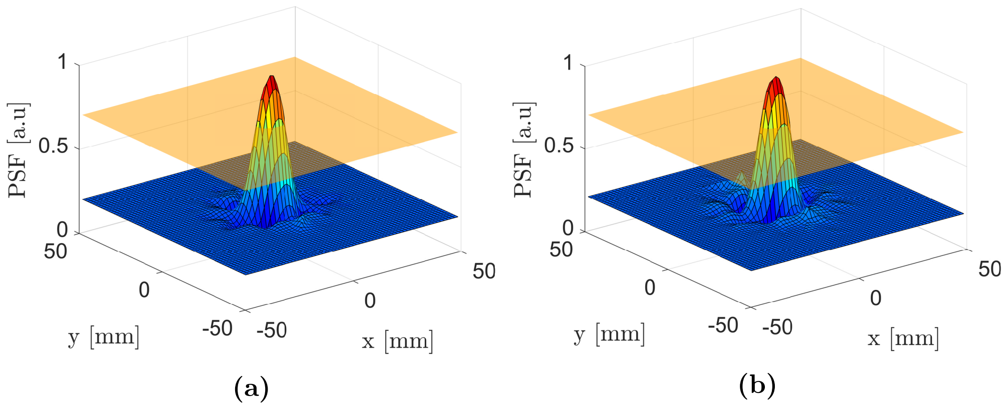

Figure 4.6: Point Spread Function (PSF) of the imaging system and -3 dB cutting plane, with (a) noiseless data, (b) SNR = 20 dB.

Table 4.1: Point-like scatterer - performance indicators for different SNR values.

SNR [dB]	Axis	3 dB lobe	SLL [dB]
20	x	0.387λ	-6.50
	y	0.252λ	-5.45
30	x	0.365λ	-6.82
	y	0.247λ	-6.08
40	x	0.346λ	-8.11
	y	0.235λ	-6.94
60	x	0.332λ	-8.35
	y	0.233λ	-7.15

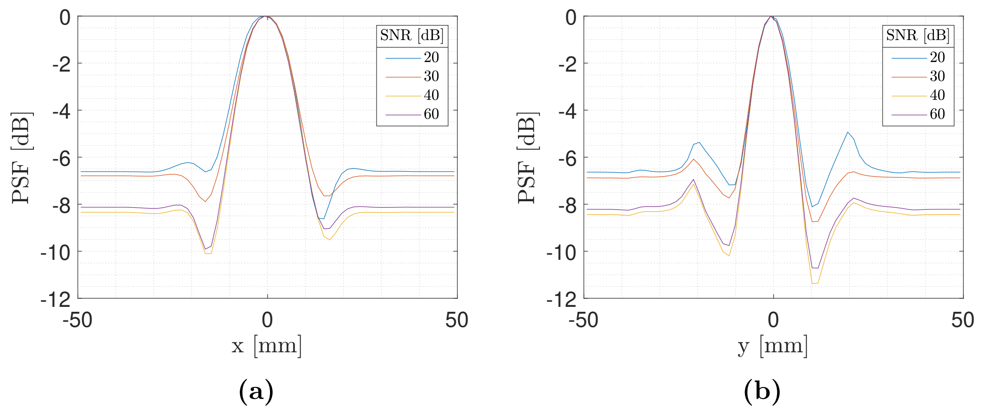

Figure 4.7: Point Spread Function (PSF) for different SNR values - (a) y = 0 and (b) x = 0 cuts.

Before considering targets with high dielectric contrast and high heterogeneity, a sensitivity analysis needs to be performed in the case of canonical-shaped targets with different sizes and contrast. Here, a square-shaped target is assumed to be located at the center of the imaging domain. A parameter analysis is performed considering different contrasts, as well as different sizes l. The reconstruction is performed assuming a PBP initial guess as derived in Section 4.2, whereas the imaging configuration assumes an imaging domain with size 2.26λ. The number of transceivers is set to $N = 32$, while a background with $\epsilon_{r_b} = 18$, $\sigma_b = 0.01$ S/m is considered. The involved E-field data have been corrupted with AWGN, resulting in SNR=20 dB. The properties of the different squared targets are summarized in Table 4.2; for each table entry, the reconstruction results are reported.

Table 4.2: Parameter settings for the sensitivity analysis. For each (l, ϵ_r) entry, the (normalized) RMSE and the correlation factor ρ are evaluated.

(l, ϵ_r)	$1.5\epsilon_{r_b}$		$2\epsilon_{r_b}$		$3\epsilon_{r_b}$	
	$\frac{RMSE}{\epsilon_{r_b}}$	ρ	$\frac{RMSE}{\epsilon_{r_b}}$	ρ	$\frac{RMSE}{\epsilon_{r_b}}$	ρ
0.5λ	0.057	0.994	0.103	0.995	0.21	0.979
0.7λ	0.075	0.997	0.15	0.991	0.26	0.973
0.8λ	0.065	0.997	0.17	0.988	0.316	0.960
λ	0.34	0.953	0.203	0.982	0.421	0.939

The reconstruction of the sub-wavelength targets is illustrated in Fig. 4.8. For all the reconstructions, good correlations with the ground-truth scenario are achieved, with limited artifacts in the background region. The RMSE values are instead consistent with the limitation of the CSI-based methods.

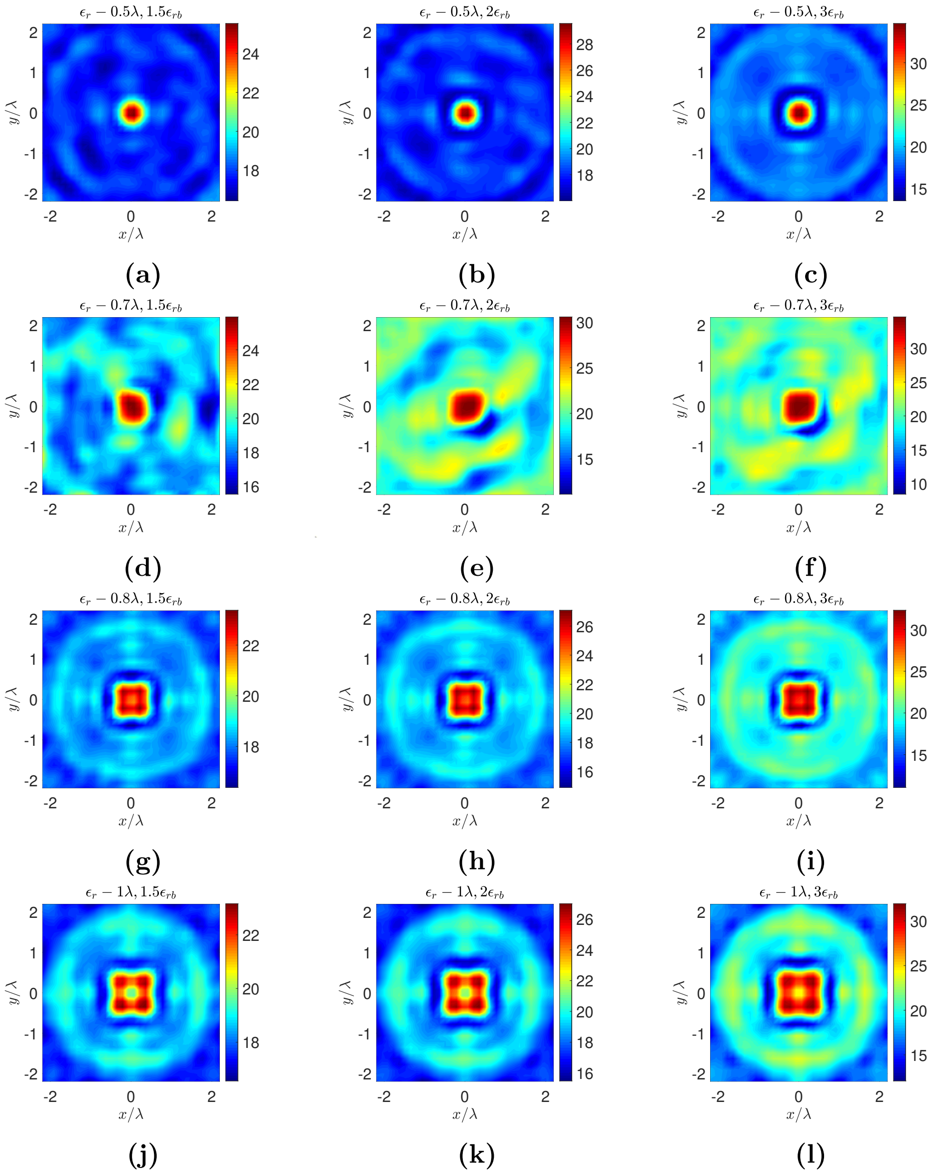

Figure 4.8: Square-shaped targets with ϵ_r as indicated in Table 4.2, for different square sizes l - 0.5λ (first row), 0.7λ (second row), 0.8λ (third row), λ (fourth row) and permittivity ϵ_r - $1.5\epsilon_{r_b}$ (first column), $2\epsilon_{r_b}$ (second column), $3\epsilon_{r_b}$ (third column).

4.5 Phaseless Reconstruction and Experimental Data

In order to test the non-linear inverse strategy on experimental data, the P-CSI reconstruction algorithm detailed in Section 4.1 has been tested by using the dataset provided by the Institut Fresnel - Marseille, whose acquisition setup (Fig. 4.9) is discussed in [82], [83] and can be summarized as follows:

- Transmitter distance from the setup center: 720 ± 3 mm;
- Transmitting angles (target rotation): $\theta_T \in (0°, 350°)$ in steps of 10°;
- Receiver distance from the setup center: 760 ± 3 mm;
- Receiving angles: $\theta_R \in (60°, 300°)$ in steps of 5°.

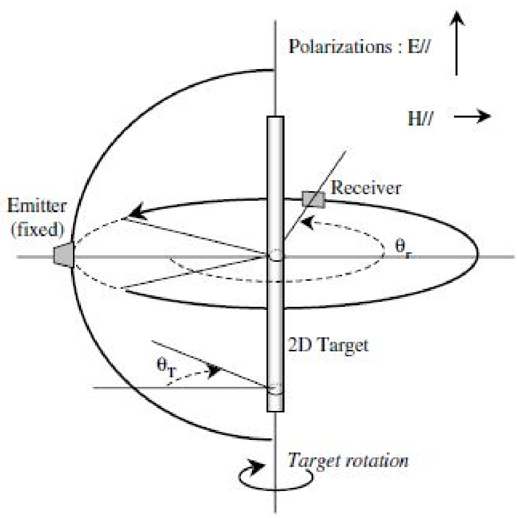

Figure 4.9: Bistatic measurement setup, taken from [82].

For all the targets, air is assumed as homogeneous background, hence $\epsilon_{r_b} = 1$. Specifically, the reconstruction method is first tested on the following cylindrical-shaped targets (Fig. 4.10):

- *diel* - a homogeneous cylinder with diameter $\oslash = 30$ mm and $\epsilon_r = 3 \pm 0.3$;
- *twodiel* - two identical homogeneous cylinders;
- *ushaped* - a metallic cylindrical *u-shaped* target.

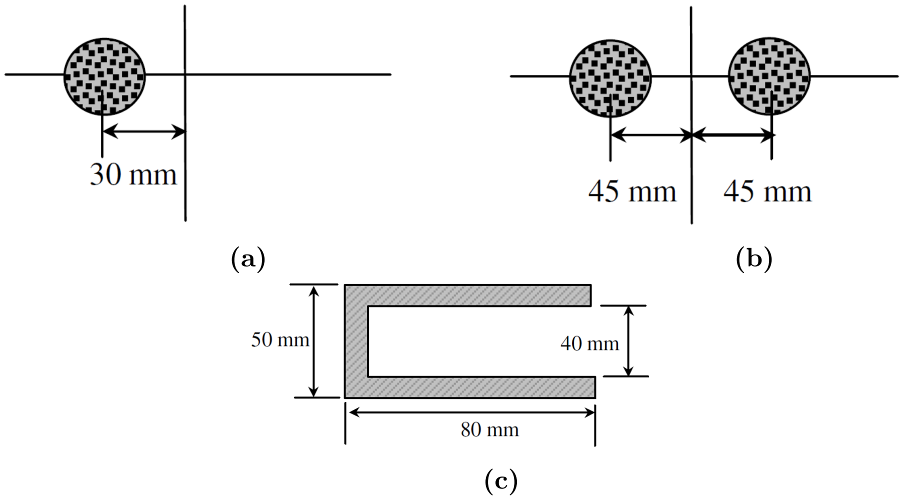

Figure 4.10: (a) *diel*, (b) *twodiel* and (c) *ushaped* cylindrical targets - transverse section [82].

The reconstruction results have been compared to a series of full-data CSI-based inversion techniques. Those include the standard CSI, the Multiplicative Regularized Contrast Source Inversion (MR-CSI) [84] and the Cross-correlated Contrast Source Inversion (CC-CSI) provided in [85]. The reconstruction methods are evaluated and compared to the P-CSI, as shown in Figs. 4.11 to 4.13, for the three different test cases.

Secondly, the P-CSI is evaluated in the case of an inhomogeneous cylinder and two different homogeneous cylinders adjacently arranged, named as *FoamDielInt* and *FoamDielExt*, respectively [83]. The involved cylinders have size $\oslash_1 = 80$ mm, $\oslash_2 = 31$ mm, with a relative permittivity $\epsilon_{r1} = 1.45 \pm 0.15$ (foam) and $\epsilon_{r2} = 3 \pm 0.3$ (plastic), respectively. The two targets and the corresponding reconstruction results are shown in Fig. 4.14.

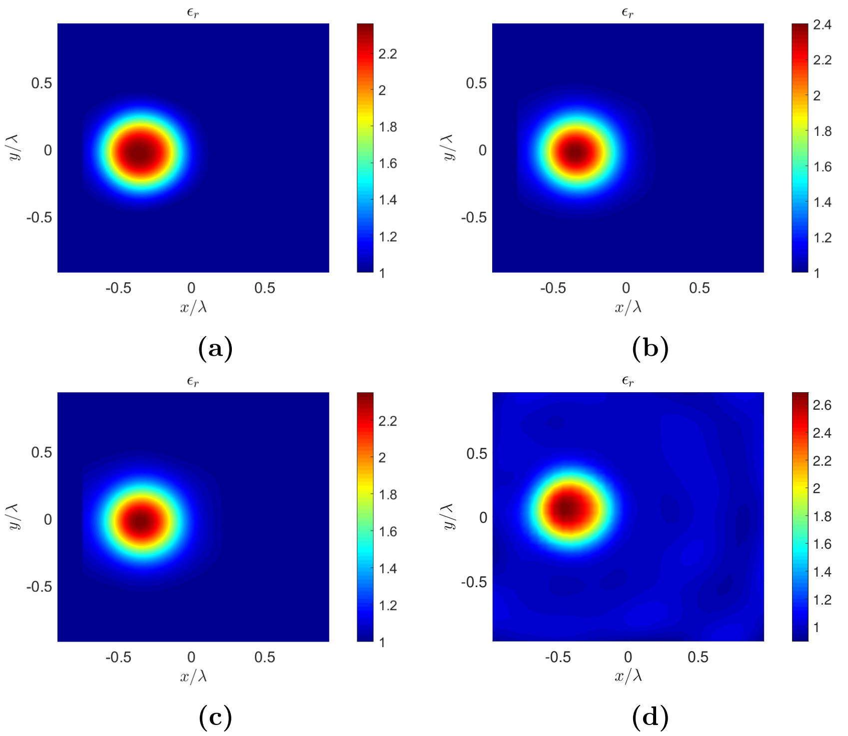

Figure 4.11: *diel* dielectric target defined in [82]. Permittivity map for (a) CSI, (b) MR-CSI, (c) CC-CSI and (d) P-CSI, with f = 4 GHz.

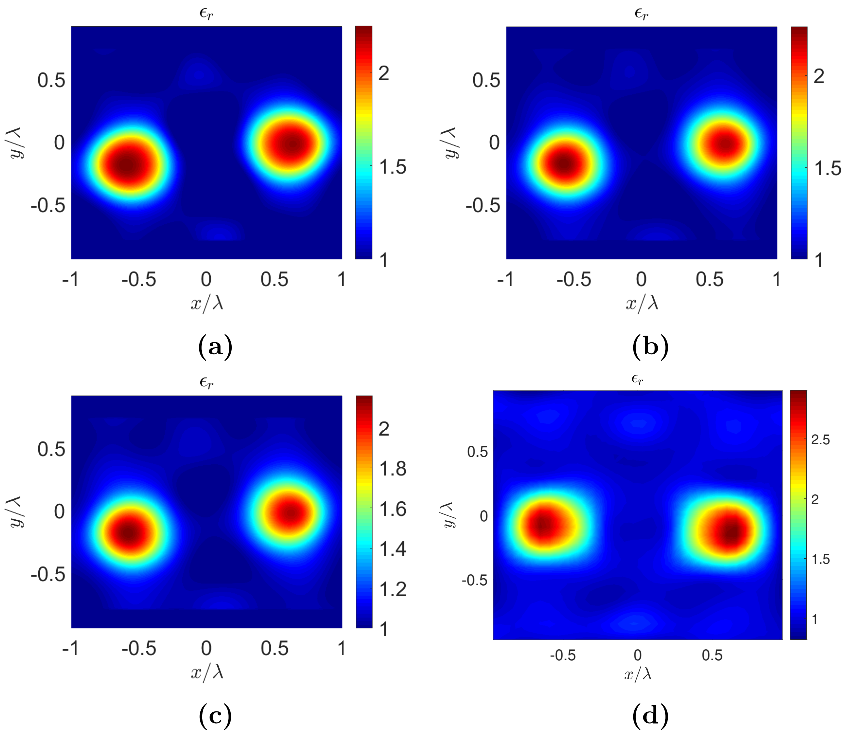

Figure 4.12: *twodiel* dielectric target defined in [82]. Permittivity map for (a) CSI, (b) MR-CSI, (c) CC-CSI and (d) P-CSI, with f = 4 GHz.

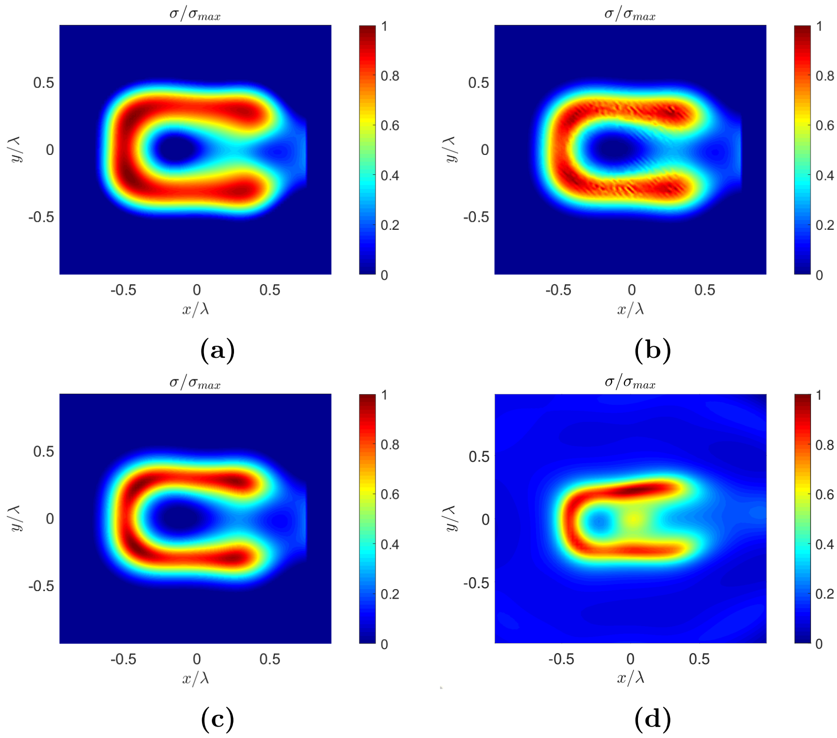

Figure 4.13: *u-shape* metallic target defined in [82]. Normalized conductivity map for (a) CSI, (b) MR-CSI, (c) CC-CSI and (d) P-CSI, with f = 4 GHz.

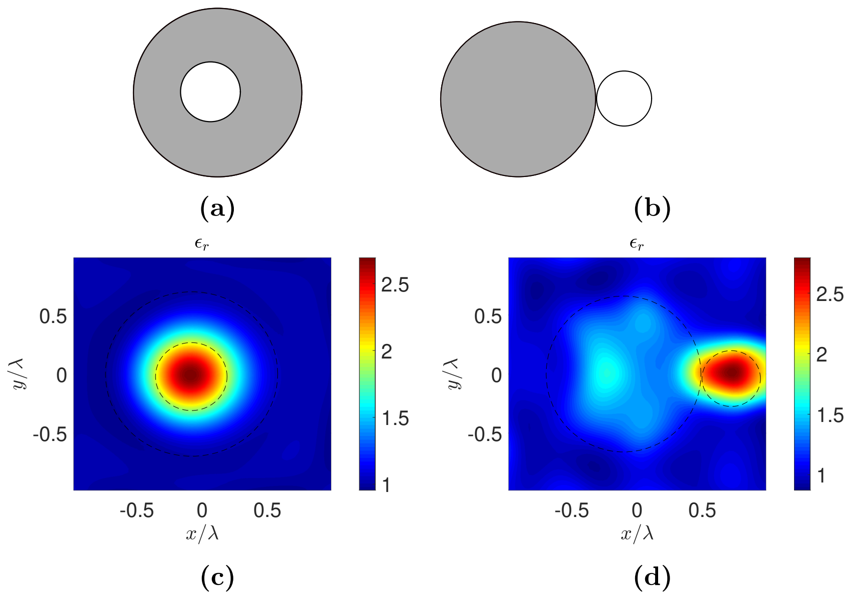

Figure 4.14: Cylindrical (white) plastic and (grey) foam targets: (a) *FoamDielInt* and (b) *FoamDielExt*, taken from [83]. In (c)-(d), retrieved permittivity by applying P-CSI, with f = 4 GHz.

Chapter 5

Phaseless Inverse Scattering Applied to Breast Imaging

5.1 On the Relevance of the Breast Imaging Tools

Among the potential biomedical applications of the microwave imaging methods, such as brain stroke detection [86]–[88], thermal therapy [89], bone imaging [90], cervical diseases [91] and many others, breast cancer diagnosis is still the most investigated. If radar techniques can be implemented as detection tools with limited accuracy in the reconstruction of the inner breast structure, microwave tomography is still considered the most promising solution in identifying the EM breast profile; indeed, recent advances in the development of breast diagnostic systems have led to a series of prototypes that are currently undergoing clinical trials, such as the Wavelia [92] and the MammoWave [93] systems. The electromagnetic analysis of this problem covers different levels of inspections, including antenna selection, operating frequency, number of required independent data and forward/inverse scattering solutions. In this chapter, some of these open challenges are discussed and addressed, as support of the proposed phaseless inverse scattering framework, whereas some reconstruction results will be presented in the final section.

5.2 Coupling Medium Analysis

Indeed, an imaging system design requires, aside from the exploration of inverse scattering solutions, a series of extra in-depth design criteria; one of this deals with the selection of a properly matching medium. Regardless of the imaging application, the main reason for the analysis of the matching medium properties relies on the following:

- Increase the *interrogation energy* coupled from the microwave source into the target, thus limiting the reflections at the target's interface, allowing a successful data inversion [94];

- Introduce a medium with limited losses, contributing in not deteriorating the penetration depth of the impinging wave. At the same time, limited but existent losses contribute to damp unwanted reflections from outer objects, not involved in the imaging process.

- Improve the spatial resolution, even in the case of limited frequency data, due to the wavelength reduction;

- Efficiency in the antenna dimension scaling.

In the case of biomedical imaging, the use of a matching medium has to deal with the need for a clinically disposable and easily realizable medium. Among the literature, glycerine-based solutions are widely considered for low-GHz range imaging applications [95]–[97]. In this case, solutions with a $70\% - 90\%$ glycerine content are conventionally used [98]. Other mixtures include the ones based on Triton X-100 [88] and corn syrup [99]. In all the mentioned cases, mixtures can be tailored differently to match the imaging needs. Other interesting solutions consider the use of *brick* antenna elements, where each radiating element is embedded in a solid box, acting as a coupling medium, such as the one made of urethane rubber and graphite powder implemented in the brain-stroke imaging prototype presented in [100].

5.2.1 Equivalent Transmission Line (TL) Model

In order to preliminary investigate the optimal conditions in terms of operating frequency and electromagnetic properties of the matching medium for the microwave breast imaging case, different approaches can be considered. Multiple reflection theory can be used for the propagation model [101] or, alternatively, a Transmission Line (TL) model, simulating a multi-layered structure with different sizes, can be used as a simplified 1D layered case. Indeed, TL models are generally used as an auxiliary tool, in both antenna design and modeling but also in the analysis of propagation in multi-layered structures. Here, the TL model aims to identify the optimal matching medium properties and frequency, to minimize the reflections at the target's interface. For the case at hand, the model consists of a 3-layered TL model, composed of an outer thin skin layer and two inner layers, denoting the fat portion and the fibroglandular region, respectively, as depicted in Fig. 5.1. The corresponding TL lengths have been set ac-

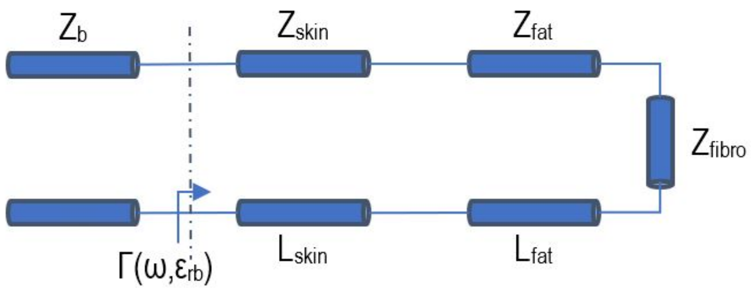

Figure 5.1: 3-layered Transmission Line (TL) model, including the involved breast tissues and the background medium.

cording to the typical transverse thickness and set to $L_{skin} = 1.5$ mm and $L_{fat} = 30$ mm, whereas the fibroglandular region is assumed as equivalent load. The line impedance value for each of the i^{th} tissue has been set as:

$$Z_i = \sqrt{\frac{\epsilon_0 \hat{\epsilon}_{r_i}}{\mu_0 \mu_{r_i}}} \tag{5.1}$$

The EM properties of those layers are obtained starting from the ones related to the fat percentage of different breast tissue types, as provided in [102], [103]. More specifically, three breast tissue categories, indicated as Groups 1-3 and classified in terms of fat content, are considered [104]:

- Group 1 (fat content: 0-30%) - skin model;

- Group 2 (fat content: 31-84%) - fibroglandular model;

- Group 3 (fat content: 85-100%) - fat model.

The median profile among the breast models included within each group has been evaluated. Therefore, starting from the first-order Cole-Cole model:

$$\begin{aligned} \hat{\epsilon}_r(\omega) &= \epsilon_\infty + \frac{\epsilon_s - \epsilon_\infty}{1 + (j\omega\tau)^{1-\alpha}} + \frac{\sigma_s}{j\omega\epsilon_0} \\ &= \epsilon_\infty + \frac{\Delta\epsilon}{1 + (j\omega\tau)^{1-\alpha}} + \frac{\sigma_s}{j\omega\epsilon_0} \end{aligned} \tag{5.2}$$

And according to the equivalent Cole-Cole parameters summarized in Table 5.1, the median EM properties for Groups 1-3 are evaluated, as shown in Fig. 5.2.

Table 5.1: Cole-Cole (C-C) parameters for the breast Groups 1-3 - median profile [102]–[104].

C-C Param.	Group 1	Group 2	Group 3
ϵ_∞	7.82	5.57	3.14
$\Delta\epsilon$	41.48	34.57	1.71
τ [ps]	11.66	9.15	14.65
α	0.047	0.095	0.061
σ_s	0.713	0.524	0.036

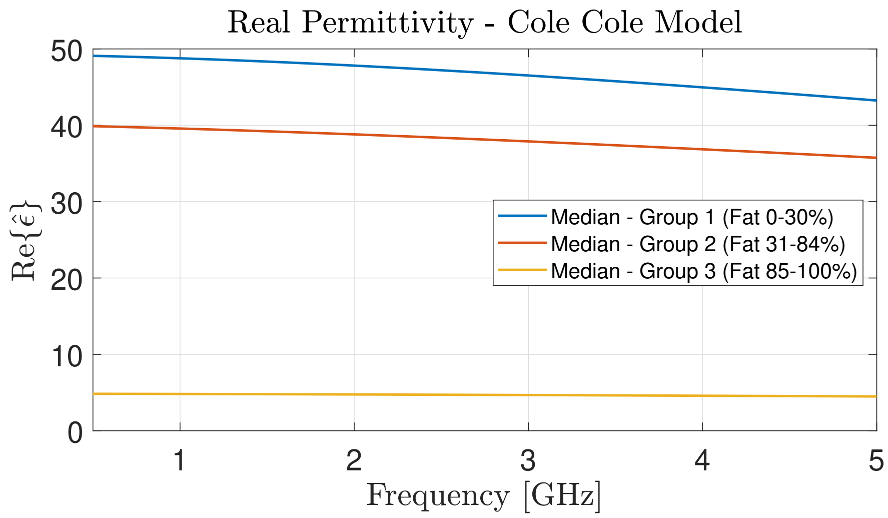

(a)

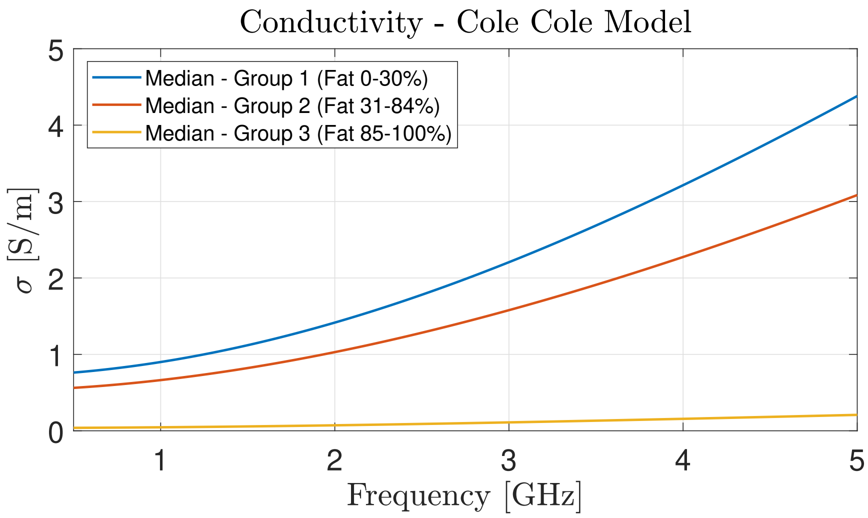

(b)

Figure 5.2: Cole-Cole model for the three different breast groups - (a) real permittivity and (b) conductivity.

The reflection coefficient $\Gamma(\omega, \epsilon_{r_b})$ is calculated at the load interface as function of the operating frequency and of the background relative permittivity. According to the permittivity-frequency map shown in Fig. 5.3, a confined region with a better matching can be identified. The dispersive model, evaluated for frequencies up to 5 GHz, reveals that minimum reflections can be obtained when $\epsilon_{r_b} \approx 20$, with an operating frequency in the range of 2 GHz.

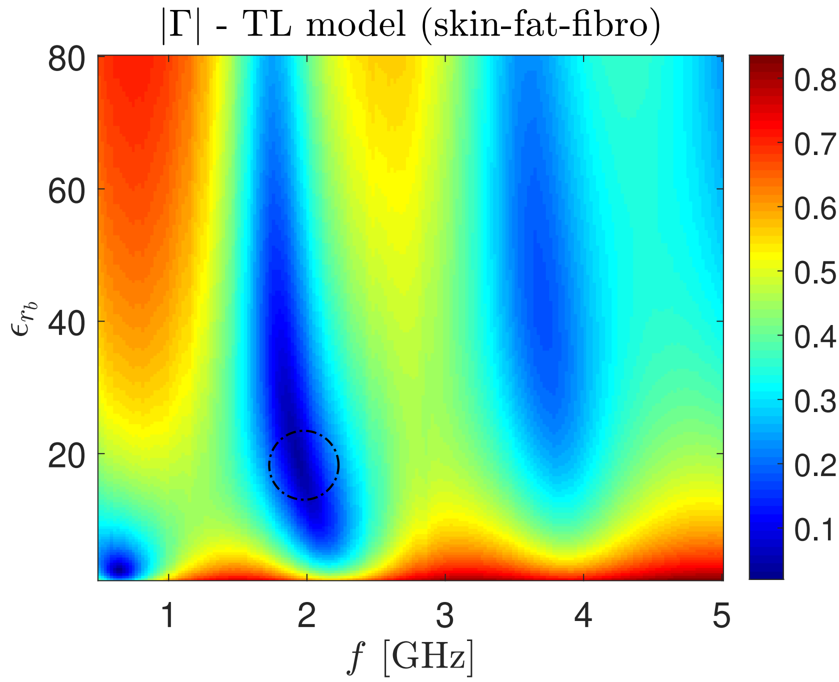

Figure 5.3: Reflection coefficient $\Gamma(\omega, \epsilon_{r_b})$ for the TL model depicted in Fig. 5.1.

5.2.2 Validation of the TL model - 3D breast models

The conclusions coming from the TL model, suggest to investigate more into the predictability of the method, by considering a more realistic scenario. This includes, firstly, the use of an Antipodal Vivaldi Antenna (AVA) as field source. Extensively used in the microwave imaging community for imaging applications [105], the AVA has been considered for the assessment of the TL model due to the need for a radiating element with a desirable low cross-polarization, specifically in the near-field zone. The low cross-polarization feature guarantees the assumption of a confined E-field component along the longitudinal axis of the designed antenna, ideally approaching the case of a line source. Since the Single-Layer Antipodal Vivaldi Antenna (SL-AVA) suffers from poor cross-polarization features [106], this can be consistently improved by considering the double-layered counterpart, namely the Double-Layer Antipodal Vivaldi Antenna (DL-AVA) [107], [108]. The designed antenna is shown in Fig. 5.4.

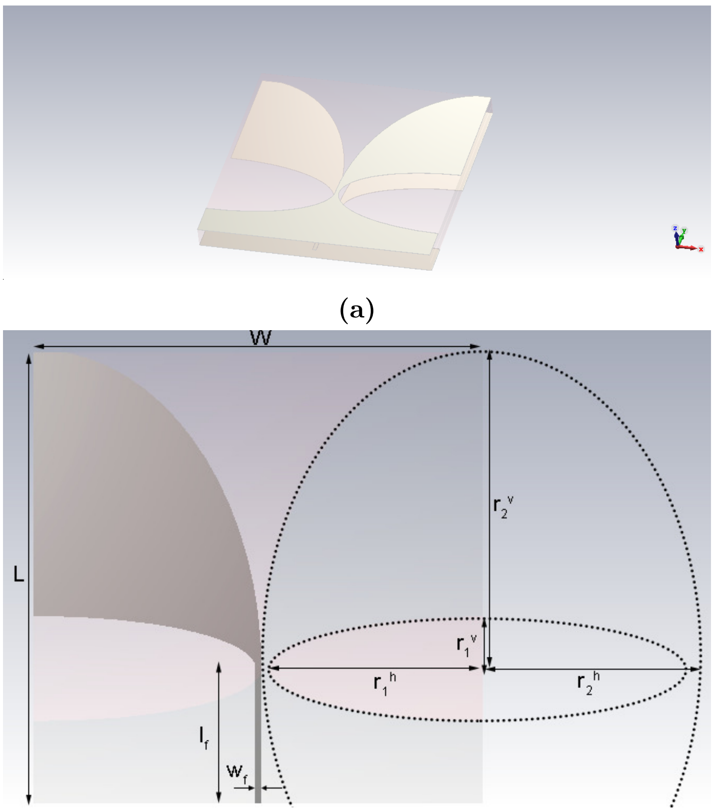

(b)

Figure 5.4: Double-Layer Antipodal Vivaldi Antenna (DL-AVA) - (a) angle view and (b) geometry details - the inner layer is highlighted.

Following the design proposed in [109]–[112], an RT/Duroid 6010LM (h = 1.905 mm, ϵ_r = 10.2, tanδ = 0.0023 @ 10 GHz) is selected as substrate, while the ellipses' geometries and sizes have been optimized through CST Studio Suite®. According to the previous analysis, a 2 GHz operating frequency and a relative permittivity of the surrounding medium $\epsilon_{r_b} \approx 18$ have been selected, while the design specifications are summarized in Table 5.2.

Table 5.2: Double-Layer Antipodal Vivaldi Antenna (DL-AVA) - design specifications.

Parameter	Size [mm]
W	48
L	48
w_f	0.72
l_f	14.33
r_1^v	5.59
r_1^h	23.28
r_2^v	34
r_2^h	24

The polarization behavior of such designed antenna has been tested in the absence of the target. As depicted in Fig. 5.5, the field evaluated in the NF - denoted as E^{inc} and accounting for all the E-field components is compared to the longitudinal component, supposed to be used in the TMz case, namely E_x^{inc} according to the used reference system. The good cross-polarization properties have been evaluated in a broadband fashion in the case of a fixed location probe (Fig. 5.5a), as well as for a near field distribution along a certain direction along the z-axis (Fig. 5.5b). For those results, the field probe and the antenna positions are assumed to be located R_{rx} = 80 mm away from the origin of the central global coordinates. The designed antenna is then tested into a realistic scenario. The latter consists of a matching medium box, where the AVA antenna is immersed, with the presence of a realistic breast model. The electromagnetic properties of the assumed breast are imported on a voxel basis, according to those of the MRI-derived models proposed in [66], [113]. Specifically, in order to consider different breast densities, two phantoms have been analyzed: a heterogeneously dense breast model and a more dense model, depicted in a Fig. 5.6a and Fig. 5.6b, respectively.

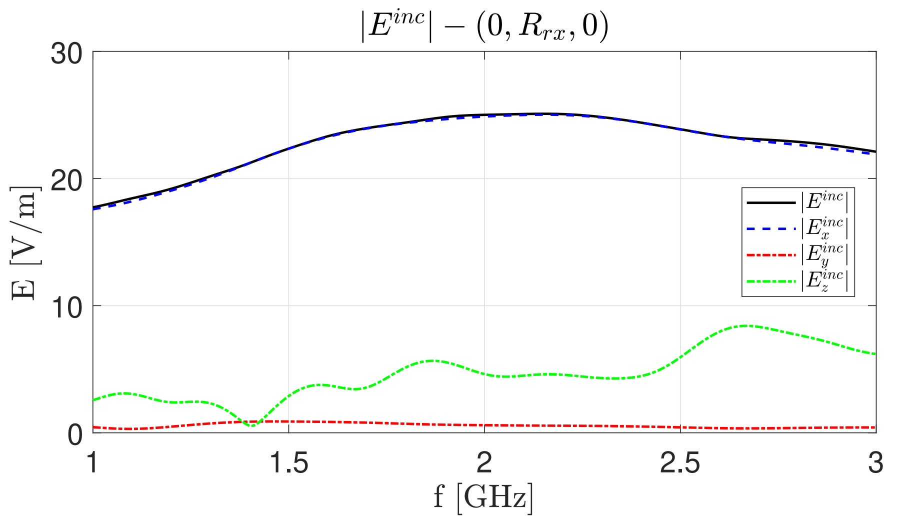

(a)

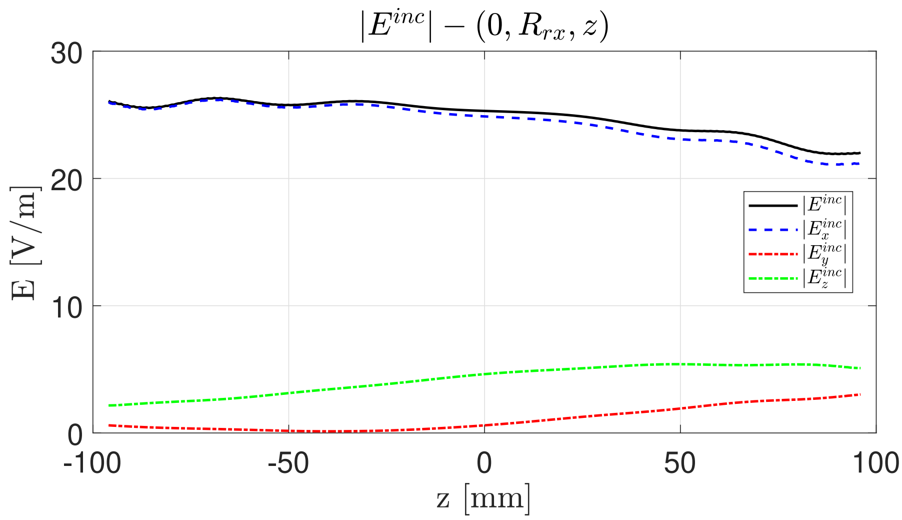

(b)

Figure 5.5: Incident E-field components as function of (a) frequency and (b) spatial distribution, with the antenna located at $(0, R_{rx}, 0)$.

The two models are classified as Class 2 and Class 3 breast respectively, according to the Breast Imaging Reporting & Data System (BI-RADS) by the American College Radiology (ACR) [114], [115]. Each phantom is constituted of a 3-D voxel grid, with $\Delta V = 0.5$ mm^3 as voxel size.

Similarly to the analysis performed for the incident field, the polarization features of the antenna are evaluated in the presence of the breast models. An example of the total field distribution in the presence of the Class 3 breast model depicted in Fig. 5.6b, is shown in Fig. 5.7a and Fig. 5.7b. For those cases, the probes are located at $(0, 0, -R_{rx})$ and on the $(0, y, -R_{rx})$ line, respectively.

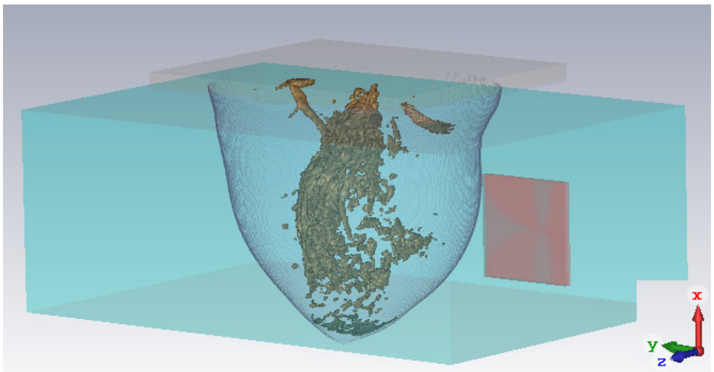

(a)

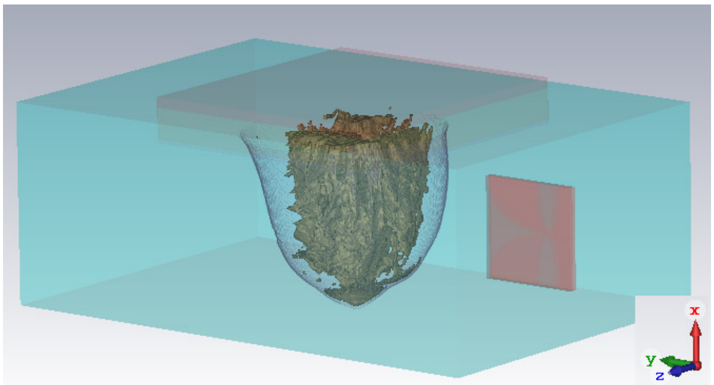

(b)

Figure 5.6: Double-Layer Antipodal Vivaldi Antenna (DL-AVA) with the presence of (a) Class 3 and (b) Class 2 breast model. The fibroglandular tissue is highlighted.

A parametric analysis is performed by considering the background permittivity variation $\epsilon_{r_b} \in \{1, 30\}$. The reflection coefficients with the presence of the two breast models as a function of ϵ_{r_b} are shown in Fig. 5.8. Those results indicate that the use of different breast models does not strongly impact on the antenna response, confirming the validity of the results for different breast densities.

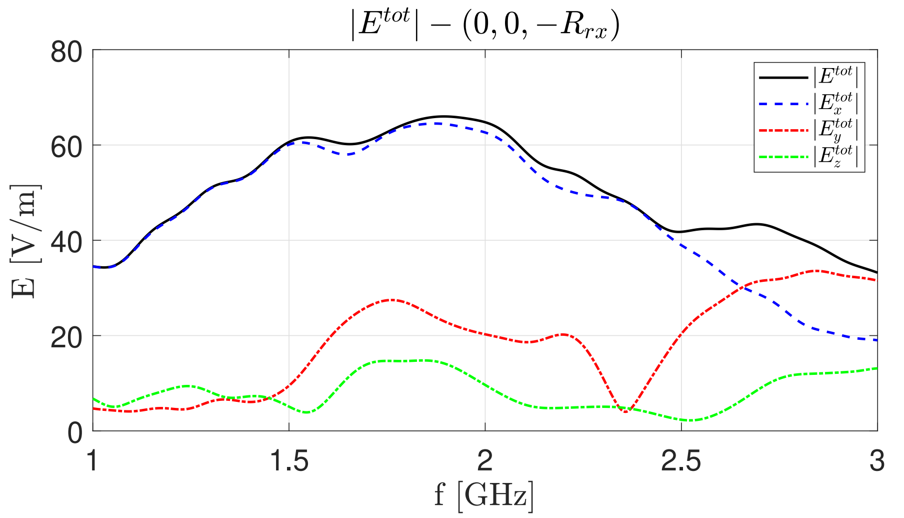

(a)

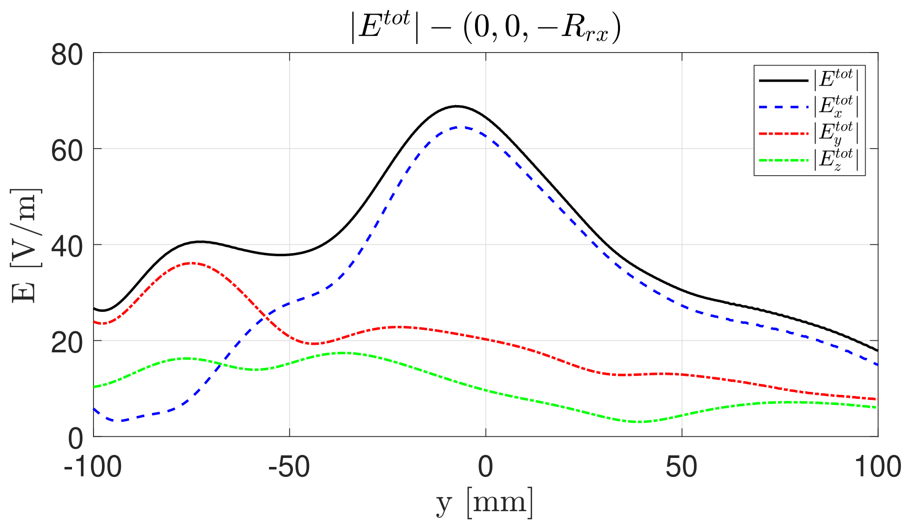

(b)

Figure 5.7: Total E-field components as function of (a) frequency and (b) spatial distribution with the antenna located at $(0, -R_{rx}, 0)$.

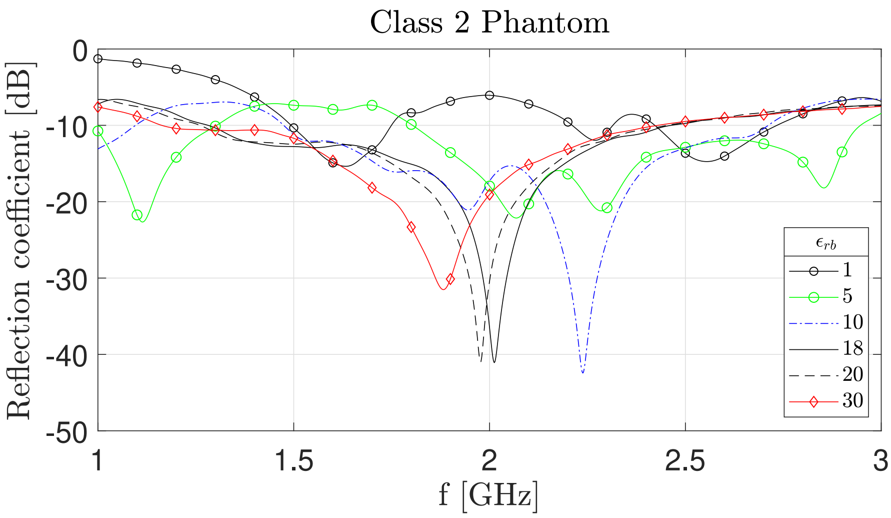

(a)

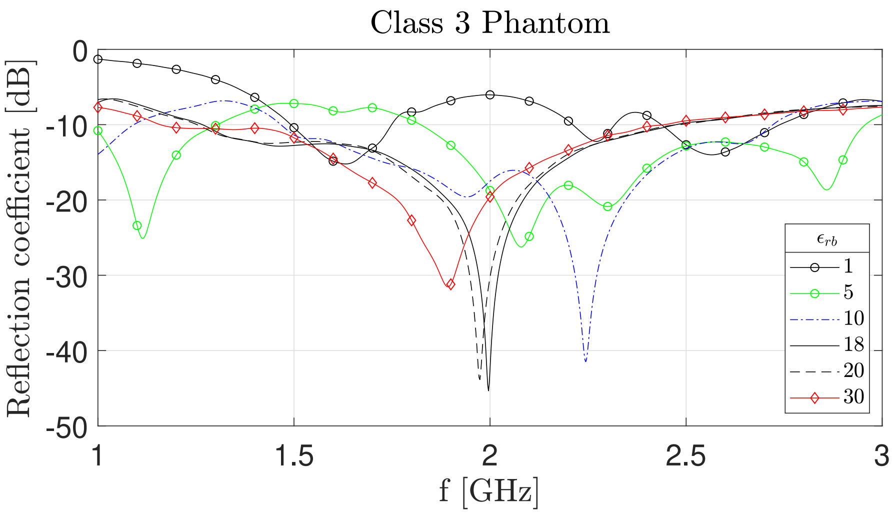

(b)

Figure 5.8: Reflection coefficient for different ϵ_{r_b} values - (a) Class 2 and (b) Class 3 phantom.

The antenna radiation efficiency has been calculated for different permittivity values of the matching medium ϵ_{r_b}, with the presence of the Class 3 breast model and it is shown in Fig. 5.9, indicating consistency with the results predicted with the TL model. Consequently, most of the breast imaging reconstruction results presented throughout the thesis consider a permittivity profile of the background - ϵ_{r_b} - and an operating frequency in accordance to what is illustrated in this section.

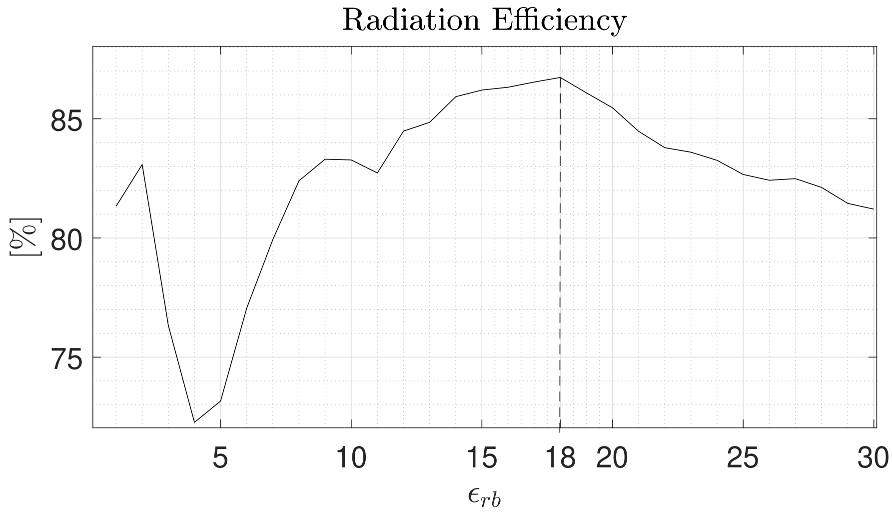

Figure 5.9: Radiation efficiency vs. ϵ_{r_b}, for the Double-Layer Antipodal Vivaldi Antenna (DL-AVA), in the presence of a Class 3 breast model, evaluated at f=2 GHz.

5.3 Breast Targets - Simplified COMSOL Model

The inverse imaging problem was first tested by considering simulation-based solutions of the involved fields. Those data are generated by considering simplified 2D breast models. The acquisition scenario has been set in COMSOL Multiphysics® and shown in Fig. 5.10. A Debye model is implemented for the EM properties of the involved tissues within the breast phantom and it is shown in Fig. 5.11 for each tissue, whereas the dielectric properties evaluated at 2 GHz are summarized in Table 5.3.

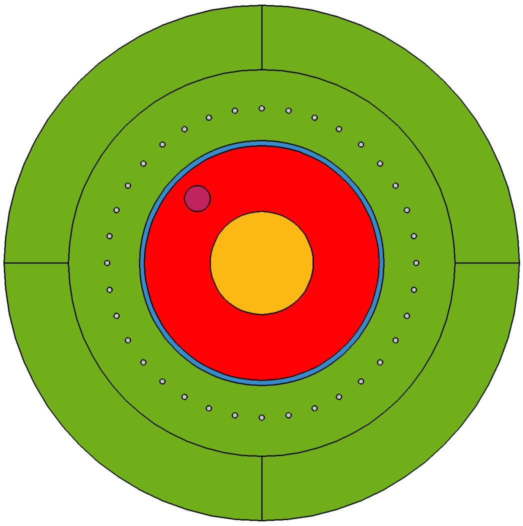

Figure 5.10: Simulated geometry in COMSOL - coupling medium (green), skin (blue), fat (red), fibroglandular (yellow), and a tumor simulant (purple) on the upper side-left of the model. Incident field simulated as line current out-of-plane.

Table 5.3: Dielectric properties involved in the COMSOL model in Fig. 5.10, with $\epsilon_{r_b} = 18$.

Material	ϵ_r	σ
Skin	39.25	1.24
Fat	4.95	0.08
Fibroglandular	36	0.86
Tumor	45.83	1.37

The setup consists of a multi-view simulated system, with a certain number of transceivers N_{TX}. A multi-static scenario resembles to be the most informative way of collecting measured total field data in cylindrical configurations. Indeed, the spatial sampling has a strong impact in the case of limited available data, whereas it becomes crucial when considering more sparse data such as the phaseless case. TMz line currents are used as EM sources, with an induced current I = 1 mA, while a Perfectly Matched Layer (PML) surrounding the imaging area truncates the computational region. The retrieved dielectric contrast χ after performing the inversion is indicated in Fig. 5.12. The tumor simulant located within the fat tissue is correctly localized, while some reconstruction errors can be noticed in the inner part of the target, due to the non-null conductivity values of the involved materials. In this reconstruction results, instead of considering the *a-priori* knowledge of the incident field distribution, a field

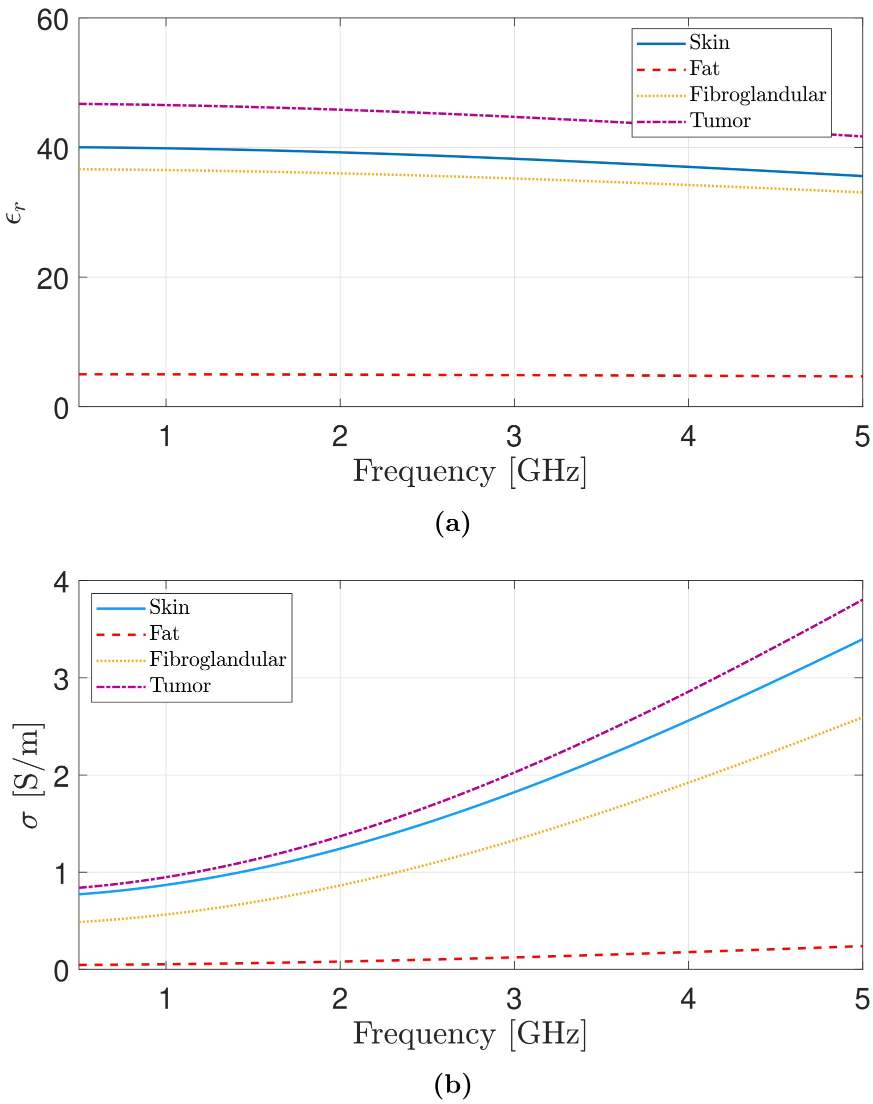

Figure 5.11: Debye model for the involved simulated tissues - (a) permittivity, (b) conductivity.

estimation based on the ME previously discussed in Section 3.3 has been tested, where the truncation of the modal expansion has been specifically tailored for the case at hand, by inspecting the contribution of the different Hankel functions. Here the impact of selecting the right coupling medium dielectric properties is highlighted. Indeed, this aspect can be appreciated when considering the objective function trend to be minimized - according to the iterative reconstruction scheme based on the solver described in Section 4.1, evaluated for different permittivity values of the background medium surrounding the target as function of the number of iterations, as depicted in Fig. 5.13.

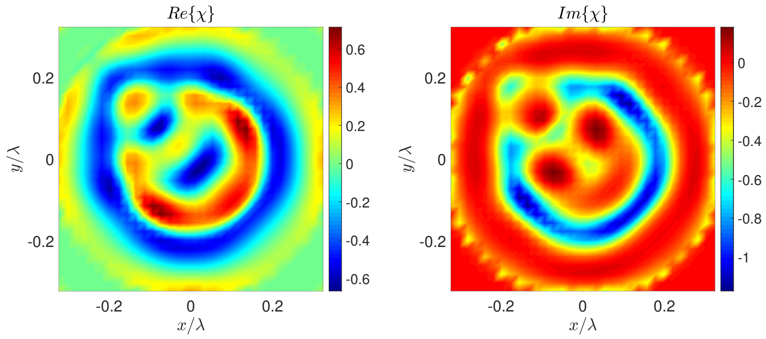

Figure 5.12: Retrieved dielectric contrast χ of the model depicted in Fig. 5.10 - (a) real and (b) imaginary part.

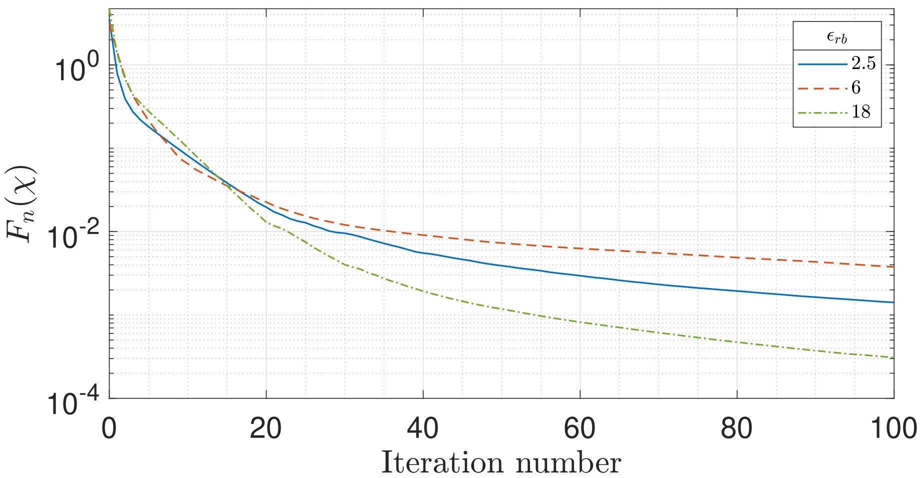

Figure 5.13: Cost function trend for the inverse method proposed in Section 4.1 for different background permittivity values - ϵ_{r_b}, in the case of a simplified breast target as the one shown in Fig. 5.10.

The robustness of the reconstruction method is tested by considering an Additive White Gaussian Noise (AWGN) applied to the involved fields. The algorithm has been evaluated by assuming SNR values that can be comparable to experimental related data; the imaging results for SNR $\in \{20, 30, 40\}$ dB are shown in Fig. 5.14. Noisy data turns out to reduce the effectiveness of the strategy, especially in the edge-detection phase as well as in terms of quantitative reconstruction, even though the overall shape, geometry and localization of the confined high-permittivity region are visible for all the investigated cases.

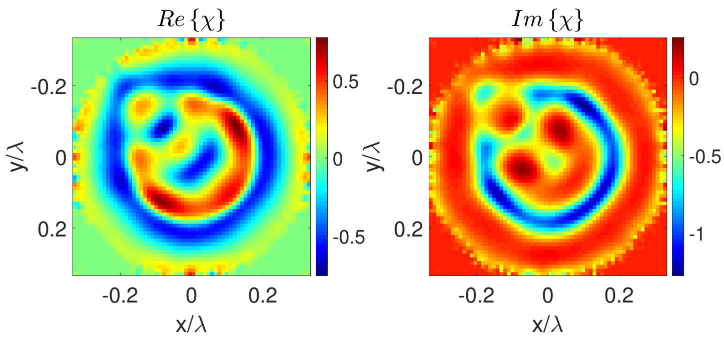

(a)

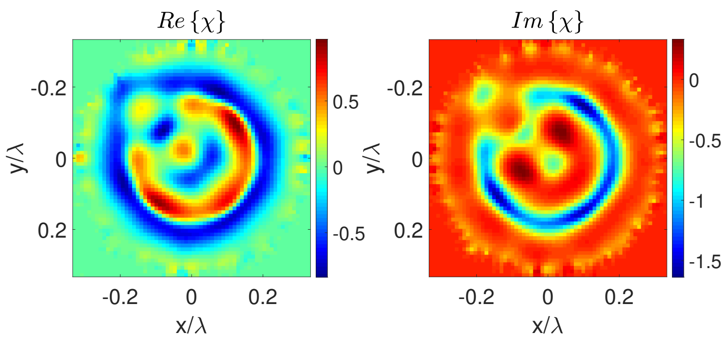

(b)

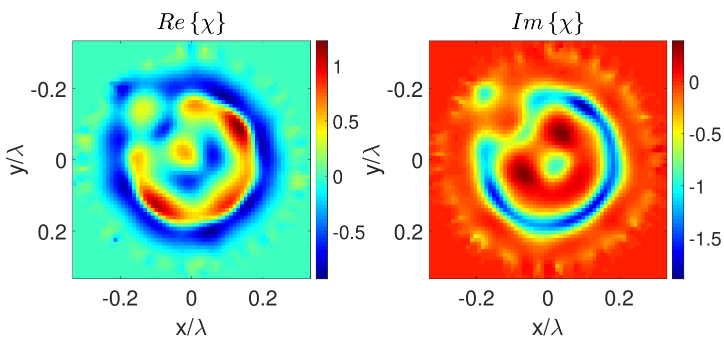

(c)

Figure 5.14: Dielectric contrast - χ - for different SNR values: (a) 40 dB, (b) 30 dB and (c) 20 dB.

5.4 Breast Targets - Realistic Models and Incident Field Prior

A first imaging reconstruction campaign has been performed by using the reconstruction method provided in Section 4.1, with the incident field distribution assumed to be known. In order to test the versatility of the phaseless reconstruction method, a series of breast models with different breast densities have been assumed as targets. Those consists of a series of MRI-based models provided by the University of Wisconsin Cross-Disciplinary Electromagnetics Laboratory (UWCEM) [66]. Within each phantom, a tumor simulant with size $d = 10$ mm has been included, resembling a bloody region with high permittivity, according to the corresponding Debye model. The EM properties of the remaining tissues have been replaced with the ones obtained according to the dielectric characterization of a series of tissue-mimicking phantoms. More specifically, instead of considering mixtures based on specific liquids such as glycerine [98] and Triton-X 100 [116]–[118], the realized mixtures consider the use of cheap ingredients [119]–[122], easily available from groceries. More details are provided in Appendix 5.6.

Again, the multi-static scenario considers 32 transceivers, equally spaced and surrounding the breast model, whereas the permittivity of the background is assumed according to the analysis performed in Section 5.2. For the generation of the scattered data, a two-dimensional non-magnetic case with a transverse magnetic (TM) polarization is considered. A proprietary forward solver is implemented by considering a Conjugate Gradient Fast Fourier Transform (CG-FFT)-based MoM model [68], [123]. A finer grid consisting of $N_x \times N_y$ cells is adopted as compared to the inverse scattering solution, so that a potential inverse crime can be avoided. The single square cell area is approximated to the equivalent circular area and the dielectric properties are assumed to be uniform within the single cell. The analytical details for the CG-FFT are provided in Appendix 5.6. The generated scattered field data is then corrupted with an Additive White Gaussian Noise (AWGN) resembling an SNR equal to 20 dB. The reconstruction results for the different breast models are reported in Figs. 5.15 to 5.17; due to the poor results in terms of retrieved conductivity, the error metrics are reported in Table 5.4 for the retrieved real permittivity only.

Table 5.4: Qualitative metrics for the analyzed breast phantom slices, considering the P-CSI approach, with the incident field assumed to be known.

Phantom ID	$RMSE_{\epsilon_r}$	ρ_{ϵ_r}
010204	7.047	0.921
012204	7.572	0.906
062204	9.198	0.909

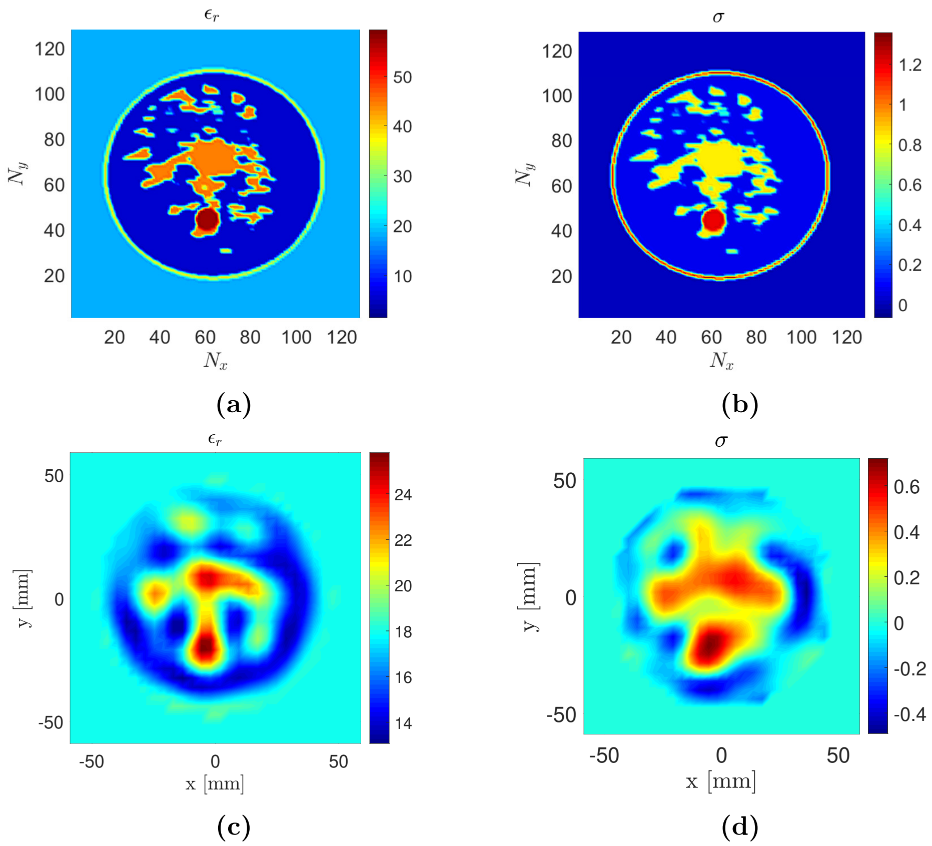

Figure 5.15: (a)-(b) Ground truth - (c) permittivity and (d) conductivity reconstruction results for the Class 2 Breast Model - ID 010204.

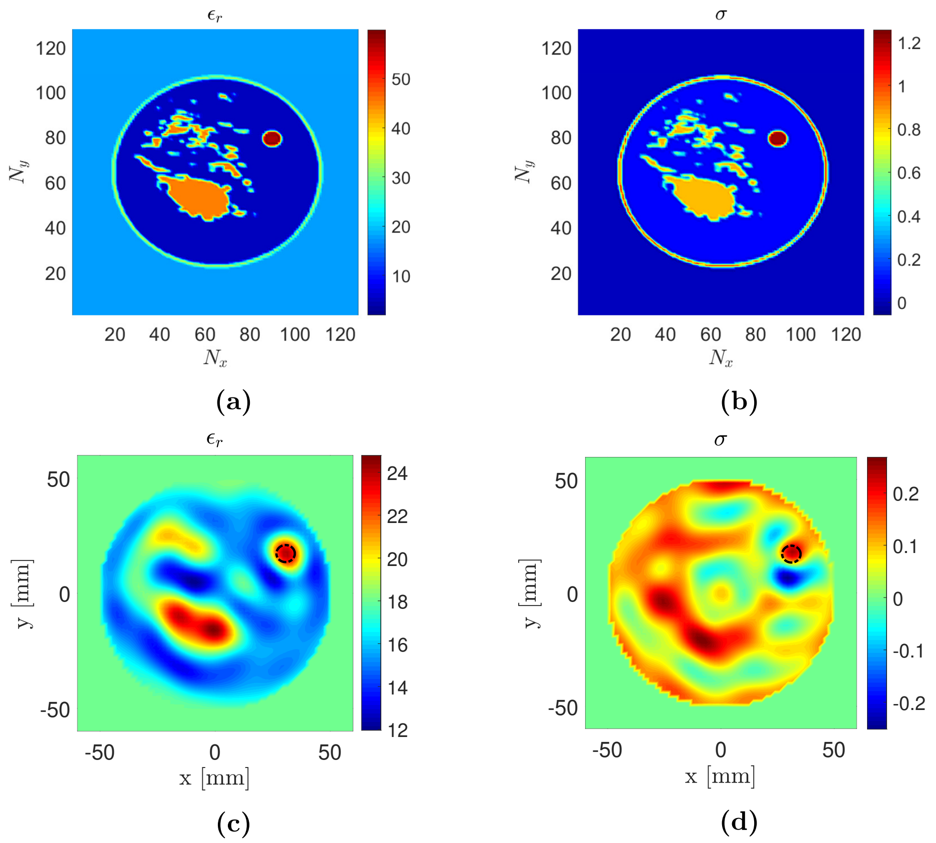

Figure 5.16: (a)-(b) Ground truth -(c) permittivity and (d) conductivity reconstruction results for the Class 2 Breast Model - ID 012204.

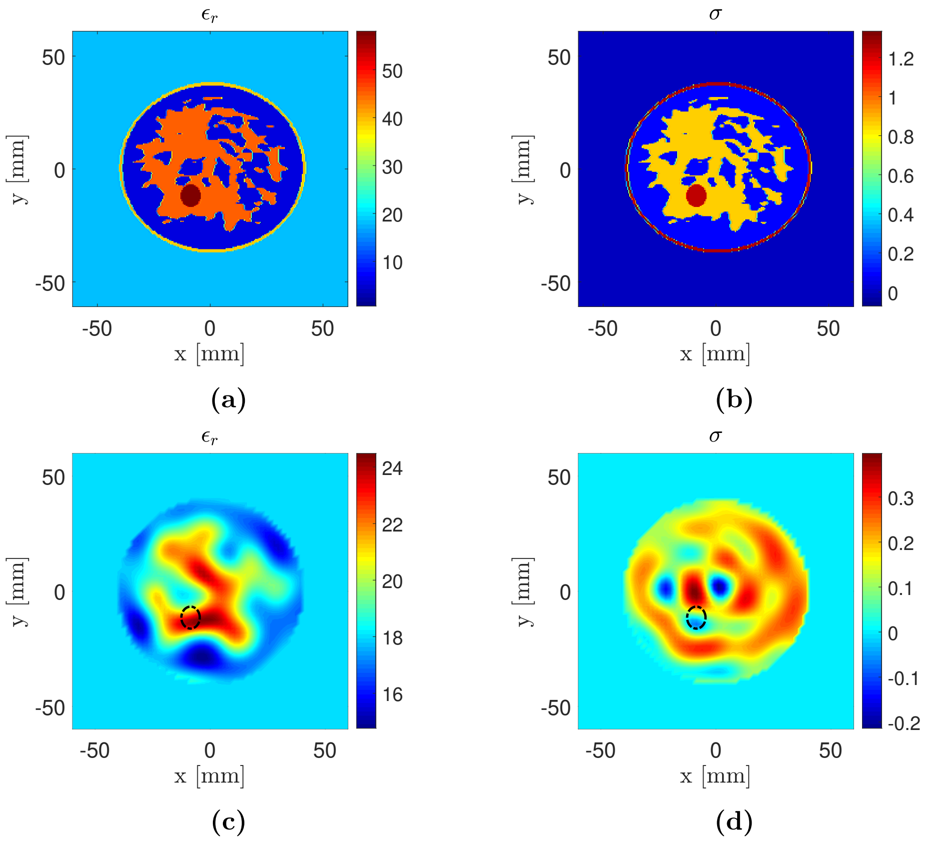

Figure 5.17: (a)-(b) Ground truth - (c) permittivity and (d) conductivity reconstruction results for the Class 3 Breast Model - ID 062204.

5.5 Breast Targets - Realistic Models and Incident Field Recovered from Phaseless Data

In this section, the combined source inverse methods discussed in Chapter 3 are recalled. For the tested breast models, TMz line-current sources are considered. The incident field reconstruction with the combined SDIHT+ SRM method, has been evaluated and compared with the result obtainable with the combined SDIHT+ME technique, as depicted in Fig. 5.18. According to the RMSE values summarized in Table 5.5, the two methods are almost equivalent for the case of non-directive sources. Consequently, the combination of one of them with the PR stage performed through the SDIHT method, allows retrieving the incident field distribution with limited discrepancy as compared to the exact model in Fig. 5.18a.

Table 5.5: Root Mean Square Error (RMSE) in the case of Spatial Domain Indirect Holography Technique (SDIHT) combined with Modal Expansion (ME) or Source Reconstruction Method (SRM).

Reconstruction Method	RMSE Re$\{E_D^i\}$	RMSE Im$\{E_D^i\}$
SDIHT+ME	0.0036	0.0028
SDIHT+SRM	0.0540	0.0461

The simulated acquisition setup is the same as discussed in the previous section, considering a series of breast targets coming from the same repository. The conductivity maps are instead obtained by considering a linear regression model as the one provided in [124]:

$$\sigma(\epsilon_r) = 0.0188\epsilon_r - 0.04711 \tag{5.3}$$

The reconstruction results are shown in Figs. 5.19 to 5.23. The values of the reconstruction metrics described in Section 4.3 are evaluated for the different investigated breast phantoms and are summarized in Table 5.6.

The returned values of the metrics show that the P-CSI, combined with the incident field reconstruction strategy from phaseless data, returns good

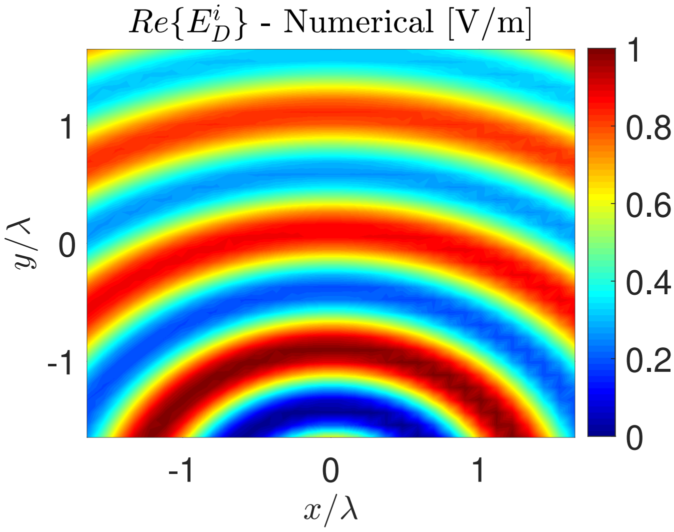

(a)

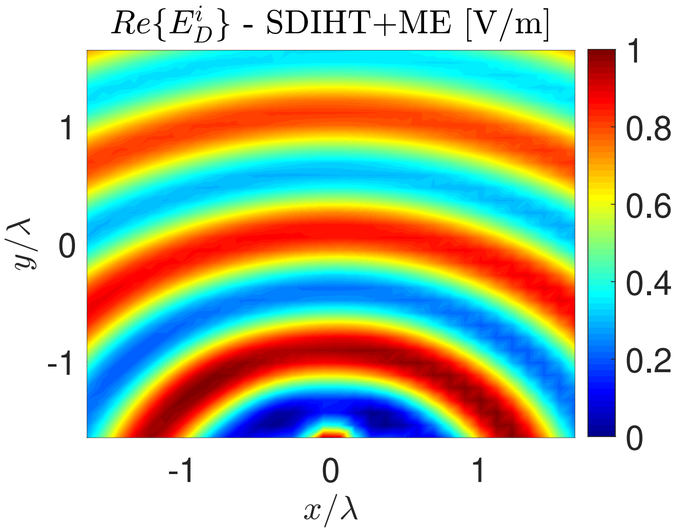

(b)

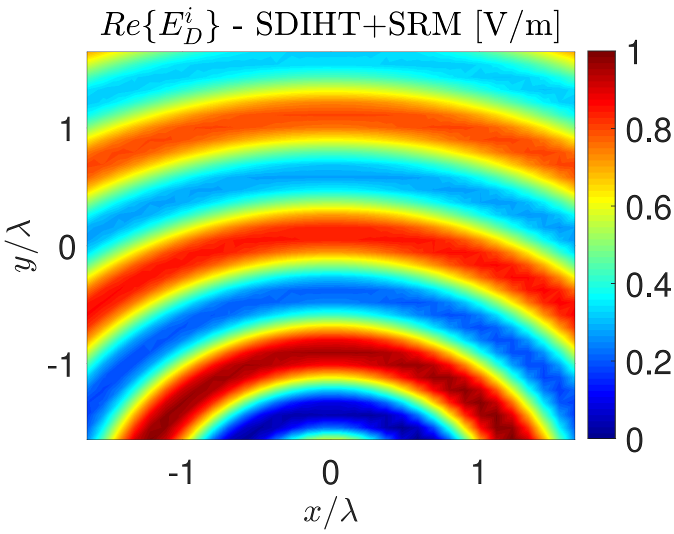

(c)

Figure 5.18: Incident field reconstruction for a TMz line source - (a) Numerical, (b) SDIHT + ME and (c) SDIHT + SRM - real normalized incident field.

Table 5.6: Qualitative metrics for the analyzed breast phantom slices, when P-CSI and the incident field reconstruction approach of Chapter 3 are adopted.

Phantom ID	$RMSE_{\epsilon_r}$	ρ_{ϵ_r}
010204	8.77	0.897
012304	10.82	0.877
012204	8.14	0.904
071904	6.89	0.939

correlation results, with reduced accuracy in terms of RMSE. At this stage, the method is capable of identifying the abrupt permittivity variations, i.e. localizing the region with a high contrast, while the reconstruction is less quantitatively accurate in the case of low-contrast portions, such as the malignant-modeled region within the fibroglandular tissue. This limitation comes from the nature of the CSI based-method itself, while the SDIHT-based reconstruction method for the incident field does not strongly impact the quantitative reconstruction capabilities of the imaging method.

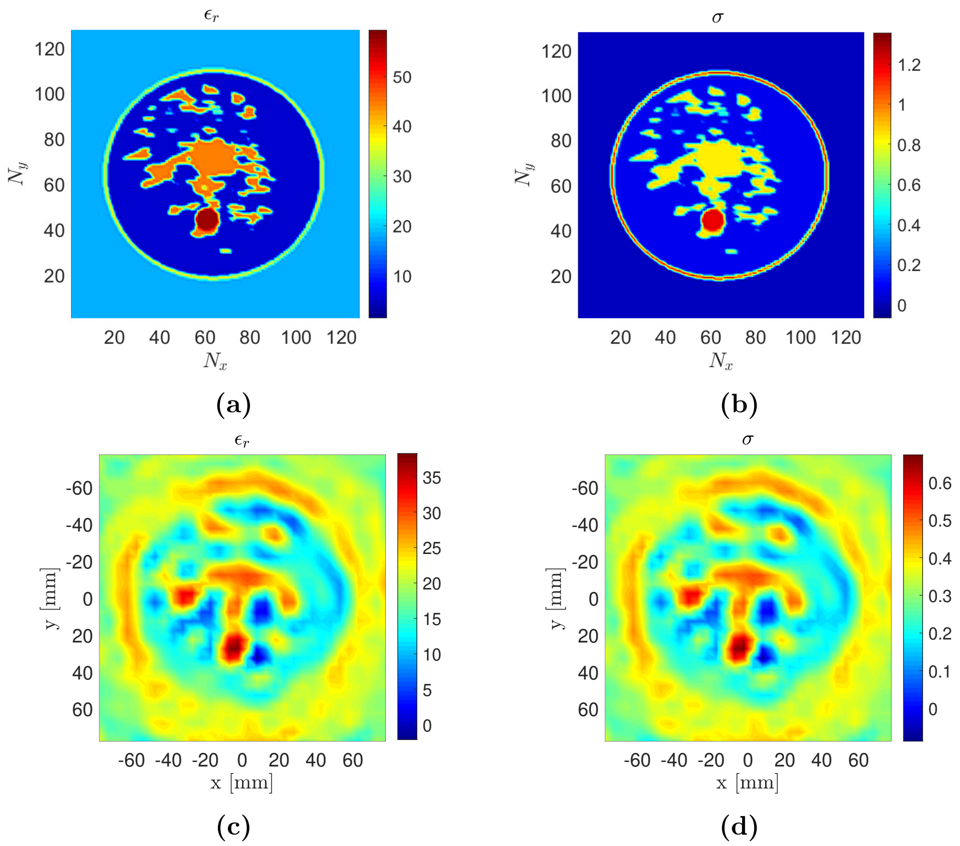

Figure 5.19: Phantom ID: 010204 (a) - (b) ground truth and (c) - (d) reconstruction results.

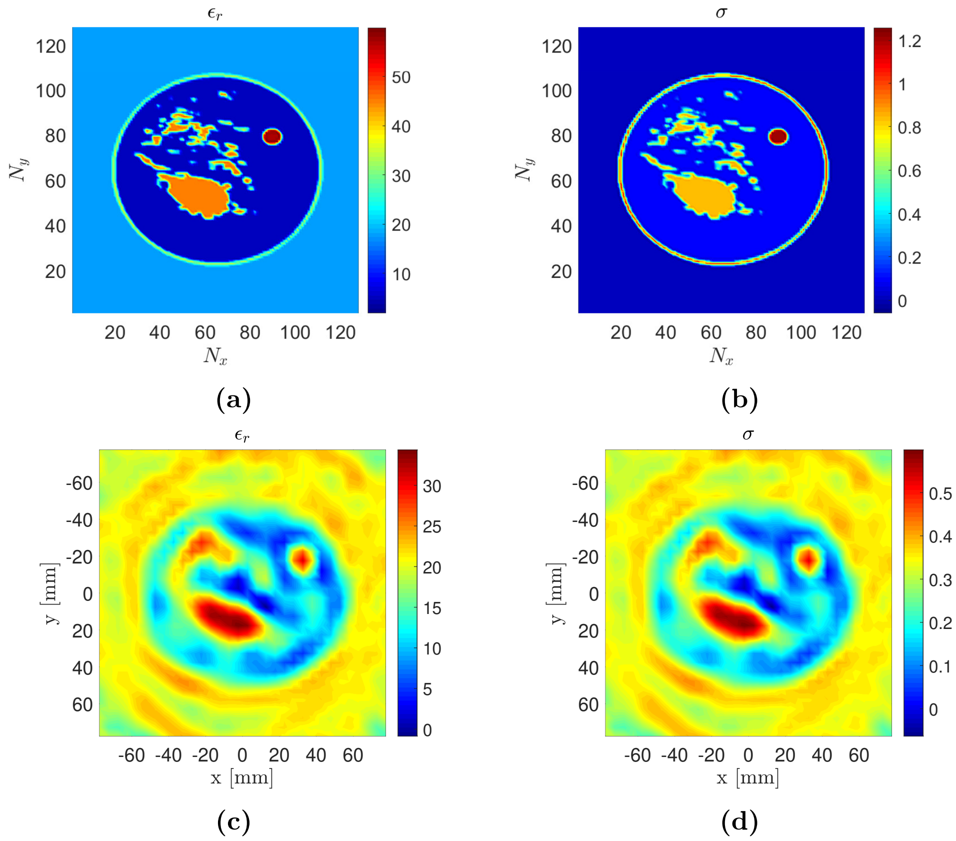

Figure 5.20: Phantom ID: 012204 - (a) - (b) ground truth and (c) - (d) reconstruction results.

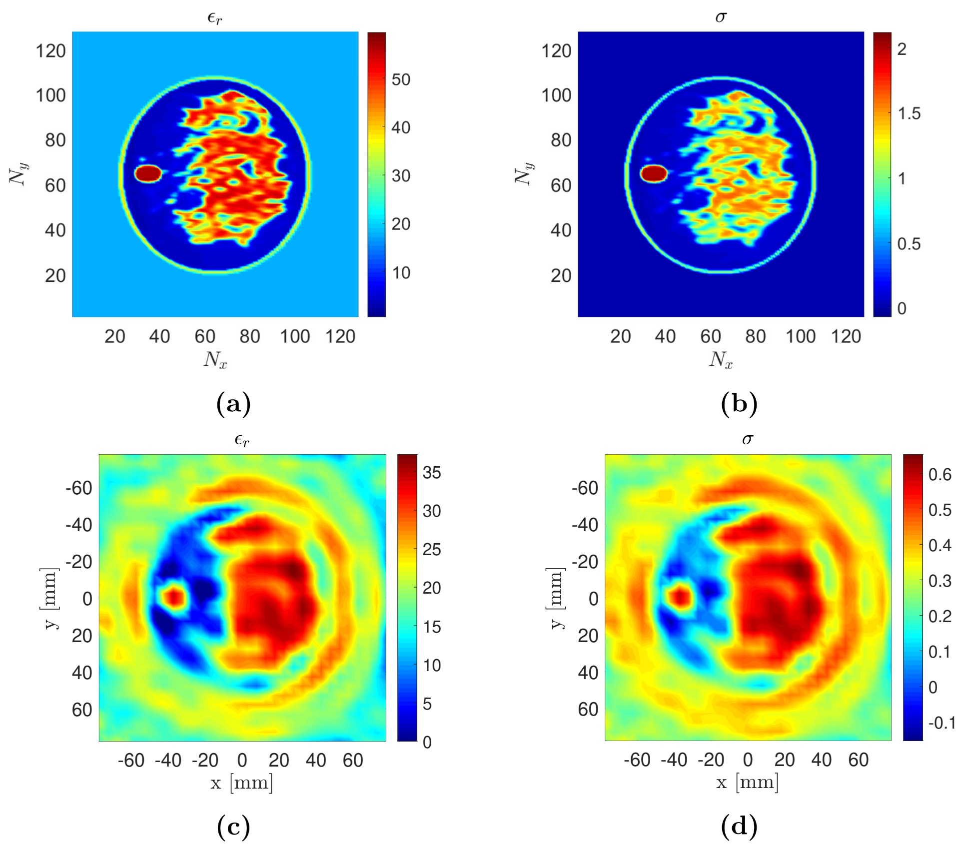

Figure 5.21: Phantom ID: 012304 - (a) - (b) ground truth and (c) - (d) reconstruction results.

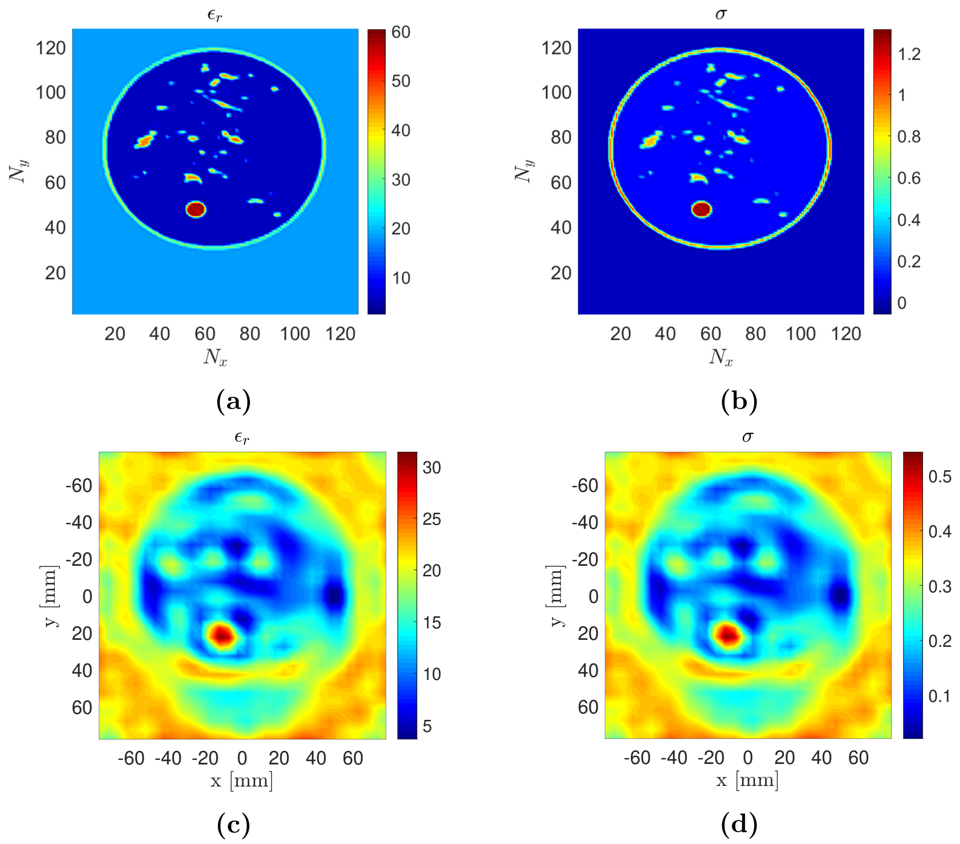

Figure 5.22: Phantom ID: 012804 - (a) - (b) ground truth and (c) - (d) reconstruction results.

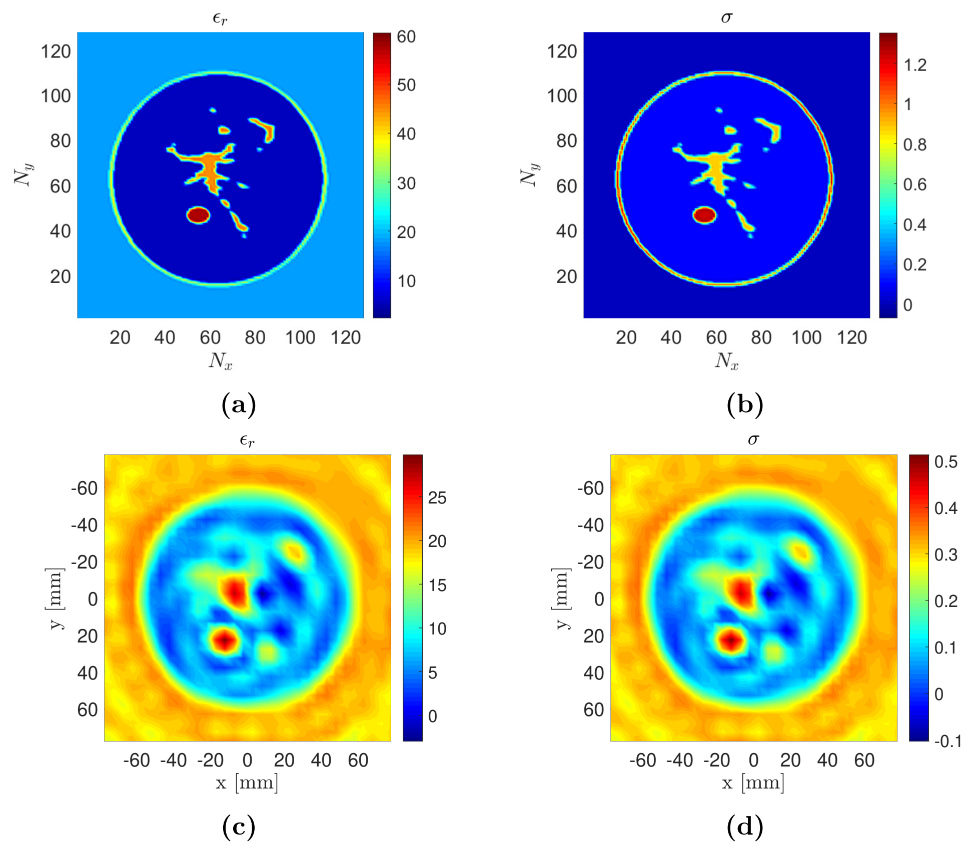

Figure 5.23: Phantom ID: 071904 - (a) - (b) ground truth and (c) - (d) reconstruction results.

5.6 In-silico Validation on a 3D Scenario

The methods investigated throughout the thesis have been ultimately tested in the case of a three-dimensional scenario, resembling the breast imaging case. For this purpose, a simplified cylindrical model has been simulated in FEKO ®, emulating two high dielectric cylindrical inhomogeneities with $\epsilon_r = 54$, included within a homogeneous background, with $\epsilon_{r_b} = 7.5$, approaching the median profile of a Class 2 breast tissue. The 3D configuration is depicted in Fig. 5.24, whereas the geometry details are summarized in Table 5.7.

Table 5.7: Geometry details of Fig. 5.24.

Variable	Value [mm]
$X - Y$ *offset*	15.28
R_{TX}	50
R_{RX}	45
r_{cyl}	10.9
h_{cyl}	43.7

The effectiveness of the inverse strategy while operating in NF zone is tested by replacing the numerical TMz sources with dipoles, whereas the total field is sampled by means of NF probes.

The phaseless approach discussed in Chapter 4 combined with the SDIHT+ SRM incident field recovery strategy has been implemented on the collected data, within the 5-6 GHz frequency range.

Furthermore, the phaseless back-propagation (PBP) initial guess discussed in Section 4.2 has been used for the first operating frequency, whereas a frequency hopping scheme has been adopted for the remaining frequencies. The reconstruction results at the different frequency steps are depicted in Fig. 5.25.

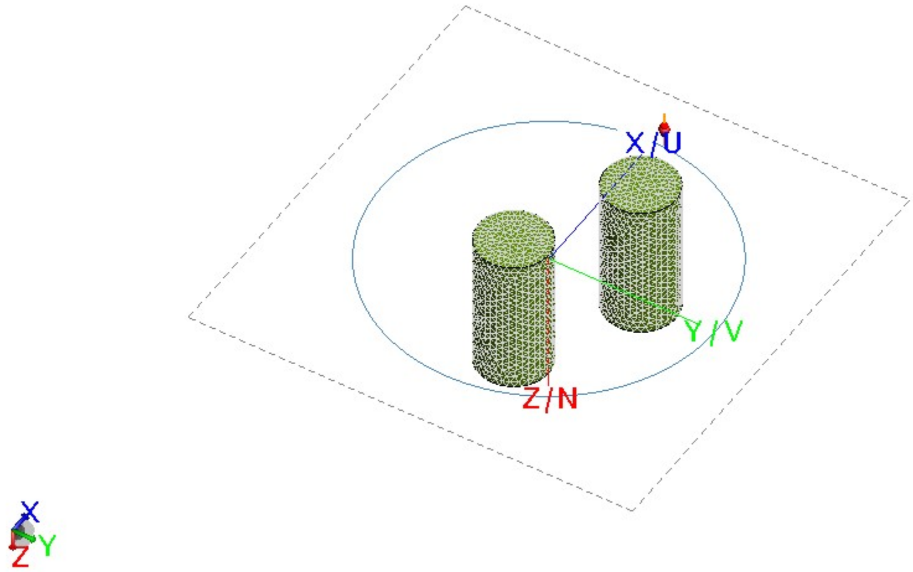

Figure 5.24: Simplified 3D model in FEKO - homogeneous background with the presence of two cylindrical inhomogeneities with high permittivity.

According to the results, the permittivity values are severely underestimated, while the two targets are correctly identified. Consequently, this preliminary investigation denotes how the developed framework can be potentially used not only in the case of experimental far-field data or 2D numerical field data, but also when considering in-silico 3D models, with the presence of strong scatterers within the NF region. The resulting artifacts can be mainly attributed to modeling errors, due to the use of different Green's operators among the forward (3D - MoM) and the inverse scattering solution (2D).

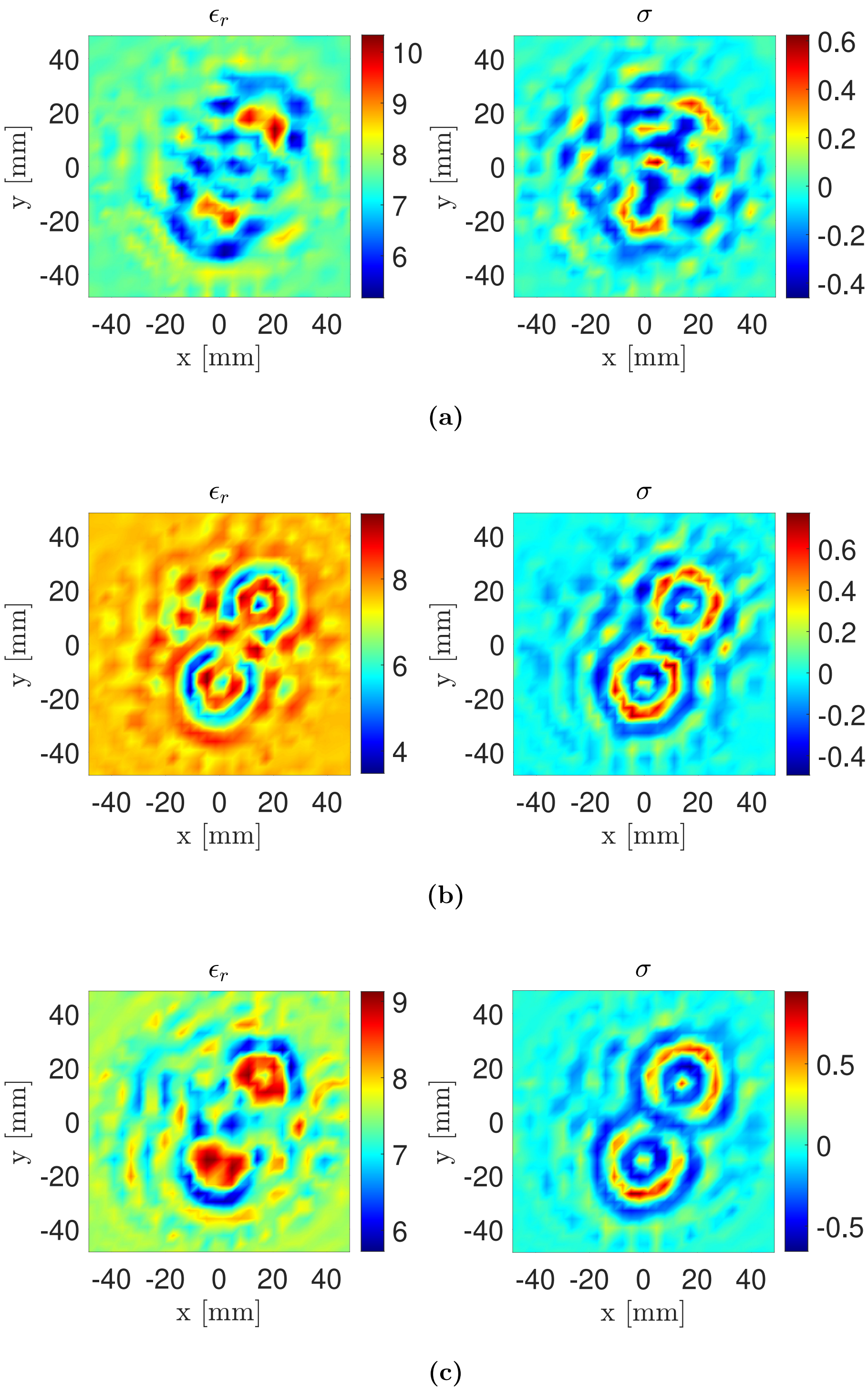

Figure 5.25: Reconstruction results for the 3D FEKO scenario depicted in Fig. 5.24, using a frequency hop scheme - (a) 5 GHz (with PBP initial guess), (b) 5.5 GHz and (c) 6 GHz.

Conclusions

Microwave imaging methods represent an attractive research topic among the applied electromagnetic research community. Several are the reasons behind this strong interest. Firstly, the frequency spectrum within the microwave range includes non-ionizing radiations, which are safe for human exposition, putting them as potential candidates for biomedical imaging applications. Furthermore, the Microwave Imaging (MWI) can be considered a powerful supporting tool to be used in clinics, combined with higher resolution and well-established imaging modalities. Indeed, microwave imaging results can be paired with complementary traits, in the perspective of image fusion techniques, that have already shown encouraging results in the case of PET/CT combined traits. Secondly, aside from the biomedical context, MWI methods find applications in other relevant fields, such as buried object detection, cracks detection, through-the-wall imaging, concealed weapon detection and many others.

The main focus of this thesis was to explore microwave imaging solutions based on amplitude-only data. The motivation behind this choice comes from the possibility to contribute in the reduction of cost and complexity of the existing microwave imaging apparatus, by putting more effort into the inverse scattering problem task.

After a general description of the scattering problems provided in Chapter 1, the imaging task has been introduced in Chapter 2, by discussing the problem statement and by providing a broader review of the current microwave imaging trends, including linear and non-linear inverse scattering strategies and the different phaseless approaches known in literature.

Then, in the context of a phaseless inverse scattering framework, an insight into the incident field modeling relying on phaseless data has been detailed in Chapter 3, where the recovery of the incident field distribution starting from amplitude-only data has been detailed and addressed. More specifically, a solution that combines a space domain holography method and a series of inverse source strategies, expressing the EM field in terms of primary source or equivalent currents has been detailed. The combined strategy has been tested when considering different EM sources, showing promising results in the field of inverse source solutions with phaseless data.

The implementation details of a phaseless inverse scattering problem solution have been discussed in Chapter 4, and some validation examples coming from experimental data and simulated data of different targets have been illustrated. Initial attempts make use of complex incident field data within the inverse strategy, returning successful qualitative imaging results, then the inverse source solutions detailed in Chapter 3 have been included within the inverse scattering method.

The inversion strategy has been then specifically tested in the case of biomedical imaging applications, with a focus on the breast imaging scenario. System design specifications and validation of the phaseless imaging method on 3D in-silico models and on 2D realistic breast cases have been discussed and shown in Chapter 5.

Despite the strong restrictions imposed by the proposed solution, i.e. neglecting the phase information content of the sampled data, remarkable reconstruction results have been obtained, both in the case of homogeneous targets and in the case of strong inhomogeneous targets such as the breast case. However, those restrictions prove to have a significant impact on the quantitative accuracy of the reconstruction methods, whereas the result remains still valuable from a qualitative point of view. The imaging results show a good correlation with the corresponding ground truth, whereas the accuracy of the quantitative reconstruction of the EM properties is limited by the phaseless approach, especially in the case of highly heterogeneous structures. Indeed, those kinds of solutions may find repeatability and validation in applications with limited sensitivity and specificity requirements, so that qualitative reconstruction can be acceptable, in exchange for desirable reduced hardware requirements.

Appendices

Tissue Phantoms

As a parallel activity to the development of the phaseless microwave imaging inversion method described in Chapter 4, the realization of tissue phantoms mimicking the electromagnetic properties of human tissue has been investigated. The principal goal of this task was to provide a repeatable making process, according to easy-follow guidelines, in order to obtain semi-solid phantoms, with a certain stability over time. Secondly, some guidelines are put in evidence for the control of the dielectric behavior of such mixtures, by changing the percentage of the involved ingredients. Those tissue phantoms have been fabricated and secondly validated to assess the sensing performance of electromagnetic wearable devices [125], [126], with the aim to extend their usage and feasibility for the microwave imaging community too. Indeed, such phantoms can allow the assessment of the imaging system performance or the validation of image reconstruction algorithms, under the assumptions of a well-controlled dielectric trend over frequency and high repeatability of the mixtures.

Tissue-mimicking Phantoms Realization and Characterization

The fabricated tissue-mimicking phantoms are in the form of gelatin-based mixtures, since they result more feasible for the realization of multi-layer structures. The ingredients concentrations are summarized in Table A.1, for the different internal breast tissues, where easily-available ingredients from groceries have been used.

Table A.1: Ingredients concentration for the different tissue-mimicking phantoms.

Tissue	Water [%]	Gelatine [%]	Oil [%]	Soap [%]	Salt [%]
Fat	14	3.6	80	2.4	-
Gland	60.9	10.8	21.4	6.2	0.7
Blood	70	10.5	6.8	12.3	0.4

As a general guideline, the water/oil ratio is selected to cope with the lower (higher) dielectric permittivity values associated to tissues with low (high) water content. A food gelatin is used as solidifying agent, whereas soap and salt are used to keep the mixture uniform and to control the conductivity trend, respectively.

The EM properties have been measured by means of an open-ended coaxial probe technique; a DAK-3.5 coaxial probe, provided by SPEAG® has been used, whereas the mixtures have been characterized up to 5 GHz.

The retrieved EM properties of the fabricated phantoms are shown in Fig. A.1. Furthermore, the upper and lower quartiles (25^{th} and 75^{th} percentiles) for two of the breast groups described in Chapter 5, namely Group 1 - here referred to as Gland - corresponding to breast tissue samples with a 0-30 % adipose tissue and Group 3 - here referred as Fat - containing all samples with an 85-100 % adipose tissue are reported. For both groups, the median dielectric constant and conductivity profiles are considered as references. The permittivity of those materials has been included in the breast models analyzed in this thesis and the imaging task is then performed. As for the blood tissue, whose EM properties are assumed to be equivalent to the ones of a tumor inclusion within the breast, the corresponding model provided by Gabriel et al. in [127], [128] has been considered as reference.

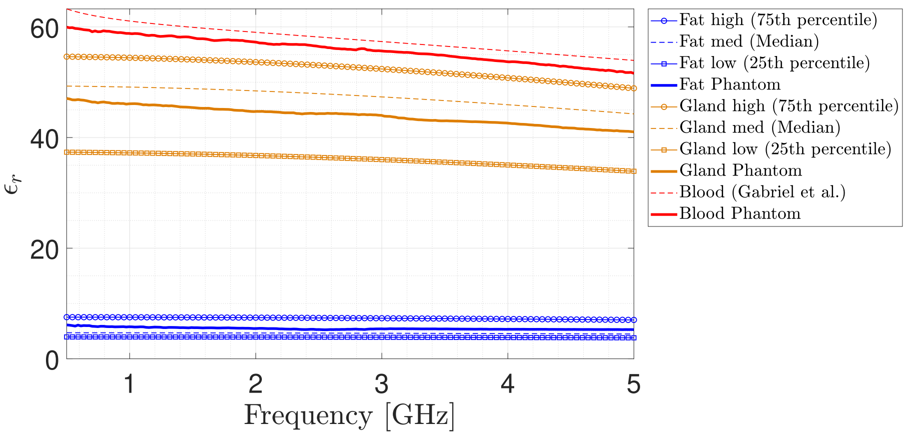

(a)

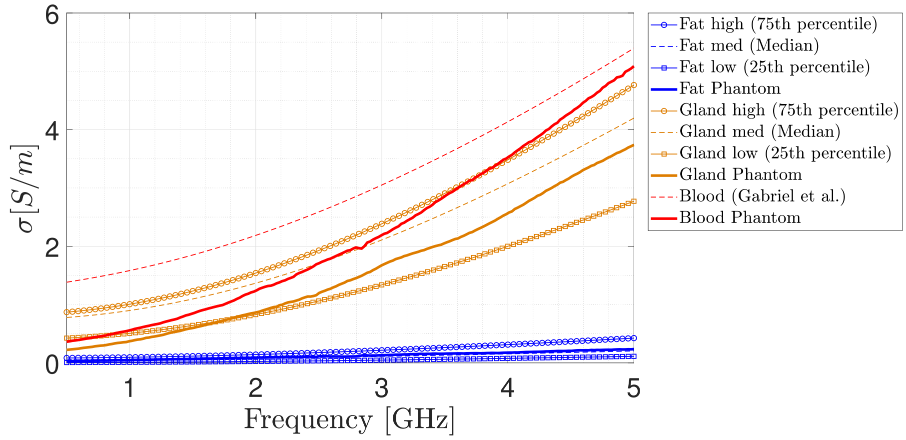

(b)

Figure A.1: Electromagnetic properties of the fabricated phantoms (bold curves) compared to the models provided in [104] (breast tissues), and [127], [128] (blood).

Discrete Forward Solver Implementation

In the case of a 2D scattering problem, the scattering object is assumed to be infinitely long along its longitudinal direction; under this assumption, the generic position vector is limited within the transverse plane. Before considering the two-dimensional case, the expression of the scattering field in a 1D case can be defined as the discrete convolution between the kernel function G and the current source, here indicated as W:

$$E_m = \sum_{n=1}^{N} G_{mn} W_n, \qquad m = 1, 2, \ldots, N \tag{4}$$

where G_{mn} indicates the interaction matrix between the m^{th} and the n^{th} cell. Re-writing Eq. (4) in a matrix form, results in:

$$\bar{E} \ = \bar{\bar{G}}\bar{W} \tag{5}$$

The discrete form of the convolution can be implemented according to an FFT-based method, but this can be done only if the convolution is converted to a circular discrete convolution[1]. Consequently, the G matrix would exhibit the property that its rows are circular right shifts of the elements composing the previous row, i.e., the G matrix needs to be of a circular type. Since the convolution as it is, does not represent a circular convolution, the sequence of G elements needs to be extended, by repeating the elements with a period of $2N-1$. The contrast source vector W needs to be zero-padded with $N-1$ zeros, in order to eliminate the contribution coming from the added $N-1$ elements in the extended G matrix.

[1]The analytical details are taken from: X. Chen, "Computational methods for electromagnetic inverse scattering," John Wiley & Sons, pp. 299–301, 2018.

Therefore, the two-dimensional discrete convolution can be expressed as:

$$E_{ij} = \sum_{m=1}^{M}\sum_{n=1}^{N} G_{i-m,j-n} W_{mn} \qquad i = 1, 2, \dots,\ M, \quad j = 1, 2, \dots, N \tag{6}$$

The circular discrete convolution is then composed by considering the contrast source extended for both directions, with size $(2M-1) \times (2N-1)$, in the form:

$$\bar{\bar{W}}^{e}(p,q) = \begin{cases} W(p,q), & \text{if } 1 \leq p \leq M \text{ and } 1 \leq q \leq N \\ 0, & \text{if } M \leq p \leq 2M \text{ and } N \leq q \leq 2N-1 \end{cases} \tag{7}$$

The extended version of the Green's operator, with size $(2M-1)\times(2N-1)$, is expressed as:

$$\bar{\bar{G}}^{e}(p,q) = G_{p',q'} \tag{8}$$

where the subscripts are defined as:

$$\begin{aligned} p' &= \begin{cases} p-1, & \text{if } 1 \leq p < M \\ p-2M, & \text{if } M \leq p \leq 2M-1 \end{cases} \\ q' &= \begin{cases} q-1, & \text{if } 1 \leq q < N \\ q-2N, & \text{if } N \leq q \leq 2N-1 \end{cases} \end{aligned} \tag{9}$$

The extended matrix including the scattered field, namely $\bar{\bar{E}}^{e}$ and with size $(2M-1) \times (2N-1)$, can be calculated by the use of the 2D-FFT:

$$\bar{\bar{E}}^{e} = FFT_2^{-1}\left\{FFT_2\left\{\bar{\bar{G}}^{e}\right\} .* FFT_2\left\{\bar{\bar{W}}^{e}\right\}\right\} \tag{10}$$

From the extended scattered field $\bar{\bar{E}}^{e}$, the actual scattered field is extracted as the submatrix of size $M \times N$. This closes the part relative to the discretized operators involved in the forward solver implementation, on which the canonical iterative CG-FFT method is based.

References

[1] D. Colton and R. Kress, "Ill-posed problems," in *Applied Mathematical Sciences (Switzerland)*, vol. 93, Springer, 2019, pp. 111–136.

[2] D. Colton and L. Päivärinta, "The uniqueness of a solution to an inverse scattering problem for electromagnetic waves," *Archive for Rational Mechanics and Analysis*, vol. 119, pp. 59–70, 1992.

[3] N. K. Nikolova, "Microwave imaging for breast cancer," *IEEE Microwave Magazine*, vol. 12, no. 7, pp. 78–94, Dec. 2011.

[4] B. M. Moloney, D. O'Loughlin, S. Abd Elwahab, and M. J. Kerin, "Breast cancer detection-a synopsis of conventional modalities and the potential role of microwave imaging," *Diagnostics (Basel, Switzerland)*, vol. 10, no. 2, E103, Feb. 14, 2020.

[5] J. Richmond, "Scattering by a dielectric cylinder of arbitrary cross section shape," *IEEE Transactions on Antennas and Propagation*, vol. 13, no. 3, pp. 334–341, May 1965.

[6] D. Tajik, F. Foroutan, D. S. Shumakov, A. D. Pitcher, and N. K. Nikolova, "Real-time microwave imaging of a compressed breast phantom with planar scanning," *IEEE Journal of Electromagnetics, RF and Microwaves in Medicine and Biology*, vol. 2, no. 3, pp. 154–162, Sep. 2018.

[7] R. Kazemivala, D. Tajik, and N. K. Nikolova, "Simultaneous use of the born and rytov approximations in real-time imaging with fourier-space scattered power mapping," *IEEE Transactions on Microwave Theory and Techniques*, vol. 70, no. 5, pp. 2904–2920, May 2022.

[8] D. Tajik, R. Kazemivala, and N. K. Nikolova, "Real-time imaging with simultaneous use of born and rytov approximations in quantitative microwave holography," *IEEE Transactions on Microwave Theory and Techniques*, vol. 70, no. 3, pp. 1896–1909, 2021.

[9] M. Wang, R. Scapaticci, M. Cavagnaro, and L. Crocco, "Towards a microwave imaging system for continuous monitoring of liver tumor ablation: Design and in silico validation of an experimental setup," *Diagnostics*, vol. 11, no. 5, p. 866, May 2021.

[10] S. Doğu, M. N. Akıncı, M. Çayören, and İ. Akduman, “Truncated singular value decomposition for through-the-wall microwave imaging application,” *IET Microwaves, Antennas & Propagation*, vol. 14, no. 4, pp. 260–267, Mar. 2020.

[11] F. Soldovieri and R. Solimene, “Through-wall imaging via a linear inverse scattering algorithm,” *IEEE Geoscience and Remote Sensing Letters*, vol. 4, no. 4, pp. 513–517, Oct. 2007.

[12] M. Donelli, G. Franceschini, A. Martini, and A. Massa, “An integrated multiscaling strategy based on a particle swarm algorithm for inverse scattering problems,” *IEEE Transactions on Geoscience and Remote Sensing*, vol. 44, no. 2, pp. 298–312, Feb. 2006.

[13] M. Donelli and A. Massa, “Computational approach based on a particle swarm optimizer for microwave imaging of two-dimensional dielectric scatterers,” *IEEE Transactions on Microwave Theory and Techniques*, vol. 53, no. 5, pp. 1761–1776, May 2005.

[14] M. Ostadrahimi, P. Mojabi, A. Zakaria, J. LoVetri, and L. Shafai, “Enhancement of gauss–newton inversion method for biological tissue imaging,” *IEEE Transactions on Microwave Theory and Techniques*, vol. 61, no. 9, pp. 3424–3434, Sep. 2013.

[15] G. Teschke and C. Borries, “Accelerated projected steepest descent method for nonlinear inverse problems with sparsity constraints,” *Inverse Problems*, vol. 26, no. 2, p. 025 007, Jan. 2010.

[16] H. Harada, D. Wall, T. Takenaka, and M. Tanaka, “Conjugate gradient method applied to inverse scattering problem,” *IEEE Transactions on Antennas and Propagation*, vol. 43, no. 8, pp. 784–792, Aug. 1995.

[17] C. Estatico, A. Fedeli, M. Pastorino, A. Randazzo, and E. Tavanti, “A phaseless microwave imaging approach based on a lebesgue-space inversion algorithm,” *IEEE Transactions on Antennas and Propagation*, vol. 68, no. 12, pp. 8091–8103, Dec. 1, 2020.

[18] C. Estatico, A. Fedeli, M. Pastorino, A. Randazzo, and E. Tavanti, “Phaseless tomographic inverse scattering in banach spaces,” *Journal of Physics: Conference Series*, vol. 756, no. 1, p. 012 010, Oct. 2016.

[19] L. Li, H. Zheng, and F. Li, “Two-dimensional contrast source inversion method with phaseless data: TM case,” in *IEEE Transactions on Geoscience and Remote Sensing*, vol. 47, Jun. 2009, pp. 1719–1736.

[20] L. Pan, Y. Zhong, X. Chen, and S. P. Yeo, “Subspace-based optimization method for inverse scattering problems utilizing phaseless data,” *IEEE Transactions on Geoscience and Remote Sensing*, vol. 49, no. 3, pp. 981–987, Mar. 2011.

[21] C. Narendra and P. Mojabi, “Phaseless gauss-newton inversion for microwave imaging,” *IEEE Transactions on Antennas and Propagation*, vol. 69, no. 1, pp. 443–456, Jan. 1, 2021.

[22] L. Zhang, K. Xu, Y. Zhong, and K. Agarwal, "Solving phaseless highly nonlinear inverse scattering problems with contraction integral equation for inversion," *IEEE Transactions on Computational Imaging*, vol. 6, pp. 1106–1116, 2020.

[23] A. Dubey and R. Murch, *Distorted wave extended phaseless rytov iterative method for inverse scattering problems*, May 25, 2022. arXiv: `2205.12578[physics]`.

[24] A. Dubey, S. Deshmukh, L. Pan, X. Chen, and R. Murch, "A phaseless extended rytov approximation for strongly scattering low-loss media and its application to indoor imaging," *IEEE Transactions on Geoscience and Remote Sensing*, vol. 60, pp. 1–17, 2022.

[25] J. E. Fajardo, J. Galván, F. Vericat, C. M. Carlevaro, and bibinitperiod R. M. Irastorza, "Phaseless microwave imaging of dielectric cylinders: An artificial neural networks-based approach," *Progress In Electromagnetics Research*, vol. 166, pp. 95–105, 2019.

[26] K. Xu, L. Wu, X. Ye, and X. Chen, "Deep learning-based inversion methods for solving inverse scattering problems with phaseless data," *IEEE Transactions on Antennas and Propagation*, vol. 68, no. 11, pp. 7457–7470, Nov. 2020.

[27] S. F. Razavi and Y. Rahmat-Samii, "Resilience to probe-positioning errors in planar phaseless near-field measurements," *IEEE Transactions on Antennas and Propagation*, vol. 58, no. 8, pp. 2632–2640, Aug. 2010.

[28] L. Crocco, M. D'Urso, and T. Isernia, "Inverse scattering from phaseless measurements of the total field on a closed curve," *Journal of the Optical Society of America A*, vol. 21, no. 4, p. 622, Apr. 1, 2004.

[29] M. D'Urso, K. Belkebir, L. Crocco, T. Isernia, and A. Litman, "Phaseless imaging with experimental data: Facts and challenges," *Journal of the Optical Society of America A*, vol. 25, no. 1, p. 271, Jan. 1, 2008.

[30] O. M. Bucci, L. Crocco, M. D'Urso, and T. Isernia, "Inverse scattering from phaseless measurements of the total field on open lines.," *Journal of the Optical Society of America. A, Optics, image science, and vision*, vol. 23, no. 10, pp. 2566–77, Oct. 2006.

[31] J. R. Fienup, "Reconstruction of an object from the modulus of its fourier transform," *Optics Letters*, vol. 3, no. 1, p. 27, Jul. 1, 1978.

[32] J. R. Fienup, "Phase retrieval algorithms: A comparison," *Applied Optics*, vol. 21, no. 15, p. 2758, Aug. 1, 1982.

[33] J. R. Fienup, "Phase-retrieval algorithms for a complicated optical system," *Applied Optics*, vol. 32, no. 10, pp. 1737–1746, 1993.

[34] G. Hislop, G. C. James, and A. Hellicar, "Phase retrieval of scattered fields," *IEEE Transactions on Antennas and Propagation*, vol. 55, no. 8, pp. 2332–2341, Aug. 2007.

[35] T. Isernia, G. Leone, and R. Pierri, “Radiation pattern evaluation from near-field intensities on planes,” *IEEE Transactions on Antennas and Propagation*, vol. 44, no. 5, pp. 701–710, 1996.

[36] A. P. Anderson and S. Sali, “New possibilities for phaseless microwave diagnostics. part 1: Error reduction techniques,” *IEE Proceedings H: Microwaves Optics and Antennas*, vol. 132, no. 5, pp. 291–298, 1985.

[37] S. Costanzo and G. Di Massa, “An integrated probe for phaseless near-field measurements,” *Measurement: Journal of the International Measurement Confederation*, vol. 31, no. 2, pp. 123–129, 2002.

[38] L. Crocco, M. D'Urso, and T. Isernia, “Faithful non-linear imaging from only-amplitude measurements of incident and total fields.,” *Optics express*, vol. 15, no. 7, pp. 3804–15, Apr. 2, 2007.

[39] N. K. Nikolova, *Introduction to microwave imaging*. Cambridge: Cambridge University Press, 2017, 1-362.

[40] D. Tajik, A. D. Pitcher, and N. K. Nikolova, “Comparative study of the rytov and born approximations in quantitative microwave holography,” *Progress In Electromagnetics Research B*, vol. 79, pp. 1–19, 2017.

[41] T. Brown, I. Jeffrey, and P. Mojabi, “Multiplicatively regularized source reconstruction method for phaseless planar near-field antenna measurements,” *IEEE Transactions on Antennas and Propagation*, vol. 65, no. 4, pp. 2020–2031, Apr. 1, 2017.

[42] D. Colton and R. Kress, “Inverse acoustic and electromagnetic scattering theory,” vol. 93, 1998.

[43] T. Tsuburaya, Z. Meng, and T. Takenaka, “Inverse scattering analysis from measurement data of total electric and magnetic fields by means of cylindrical-wave expansion,” *Electronics*, vol. 8, no. 4, p. 417, Apr. 10, 2019.

[44] F. Bürgel, K. S. Kazimierski, and A. Lechleiter, “A sparsity regularization and total variation based computational framework for the inverse medium problem in scattering,” *Journal of Computational Physics*, 2017.

[45] F. Bürgel, K. S. Kazimierski, and A. Lechleiter, *IPscatt — a MATLAB toolbox for the inverse medium problem in scattering*, 2017.

[46] M. Gehre, “Rapid uncertainty quantification for nonlinear inverse problems,” Ph.D. dissertation, Dec. 17, 2013.

[47] Y. Álvarez, F. Las-Heras, and C. García, *The Sources Reconstruction Method for Antenna Diagnostics and Imaging Applications*. IntechOpen, Nov. 14, 2012.

[48] F. Las-Heras and T. K. Sarkar, “A direct optimization approach for source reconstruction and NF-FF transformation using amplitude-only data,” *IEEE Transactions on Antennas and Propagation*, vol. 50, no. 4, pp. 500–510, Apr. 2002.

[49] D. Smith, M. Leach, M. Elsdon, and S. J. Foti, "Indirect holographic techniques for determining antenna radiation characteristics and imaging aperture fields," *IEEE Antennas and Propagation Magazine*, vol. 49, no. 1, pp. 54–67, Feb. 2007.

[50] S. Costanzo and G. Di Massa, "Spatial domain indirect holographic technique for antenna near-field phaseless measurements," *Radio Science*, vol. 52, no. 4, pp. 432–438, Apr. 1, 2017.

[51] D. Smith, O. Yurduseven, B. Livingstone, and V. Schejbal, "Microwave imaging using indirect holographic techniques," *IEEE Antennas and Propagation Magazine*, vol. 56, no. 1, pp. 104–117, Feb. 2014.

[52] S. Costanzo and G. Di Massa, "Microwave imaging with spatial-domain indirect holography," *Proceedings of the 2017 19th International Conference on Electromagnetics in Advanced Applications, ICEAA 2017*, pp. 1412–1414, Oct. 11, 2017.

[53] S. Costanzo and G. Lopez, "Phaseless approach to microwave biomedical imaging: System requirements towards clinical applications," in *14th European Conference on Antennas and Propagation, EuCAP 2020*, Mar. 1, 2020.

[54] A. Abubakar, P. M. Van den Berg, and S. Y. Semenov, "A robust iterative method for born inversion," *IEEE Transactions on Geoscience and Remote Sensing*, vol. 42, no. 2, pp. 342–354, Feb. 2004.

[55] Y. Alvarez Lopez, F. Las-Heras Andres, M. R. Pino, and T. K. Sarkar, "An improved super-resolution source reconstruction method," *IEEE Transactions on Instrumentation and Measurement*, vol. 58, no. 11, pp. 3855–3866, Nov. 2009.

[56] Y. Alvarez, F. Las-Heras, and M. R. Pino, "Reconstruction of equivalent currents distribution over arbitrary three-dimensional surfaces based on integral equation algorithms," *IEEE Transactions on Antennas and Propagation*, vol. 55, no. 12, pp. 3460–3468, Dec. 2007.

[57] C. Narendra, I. Jeffrey, and P. Mojabi, "Using the source reconstruction method to model incident fields in microwave tomography," *IEEE Antennas and Wireless Propagation Letters*, vol. 16, pp. 46–49, 2017.

[58] P. C. Hansen, "REGULARIZATION TOOLS: A matlab package for analysis and solution of discrete ill-posed problems," *Numerical Algorithms*, vol. 6, no. 1, pp. 1–35, Mar. 1, 1994.

[59] P. C. Hansen, *Rank-Deficient and Discrete Ill-Posed Problems*, ser. Mathematical Modeling and Computation. Society for Industrial and Applied Mathematics, Jan. 1, 1998, 263 pp.

[60] N. Bayat and P. Mojabi, "The effect of antenna incident field distribution on microwave tomography reconstruction," *Progress In Electromagnetics Research*, vol. 145, pp. 153–161, 2014.

[61] N. Bayat and P. Mojabi, “On the use of focused incident near-field beams in microwave imaging,” *Sensors*, vol. 18, no. 9, p. 3127, Sep. 2018.

[62] P. M. Van Den Berg and R. E. Kleinman, “A contrast source inversion method,” *Inverse Problems*, vol. 13, no. 6, pp. 1607–1620, Dec. 1, 1997.

[63] P. M. Van Den Berg and A. Abubakar, “Contrast source inversion method: State of art,” *Journal of Electromagnetic Waves and Applications*, vol. 15, no. 11, pp. 1503–1505, 2001.

[64] D. M. Dunlavy, T. G. Kolda, and E. Acar, “Sandria report poblano v1.0: A matlab toolbox for gradient-based optimization.”

[65] P. M. van den Berg, *Forward and Inverse Scattering Algorithms based on Contrast Source Integral Equations*. 2021.

[66] M. J. Burfeindt, T. J. Colgan, R. O. Mays, *et al.*, “MRI-derived 3-d-printed breast phantom for microwave breast imaging validation,” *IEEE Antennas and Wireless Propagation Letters*, vol. 11, pp. 1610–1613, 2012.

[67] D. Kurrant and E. Fear, “Regional estimation of the dielectric properties of inhomogeneous objects using near-field reflection data,” *Inverse Problems*, vol. 28, no. 7, p. 075 001, Jun. 14, 2012.

[68] Y. Qin, T. Rodet, M. Lambert, and D. Lesselier, “Microwave breast imaging with prior ultrasound information,” *IEEE Open Journal of Antennas and Propagation*, vol. 1, pp. 472–482, Aug. 27, 2020.

[69] N. Bayat and P. Mojabi, “Incorporating spatial priors in microwave imaging via multiplicative regularization,” *IEEE Transactions on Antennas and Propagation*, vol. 68, no. 2, pp. 1107–1118, Feb. 1, 2020.

[70] N. Abdollahi, D. Kurrant, P. Mojabi, M. Omer, E. Fear, and J. LoVetri, “Incorporation of ultrasonic prior information for improving quantitative microwave imaging of breast,” *IEEE Journal on Multiscale and Multiphysics Computational Techniques*, vol. 4, pp. 98–110, 2019.

[71] D. Kurrant, A. Baran, J. LoVetri, and E. Fear, “Integrating prior information into microwave tomography part 1: Impact of detail on image quality,” *Medical Physics*, vol. 44, no. 12, pp. 6461–6481, Dec. 1, 2017.

[72] D. Kurrant, E. Fear, A. Baran, and J. LoVetri, “Integrating prior information into microwave tomography part 2: Impact of errors in prior information on microwave tomography image quality,” *Medical Physics*, vol. 44, no. 12, pp. 6482–6503, Dec. 2017.

[73] R. Potthast, “A study on orthogonality sampling,” *Inverse Problems*, vol. 26, no. 7, p. 074 015, Jul. 1, 2010.

[74] M. T. Bevacqua, R. Palmeri, T. Isernia, and L. Crocco, “Physical interpretation of the orthogonality sampling method,” in *2018 2nd URSI Atlantic Radio Science Meeting (AT-RASC)*, May 2018, pp. 1–3.

[75] M. T. Bevacqua, N. Abdollahi, I. Jeffrey, T. Isernia, and J. LoVetri, "Qualitative techniques for generating spatial prior information for biomedical microwave imaging," in *2020 14th European Conference on Antennas and Propagation (EuCAP)*, Mar. 2020, pp. 1–4.

[76] R. Griesmaier, "Multi-frequency orthogonality sampling for inverse obstacle scattering problems," *Inverse Problems*, vol. 27, no. 8, p. 085 005, Jul. 2011.

[77] D. Colton, H. Haddar, and M. Piana, "The linear sampling method in inverse electromagnetic scattering theory," *Inverse Problems*, vol. 19, no. 6, S105, Nov. 12, 2003.

[78] M. N. Akıncı, M. Çayören, and İ. Akduman, "Near-field orthogonality sampling method for microwave imaging: Theory and experimental verification," *IEEE Transactions on Microwave Theory and Techniques*, vol. 64, no. 8, pp. 2489–2501, Aug. 2016.

[79] A. Zakaria, C. Gilmore, and J. LoVetri, "Finite-element contrast source inversion method for microwave imaging," *Inverse Problems*, vol. 26, no. 11, p. 115 010, Nov. 1, 2010.

[80] A. Arduino, O. Bottauscio, M. Chiampi, and L. Zilberti, "Magnetic resonance-based imaging of human electric properties with phaseless contrast source inversion," *Inverse Problems*, vol. 34, no. 8, p. 084 002, Aug. 1, 2018.

[81] F. Gao, B. D. Van Veen, and S. C. Hagness, "Sensitivity of the distorted born iterative method to the initial guess in microwave breast imaging," *IEEE Transactions on Antennas and Propagation*, vol. 63, no. 8, pp. 3540–3547, Aug. 2015.

[82] K. Belkebir and M. Saillard, "Special section: Testing inversion algorithms against experimental data," *Inverse Problems*, vol. 17, no. 6, p. 1565, Dec. 1, 2001.

[83] J. M. Geffrin, P. Sabouroux, and C. Eyraud, "Free space experimental scattering database continuation: Experimental set-up and measurement precision," *Inverse Problems*, vol. 21, no. 6, S117–S130, Dec. 1, 2005.

[84] A. Abubakar, P. M. Van Den Berg, and T. M. Habashy, "Application of the multiplicative regularized contrast source inversion method on TM- and TE-polarized experimental fresnel data," *Inverse Problems*, vol. 21, no. 6, Dec. 1, 2005.

[85] S. Sun, B. J. Kooij, T. Jin, and A. G. Yarovoy, "Cross-correlated contrast source inversion," *IEEE Transactions on Antennas and Propagation*, vol. 65, no. 5, pp. 2592–2603, May 2017. arXiv: `1906.10864`.

[86] D. O. Rodriguez-Duarte, J. A. T. Vasquez, R. Scapaticci, L. Crocco, and F. Vipiana, "Assessing a microwave imaging system for brain stroke monitoring via high fidelity numerical modelling," *IEEE Journal of Electromagnetics, RF and Microwaves in Medicine and Biology*, vol. 5, no. 3, pp. 238–245, Sep. 2021.

[87] J. A. Tobon Vasquez, R. Scapaticci, G. Turvani, *et al.*, "A prototype microwave system for 3d brain stroke imaging," *Sensors*, vol. 20, no. 9, p. 2607, Jan. 2020.

[88] J. A. Tobon Vasquez, R. Scapaticci, G. Turvani, *et al.*, "Design and experimental assessment of a 2d microwave imaging system for brain stroke monitoring," *International Journal of Antennas and Propagation*, vol. 2019, pp. 1–12, May 5, 2019.

[89] M. Haynes, J. Stang, and M. Moghaddam, "Real-time microwave imaging of differential temperature for thermal therapy monitoring," *IEEE Transactions on Biomedical Engineering*, vol. 61, no. 6, pp. 1787–1797, Jun. 2014.

[90] A. Mirbeik and N. Tavassolian, "Ultra-high resolution millimeter-wave imaging for biomedical applications: Feasibility study," in *2015 IEEE Biomedical Circuits and Systems Conference (BioCAS)*, IEEE, Oct. 2015, pp. 1–4.

[91] C. Dachena, A. Fedeli, A. Fanti, M. B. Lodi, M. Pastorino, and A. Randazzo, "Microwave imaging for the diagnosis of cervical diseases: A feasibility analysis," *IEEE Journal of Electromagnetics, RF and Microwaves in Medicine and Biology*, vol. 5, no. 3, pp. 277–285, Sep. 2021.

[92] B. M. Moloney, P. F. McAnena, S. M. Abd Elwahab, *et al.*, "Microwave imaging in breast cancer - results from the first-in-human clinical investigation of the wavelia system," *Academic Radiology*, vol. 29 Suppl 1, S211–S222, Jan. 2022.

[93] L. Sani, A. Vispa, R. Loretoni, *et al.*, "Breast lesion detection through MammoWave device: Empirical detection capability assessment of microwave images' parameters," *PloS One*, vol. 16, no. 4, e0250005, 2021.

[94] A. Fasoula, L. Duchesne, J. D. Gil Cano, P. Lawrence, G. Robin, and J.-G. Bernard, "On-site validation of a microwave breast imaging system, before first patient study," *Diagnostics*, vol. 8, no. 3, p. 53, Sep. 2018.

[95] Z. Miao, P. Kosmas, and S. Ahsan, "Impact of information loss on reconstruction quality in microwave tomography for medical imaging," *Diagnostics*, vol. 8, no. 3, p. 52, Aug. 14, 2018.

[96] P. M. Meaney, S. A. Pendergrass, M. W. Fanning, D. Li, and K. D. Paulsen, "Importance of using a reduced contrast coupling medium in 2d microwave breast imaging," *Journal of Electromagnetic Waves and Applications*, vol. 17, no. 2, pp. 333–355, 2003.

[97] P. M. Meaney, F. Shubitidze, M. W. Fanning, M. Kmiec, N. R. Epstein, and K. D. Paulsen, “Surface wave multipath signals in near-field microwave imaging,” *International Journal of Biomedical Imaging*, vol. 2012, pp. 1–11, Apr. 10, 2012.

[98] P. M. Meaney, C. J. Fox, S. D. Geimer, and K. D. Paulsen, “Electrical characterization of glycerin: Water mixtures: Implications for use as a coupling medium in microwave tomography,” *IEEE Transactions on Microwave Theory and Techniques*, vol. 65, no. 5, pp. 1471–1478, May 2017.

[99] G. N. Bindu, A. Lonappan, V. Thomas, C. Aanandan, and bibinitperiod K. Mathew, “Dielectric studies of corn syrup for applications in microwave breast imaging,” *Progress In Electromagnetics Research*, vol. 59, pp. 175–186, 2006.

[100] D. O. Rodriguez-Duarte, J. A. T. Vasquez, R. Scapaticci, L. Crocco, and F. Vipiana, “Brick-shaped antenna module for microwave brain imaging systems,” *IEEE Antennas and Wireless Propagation Letters*, vol. 19, no. 12, pp. 2057–2061, Dec. 2020.

[101] Weng Cho Chew, *Waves and Fields in Inhomogenous Media*. Wiley-IEEE Press, 1995, 632 pp.

[102] M. Lazebnik, M. Okoniewski, J. H. Booske, and S. C. Hagness, “Highly accurate debye models for normal and malignant breast tissue dielectric properties at microwave frequencies,” *IEEE Microwave and Wireless Components Letters*, vol. 17, no. 12, pp. 822–824, Dec. 2007.

[103] M. Lazebnik, E. L. Madsen, G. R. Frank, and S. C. Hagness, “Tissue-mimicking phantom materials for narrowband and ultrawideband microwave applications,” *Physics in Medicine and Biology*, vol. 50, no. 18, pp. 4245–4258, Sep. 21, 2005.

[104] M. Lazebnik, D. Popovic, L. McCartney, *et al.*, “A large-scale study of the ultrawideband microwave dielectric properties of normal, benign and malignant breast tissues obtained from cancer surgeries,” *Physics in Medicine and Biology*, vol. 52, no. 20, pp. 6093–6115, Oct. 21, 2007.

[105] S. Ahsan, B. Yeboah-Akowuah, P. Kosmas, H. C. Garcia, G. Palikaras, and E. Kallos, “Balanced antipodal vivaldi antenna for microwave tomography,” in *Proceedings of the 2014 4th International Conference on Wireless Mobile Communication and Healthcare - "Transforming Healthcare Through Innovations in Mobile and Wireless Technologies", MOBIHEALTH 2014*, Institute of Electrical and Electronics Engineers Inc., Jan. 20, 2015, pp. 316–319.

[106] T. A. Milligan, *Modern Antenna Design: Second Edition*. John Wiley and Sons, Jan. 27, 2005, 1-614.

[107] M. Ostadrahimi, S. Noghanian, and L. Shafai, “A modified double layer tapered slot antenna with improved cross polarization,” in *2009 13th International Symposium on Antenna Technology and Applied Electromagnetics and the Canadian Radio Science Meeting*, IEEE, Feb. 2009.

[108] M. Ostadrahimi, S. Noghanian, L. Shafai, A. Zakaria, C. Kaye, and J. LoVetri, “Investigating a double layer vivaldi antenna design for fixed array field measurement,” *International Journal of Ultra Wideband Communications and Systems*, vol. 1, no. 4, 2010.

[109] A. M. Abbosh, H. K. Kan, and M. E. Bialkowski, “Compact ultra-wideband planar tapered slot antenna for use in a microwave imaging system,” *Microwave and Optical Technology Letters*, vol. 48, no. 11, pp. 2212–2216, Nov. 1, 2006.

[110] A. M. Abbosh, H. K. Kan, and M. E. Bialkowski, “Design of compact directive ultra wideband antipodal antenna,” *Microwave and Optical Technology Letters*, vol. 48, no. 12, pp. 2448–2450, Dec. 1, 2006.

[111] M. Wang, L. Crocco, and M. Cavagnaro, “On the design of a microwave imaging system to monitor thermal ablation of liver tumors,” *IEEE Journal of Electromagnetics, RF and Microwaves in Medicine and Biology*, 2021.

[112] M. Wang, L. Crocco, S. Costanzo, R. Scapaticci, and M. Cavagnaro, “A compact slot-loaded antipodal vivaldi antenna for a microwave imaging system to monitor liver microwave thermal ablation,” *IEEE Open Journal of Antennas and Propagation*, pp. 1–1, 2022.

[113] M. J. Burfeindt, N. Behdad, B. D. Van Veen, and S. C. Hagness, “Quantitative microwave imaging of realistic numerical breast phantoms using an enclosed array of multiband, miniaturized patch antennas,” *IEEE Antennas and Wireless Propagation Letters*, vol. 11, pp. 1626–1629, 2012.

[114] “Breast lesion detection through MammoWave device: Empirical detection capability assessment of microwave images’ parameters | PLOS ONE.” (), [Online]. Available: `https://journals.plos.org/plosone/article/authors?id=10.1371/journal.pone.0250005` (visited on 11/04/2022).

[115] “ACR statement on reporting breast density in mammography reports and patient summaries | american college of radiology.” (), [Online]. Available: `https://www.acr.org/Advocacy-and-Economics/ACR-Position-Statements/Reporting-Breast-Density` (visited on 10/01/2021).

[116] N. Joachimowicz, C. Conessa, T. Henriksson, and B. Duchêne, “Breast phantoms for microwave imaging,” *IEEE Antennas and Wireless Propagation Letters*, vol. 13, pp. 1333–1336, 2014.

[117] N. Joachimowicz, B. Duchêne, C. Conessa, and O. Meyer, “Anthropomorphic breast and head phantoms for microwave imaging,” *Diagnostics*, vol. 8, no. 4, p. 85, Dec. 18, 2018.

[118] S. Romeo, L. Di Donato, O. M. Bucci, *et al.*, "Dielectric characterization study of liquid-based materials for mimicking breast tissues," *Microwave and Optical Technology Letters*, vol. 53, no. 6, pp. 1276–1280, Jun. 1, 2011.

[119] S. Di Meo, L. Pasotti, I. Iliopoulos, *et al.*, "Tissue-mimicking materials for breast phantoms up to 50 GHz," *Physics in Medicine and Biology*, vol. 64, no. 5, p. 055 006, Feb. 2019.

[120] T. Yilmaz, R. Foster, and Y. Hao, "Broadband tissue mimicking phantoms and a patch resonator for evaluating noninvasive monitoring of blood glucose levels," *IEEE Transactions on Antennas and Propagation*, vol. 62, no. 6, pp. 3064–3075, Jun. 2014.

[121] E. L. Madsen, M. A. Hobson, H. Shi, T. Varghese, and G. R. Frank, "Stability of heterogeneous elastography phantoms made from oil dispersions in aqueous gels," *Ultrasound in Medicine and Biology*, vol. 32, no. 2, pp. 261–270, Feb. 2006.

[122] E. L. Madsen, M. A. Hobson, H. Shi, T. Varghese, and G. R. Frank, "Tissue-mimicking agar/gelatin materials for use in heterogeneous elastography phantoms," *Physics in Medicine and Biology*, vol. 50, no. 23, pp. 5597–5618, Dec. 7, 2005.

[123] X. Chen, *Computational Methods for Electromagnetic Inverse Scattering.* John Wiley & Sons Singapore Pte. Ltd, May 29, 2018.

[124] A. Costa Batista, L. S. Batista, and R. Adriano, "A quadratic programming approach for microwave imaging," *IEEE Transactions on Antennas and Propagation*, vol. 69, no. 8, pp. 4923–4934, 2021.

[125] S. Costanzo, V. Cioffi, and G. Lopez, "Tissue-mimicking phantoms: Dielectric characterization and design of a multi-layer substrate for microwave blood glucose monitoring," in *Advances in Intelligent Systems and Computing*, vol. 1368 AISC, 2021, pp. 233–239.

[126] S. Costanzo, V. Cioffi, A. M. Qureshi, and A. Borgia, "Gel-like human mimicking phantoms: Realization procedure, dielectric characterization and experimental validations on microwave wearable body sensors," *Biosensors*, vol. 11, no. 4, p. 111, Apr. 2021.

[127] C. Gabriel, "Compilation of the dielectric properties of body tissues at RF and microwave frequencies," 1996.

[128] S. Gabriel, R. W. Lau, and C. Gabriel, "The dielectric properties of biological tissues: III. parametric models for the dielectric spectrum of tissues," *Physics in Medicine and Biology*, vol. 41, no. 11, pp. 2271–2293, Nov. 1996.

Publications

Journals

J1. S. Costanzo, G. Lopez and G. Di Massa, "Spatial Domain Indirect Holography for a Full Phaseless Approach to Biomedical Microwave Imaging," *IEEE Open Journal of Antennas and Propagation*, 2022.

J2. S. Costanzo and G. Lopez, "Phaseless Microwave Tomography Assessment For Breast Imaging: Preliminary Results," *International Journal of Antennas and Propagation - Bioengineering Applications of Electromagnetic Wave Propagation*, 2020.

J3. S. Costanzo and G. Lopez, "Phaseless Single-Step Microwave Imaging Technique for Biomedical Applications," *Radioengineering*, 2019.

Book Chapters

Ch1. S. Costanzo, G. Lopez and G. Di Massa, "Full Phaseless Approach to Inverse Scattering," *In Consorzio Nazionale Interuniversitario per le Telecomunicazioni (CNIT) Technical Report 10* - Chapter 9 (In Press).

Conference Proceedings

C1. S. Costanzo, G. Lopez, N. K. Nikolova and G. Di Massa, "Inverse Source and Scattering Solution with Phaseless Data: Near Field In-Silico Validation," *17th European Conference on Antennas and Propagation (EuCAP)*, 2023 (Accepted).

C2. S. Costanzo, G. Lopez and G. Di Massa, "Incident Field Modeling in the Imaging Domain: a strategy for Amplitude Only Reconstruction Methods," *XXIV Riunione Nazionale di Elettromagnetismo (RiNEm),* 2022.

C3. S. Costanzo, G. Lopez and G. Di Massa, "A Combined Strategy for Incident Field Characterization in Phaseless Microwave Imaging," *VI Convegno Nazionale "Interazione tra Campi Elettromagnetici e Biosistemi (ICEmB),* 2022.

C4. S. Costanzo, G. Lopez and G. Di Massa, "Spatial Domain Indirect Holography for Phaseless Microwave Imaging," *16th European Conference on Antennas and Propagation (EuCAP)*, 2022.

C5. S. Costanzo and G. Lopez, "Dielectric Characterization of Breast Phantoms for Phaseless Microwave Imaging Focused on Tumor Identification," *In World Conference on Information Systems and Technologies (WorldCIST)*, Springer, 2021.

C6. S. Costanzo, V. Cioffi and G. Lopez, "Tissue-Mimicking Phantoms: Dielectric Characterization and Design of a Multi-Layer Substrate for Microwave Blood Glucose Monitoring," *In World Conference on Information Systems and Technologies (WorldCIST)*, Springer, 2021.

C7. S. Costanzo and G. Lopez, "Microwave Breast Imaging: Preliminary Phantoms Realization and Phaseless Reconstructions," *XXXIVth General Assembly and Scientific Symposium of the International Union of Radio Science (URSI GASS)*, 2021.

C8. S. Costanzo and G. Lopez, "Low-Complexity Amplitude-Only Breast Imaging Technique," *15th European Conference on Antennas and Propagation (EuCAP),* 2021.

C9. S. Costanzo and G. Lopez, "2D Amplitude-Only Microwave Tomography Algorithm for Breast-Cancer Detection," *The 14th IEEE International Conference Application of Information and Communication Technologies (AICT),* 2020.

C10. S. Costanzo and G. Lopez, "Phaseless Microwave Breast Imaging: Preliminary Study and Coupling Medium Effects," *IEEE MTT-S International Microwave Biomedical Conference (IMBioC),* 2020.

C11. S. Costanzo and G. Lopez, "Phaseless Approach to Microwave Biomedical Imaging: System Requirements towards Clinical Applications," *14th European Conference on Antennas and Propagation (EuCAP),* 2020.

C12. S. Costanzo and G. Lopez, "Single-Step Approach to Phaseless Contrast-Source Inverse Scattering," *In World Conference on Information Systems and Technologies (WorldCIST),* Springer, 2019.

C13. S. Costanzo and G. Lopez, "Single-Step Phaseless Inverse Scattering Approach," *PhotonIcs and Electromagnetics Research Symposium (PIERS) Proceedings,* 2019.